LOS ALAMOS SCIENTIFIC LABORATORY
of the
University of California

LOS ALAMOS • NEW MEXICO

Status Report of the

LASL Controlled Thermonuclear Research Program

for 12-Month Period Ending October 1970

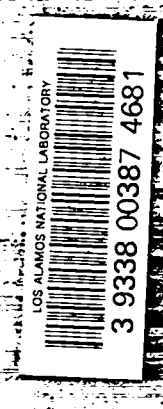

UNITED STATES
ATOMIC ENERGY COMMISSION
CONTRACT W-7405-ENG. 36

This LA-...-MS report presents the status of the LASL Controlled Thermonuclear Research Program. Previous annual status reports in this series, all unclassified, are:

LA-3628-MS
LA-3831-MS
LA-4075-MS
LA-4351-MS

This report, like other special-purpose documents in the LA-...-MS series has not been reviewed or verified for accuracy in the interest of prompt distribution.

Printed in the United States of America. Available from
National Technical Information Service
U. S. Department of Commerce
Springfield, Virginia 22151
Price: Printed Copy $3.00; Microfiche $0.65

Distributed: February 1971

LA-4585-MS
UC-20, CONTROLLED
THERMONUCLEAR PROCESSES
TID-4500

LOS ALAMOS SCIENTIFIC LABORATORY
of the
University of California
LOS ALAMOS • NEW MEXICO

Status Report of the

LASL Controlled Thermonuclear Research Program

for 12-Month Period Ending October 1970

TABLE OF CONTENTS

INTRODUCTION

J. L. Tuck

The prime task of bringing into operation the five-meter curved section of the Scyllac is on schedule and proceeding well (P-15). Already, the on-line computer gap monitoring and data acquisition is proving its worth during the setting-up stage. Operation with plasma is expected in January 1971. The linear Scylla with x2 mirrors is also proceeding: the projected operation date is late 1971.

The shock-heated toroidal z-pinch (P-14) is in advanced construction. This experiment should give a definite answer to the question whether or not fast z-pinches have a future for pulsed fusion power. Experimental observation is estimated for the Spring of 1971.

Although it is peripheral to CTR, the three successful firings of high power plasma guns powered from a complicated two-stage explosive generator and carried by rocket to 210 km altitude, must be acknowledged to be a remarkable physical and engineering tour de force (P-17).

On the mathematical physics side (P-18), the computer simulation of plasma has been carried to new heights of sophistication. It has justified our early confidence and become a major tool of plasma physics. The electron cyclotron drift instability which it revealed is probably the key to understanding anomalous plasma resistivity which is widely observed in machines such as Tokamak.

THETA PINCH

EXPERIMENTS ON SCYLLA IV-3 WITH $\ell = 1$ FIELDS PRODUCED BY HELICAL GROOVES IN THE COMPRESSION COIL (P-15)

(C. F. Hammer, W. E. Quinn, F. L. Ribe
R. E. Siemon, K. S. Thomas)

In the last annual report,[1] the operation of Scylla IV with a 3-meter coil was reported. The effort during this report period has been devoted almost entirely to experimental studies with $\ell = 1$ helical magnetic field configurations superimposed on the 3-*m* theta pinch. The effects of an $\ell = 1$ field are of considerable interest since it has been shown theoretically that such a field configuration can provide an equilibrium for a toroidal high-β plasma. Plasma studies have been made with a 135-cm $\ell = 1$ region in the center of the compression coil as well as with the $\ell = 1$ configuration extending over the full length of the 3-*m* coil. In addition, an axial current I_z has been used.

These experiments with $\ell = 1$ fields were conducted primarily to test the Grad, Weitzner, Freidberg stability theory. The most important fact to emerge is that only the $m = 1$ MHD mode is present. An unexpected observation is the importance of induced net longitudinal current I_z which must now be understood in order to avoid Kruskal modes in Scyllac. Since these $\ell = 1$ fields were generated by helical grooves in the compression coil, their timing (simultaneous)with respect to the main field could not be changed. There is theoretical reason to expect that I_z is sensitive to this timing, and, consequently, we shall do new experiments on Scylla IV-3--and have designed Scyllac--with $\ell = 1$ fields generated by helical coils.

The $m = 1$ growth rate observed is sensitive to initial implosion conditions, as controlled by applying external I_z, which was, however, done for reasons of controlling the $\ell = 1$ induced I_z. We infer that the wide variations of growth rate observed reflect a change of β with changed initial conditions. That inference must be checked on the new experiments. At any rate, we see some quite slow growth rates, easily amenable to feedback stabilization. The question next to be investigated is: with what β's and ion temperatures are they associated?

EXPERIMENTS WITH AN $\ell = 1$ HELICAL FIELD SUPERIMPOSED ON THE CENTRAL 135-cm LENGTH OF A 3-*m* THETA PINCH

Experimental Arrangement. The $\ell = 1$ helical magnetic field is produced by cutting a spiral groove or thread in the inside surface of the compression coil. In the present experiment the coil inner surface is shaped as a flux surface of the $\ell = 1$ helical field by means of rectangular grooves of depth $\Delta = 1.59$ cm and wavelength of 30 cm ($h = 2\pi/30 = 0.209$). These grooves provide an approximation to a sinusoidal amplitude at the coil surface (cf. F. L. Ribe, LA-4098),

$$\delta_1(b) = \frac{\Delta}{2b}\left(1 - \frac{\Delta}{2b}\right) = 0.13, \qquad (1)$$

where b is the inside radius of the coil. For a wall-to-plasma radius ratio $b/a = 6.0/0.63 = 9.5$ and $\beta = 0.5$, the plasma distortion $\delta_1(a) = 1.6$. Here δ_1 is the ratio of the helical excursion to the mean coil or plasma radius.

In the initial experiments, the $\ell = 1$ section occupied a 135-cm length in the central region of the compression coil with uniform field regions of 90 cm and 75 cm on its ends. Most of the experiments with this arrangement were performed with an annular array of trapezoidal Inconel-tube inserts filling the $\ell = 1$ grooves. These were used to provide an initial homogeneous B_z field during the shock implosion phase of the discharge with the generation of the $\ell = 1$ field occurring as the magnetic flux diffuses into the Inconel inserts. The $\ell = 1$ groove with the Inconel inserts in the lower half of the compression coil is shown in Fig. 1. Only one 15-cm section of the smooth-bore portion of the coil is shown at each end of the $\ell = 1$ section. The longer coil tab (Fig. 1) connects to the collector plate current feed.

Streak cameras viewed the plasma column side-on at the coil midplane near the center of the $\ell = 1$ region, at the end of the $\ell = 1$ region 60-cm off the midplane, and at a position 15 cm beyond the other end of the $\ell = 1$ region 90 cm from the coil midplane. Each streak camera viewed the plasma stereoscopically. The holographic interferometer arrangement was used to view the plasma column in the axial direction. Neutron

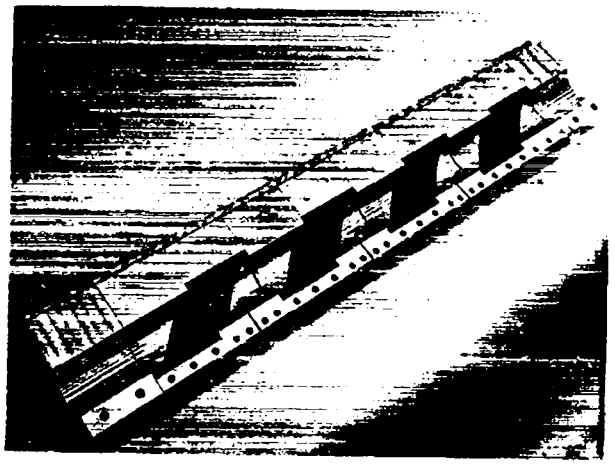

Fig. 1. Portion of Scylla IV-3 compression coil showing $\ell = 1$ helical groove and Inconel inserts.

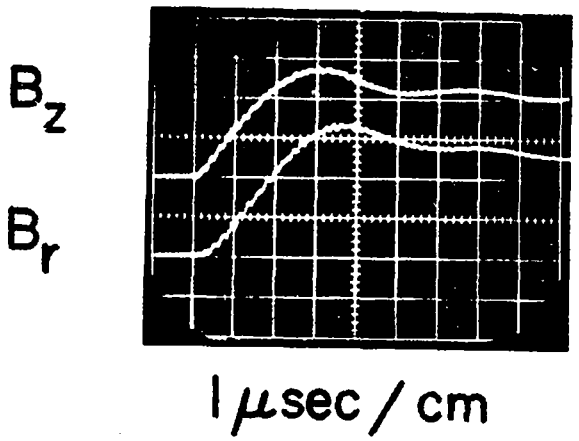

Fig. 2. Oscillograms of Scylla IV-3 compression field (top) and B_r component of $\ell = 1$ field.

emission from the plasma was observed by means of a plastic scintillation counter and by silver activation counters.

Initial Results. Magnetic probe measurements of the B_r component of the $\ell = 1$ helical vacuum field show the delaying effect of the Inconel inserts, as shown in Fig. 2. The upper trace of the oscillogram shows the applied B_z field and the lower trace the B_r component of the $\ell = 1$ field. The $\ell = 1$ helical field lags the B_z field by approximately one-half microsecond. The peak magnitude of the vacuum B_r component is about 8 kG at a radius of 3.2 cm, or approximately 15% of the B_z field.

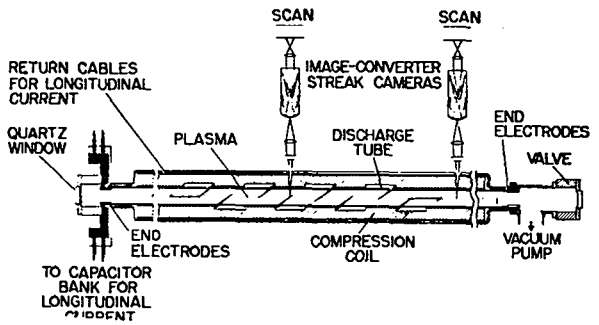

Fig. 3. Scylla IV-3 coil with $\ell = 1$ grooves and end electrodes

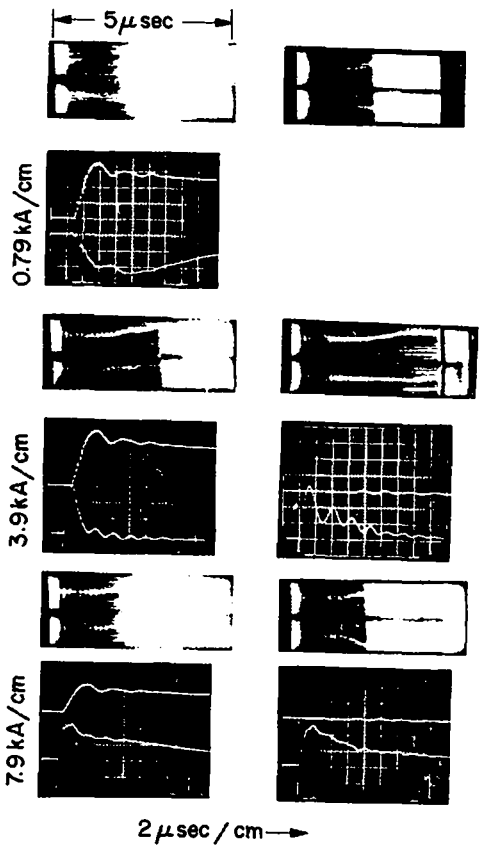

Fig. 4. Streak photographs of $m = 1$ instability in Scylla IV-3 with 135-cm of $\ell = 1$ field. The oscillograms show the compression field (top) and the I_z current.

This corresponds to a plasma distortion at $r = a = 0.63$ cm

$$\delta_1(a) = [(ha)(1 - \beta/2)]^{-1} B_r/B_o = 1.5. \qquad (2)$$

Typical streak photographs, using the arrangement in Fig. 3, of the radial plasma motion taken under the above conditions are shown in the upper streaks of Fig. 4. The streaks on the left were taken at the coil midplane and those on the right at a position 15 cm beyond the end of the $\ell = 1$ region, 90 cm from the coil midplane. The upper streak photograph of each vertical pair shows the plasma motion in the horizontal plane with the coil feedslot at the bottom, while the lower streak of each pair shows the vertical motion of the plasma column in its true orientation. The streak photographs show that the plasma column in the $\ell = 1$ region goes to the discharge tube wall in an $m = 1$ sideways motion. An analysis of several such streak photographs shows the following: (1) The plasma column in the central portion of the $\ell = 1$ region moves toward the wall ahead of the column at the ends of the $\ell = 1$ region; (2) the $m = 1$ sideways motion of the plasma column is predominantly in the horizontal plane away from the coil feedpoint; and (3) the plasma begins to move off axis in 1 to 2 μsec and strikes the discharge tube wall at 2 to 3 μsec, i.e., before or at the time of B_z maximum, as evidenced by the abrupt onset of intense illumination across the entire streak photograph.

I_z Currents Generated by the $\ell = 1$ Fields. The application of the $\ell = 1$ helical field on the B_z field can produce a current along the plasma column, since the helical plasma links B_z flux. With the Inconel insert . the $\ell = 1$ field is effectively applied after the formation of the theta-pinch plasma column. This method avoids interference of the $\ell = 1$ field with the symmetry of the initial shock-heating process.

In order to observe such an I_z current, hollow cylindrical electrodes were installed at each end of the theta-pinch coil about 15 cm beyond the coil ends. These electrodes were connected by an external circuit of 8 insulated wires (Fig. 3). Current measurements with a Rogowski loop showed the presence of an I_z current as shown in the lower trace of the upper oscillogram of Fig. 4. The upper trace shows the applied magnetic field. With the 135-cm length $\ell = 1$ coil section, the I_z bucking current attains a maximum value of approximately 1.9 kA. The variation of the bucking current with time follows that of the applied magnetic field (Fig. 4). The sign of the observed I_z is opposite to that produced by a rotational transform penetrating the plasma column of the same sign as that external to the plasma. The I_z current was very reproducible from discharge to discharge.

Results with an Applied I_z Current. An axial I_z current was applied to embed rotational transform during the plasma formation (Fig. 3). A crowbarred 0.7-μF capacitor charged to 41 kV was discharged between the end electrodes with a variable coaxial shunt in parallel with the plasma column to assist in varying the magnitude of I_z.

Composites of streak photographs and corresponding oscillograms with an I_z applied in opposition to the observed $\ell = 1$ induced current are shown in the lower portions of Figs. 4 and 5. The left streaks were taken stereoscopically at the coil midplane, 15 cm beyond the end of the $\ell = 1$ groove, while the right streaks were taken 90 cm off the midplane. The upper streak shows the plasma motion in the horizontal plane and the lower streak the motion in the vertical plane. The lower traces of the left oscillograms below the streak photographs show the I_z current on the given discharge while the upper trace shows the applied B_z field. The oscillograms on the right of Fig. 4 and at the bottom of Fig. 5 show the I_z current resulting from the timing of the passive crowbar when fired on the afterglow of the preionized plasma, before the discharge on which the streak photographs and other oscillograms were taken.

These streak photographs, taken with an applied I_z (Figs. 4 and 5), are to be compared with those of the upper streaks of Fig. 4, which are typical of the case when there is not an applied I_z. In addition, the cases with applied I_z are compared with each other relative to the type and magnitude of the I_z current pulse and relative to the time of application of the main compression field. The center streaks of Fig. 4 show the effect of applying an 11.7 kA pulse of current which is crowbarred off in such a way as to

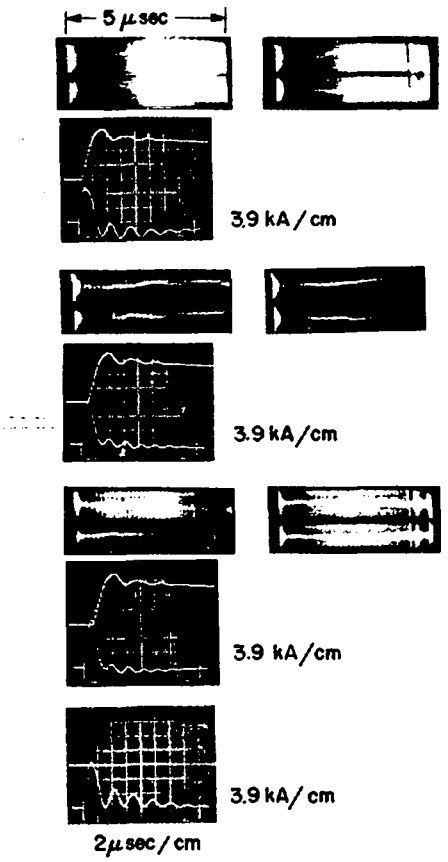

Fig. 5. Streak photographs and oscillograms of Scylla IV-3 as in Fig. 4 with 135-cm of $\ell = 1$ field.

produce a net zero current. The plasma column is almost stable in this case. The lower streaks of Fig. 4 show the effect of applying a 17.4 -kA current pulse sustained with the passive crowbar. In this case, the streaks indicate that, with the increased I_z current, 17.4 kA, a (helical) Kruskal mode has been excited with a quarter-wavelength approximately equal to the distance (90 cm) between the viewing slits. In this case, the plasma column strikes the discharge tube wall.

Figure 5 shows the effect of applying the main B_z field at slightly different times relative to a 12-kA current pulse which is crowbarred to approximately zero current. In the upper streaks, the field was applied before the current pulse attained its peak value. In this case (B_θ outside the plasma column), the plasma column moved to the wall in an $m = 1$ motion in the absence of an applied I_z, much as it did in the upper streaks of Fig. 4. In the center streaks of Fig. 5 the main field was applied at the peak of the I_z current pulse and a grossly stable plasma column resulted. In the lower streaks, the main field was applied after the I_z peak and a grossly stable plasma column was observed with some apparent "shredding."

In general, when the I_z current is applied with a partial or completely sustaining crowbar, the plasma column moves to the discharge tube wall. Also if the I_z current is crowbarred so that a sustaining current results on the second half cycle, i.e., a current in the opposite sense to the initially applied I_z, the plasma column moves to the wall.

Studies were also made with 2 and 5 kA of applied I_z and a sustaining crowbar. There was only a small delay in the onset of the $m = 1$ motion of the plasma column to the discharge tube wall. With a 9-kA current pulse and without a sustaining crowbar, the plasma column was almost stable.

EXPERIMENTS WITH A $\ell = 1$ HELICAL FIELD SUPERIMPOSED ON THE COMPLETE 3-m LENGTH OF THE THETA PINCH

Experimental Arrangement. More recently, experiments have been performed with $\ell = 1$ grooves, starting 15 cm from each end, and extending over the full length of the 3-m compression coil. In these experiments, the Inconel inserts were not used. The same arrangement for the application of an I_z current to the plasma column was used (Fig. 3).

Streak cameras viewed the plasma column at the coil midplane and at 60 cm east and 90 cm west of the midplane. The holographic interferometry arrangement was used to view the plasma column in the axial direction.

Results Without an Applied I_z Current. Streak photographs of the plasma column in the coil with the full-length $\ell = 1$ grooves are shown in Fig. 6A. In the streak photographs in the left vertical columns time elapses from right to left in contrast to the other streaks where time elapses from left to right. These streak photographs show the plasma column moving toward the wall predominantly in

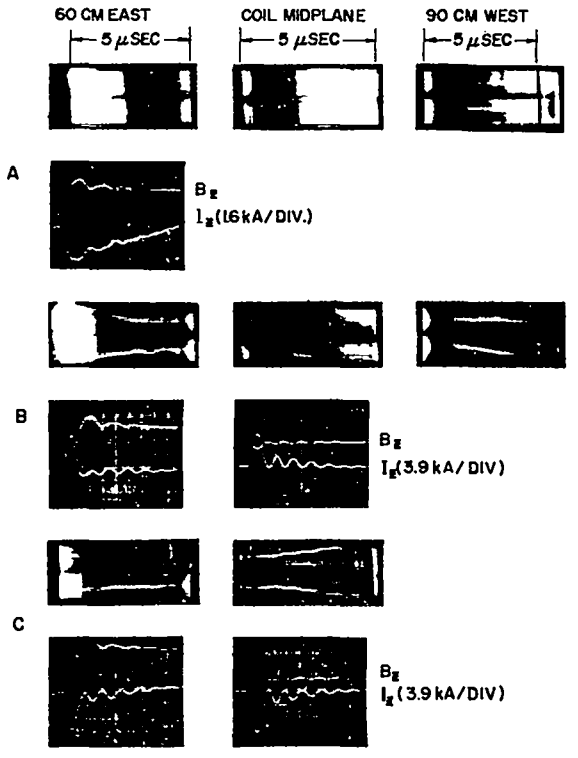

Fig. 6. Streak photographs and oscillograms of Scylla IV-3 with $\ell = 1$ field over the full 3-meter length.

the horizontal plane and opposite the coil feed-point. This behavior is essentially the same as that observed with the 135-cm length $\ell = 1$ region discussed previously. The plasma column begins to move off axis at about 1 to 1.5 μsec after the main bank is applied and strikes the discharge tube wall at approximately 2 to 3 μsec. This phenomenon is quite reproducible from discharge to discharge.

The oscillograms of Fig. 6A show the I_z current induced in the plasma column. The upper traces show the applied magnetic field. The induced I_z current attains a maximum value of approximately 3.9 kA. This is about a factor two greater than the 1.9 kA observed in the 135-cm length, $\ell = 1$ coil region. These two observations indicate that the I_z current scales linearly with the length of the $\ell = 1$ region, which has a length of 270 cm in the present case, compared with the earlier 135-cm length.

Results with an Applied I_z Current. Streak photographs with an I_z current applied in opposition to the $\ell = 1$ induced current are shown in Fig. 6B. Figure 6C shows streak photographs of the plasma column with an I_z current applied in the same direction as the induced current. In the streak photographs in the left vertical column time elapses from right to left in contrast to the other streaks where time elapses from left to right. The oscillograms on the left show the I_z current on the lower traces and the applied magnetic field on the upper traces. The oscillograms on the right show the same applied I_z current on a preionization discharge taken before the main discharge.

With an I_z current pulse of ~18 kA applied in opposition to the $\ell = 1$ induced current, the plasma column is grossly stable but shows some evidence of the shredding phenomenon. When the I_z current pulse is reduced to ~10 kA, as shown in Fig. 6B, the plasma column is almost stable with the column striking the wall at ~ 4 μsec. This is to be compared with the streaks of Fig. 6A taken in the absence of an applied I_z where the plasma column goes to the wall in approximately 2 μsec.

The I_z current was also applied parallel to the current generated by the $\ell = 1$ field. With an I_z current pulse of ~ 18 kA, the plasma column is grossly stable but shows some evidence of the shredding phenomenon. Figure 6C shows typical streak photographs with an I_z current pulse of 11.7 kA. The plasma column is almost stable and goes to the wall in approximately 4 μsec. The experimental conditions for Figs. 6C and 6B were almost identical with the exception that the applied I_z current was in opposition to the $\ell = 1$ induced I_z current in Fig. 6B, whereas it was parallel in Fig. 6C. The gross stability of the plasma column in the two cases is very similar. Several plasma discharges with both current polarities confirm this conclusion. Parallel axial currents of approximately 7 kA were also applied. With the lower parallel I_z current, the plasma moved to the wall with the $m = 1$ sideways motion just as it does without an applied I_z or with an applied antiparallel I_z current of the same amplitude. (cf. Fig. 6A).

Fig. 7. End-on interferogram of Scylla IV-3 with $\ell = 1$ field over the 3-meter length.

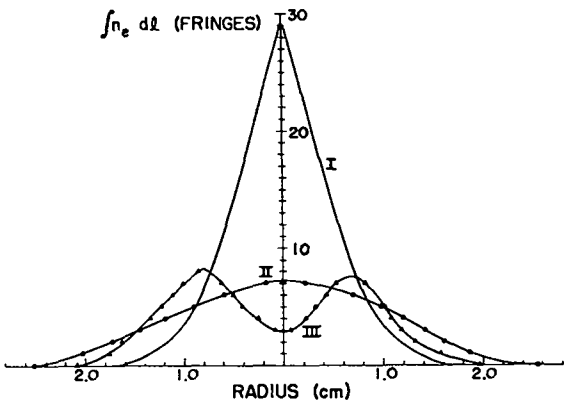

Fig. 8. Density profiles of Scylla IV-3. (I) With no helical field. (II) With helical field over the 3-meter length, no applied I_z. (III) With helical field and applied I_z.

Interferogram Results. Holographic interferometry has been used throughout these $\ell = 1$ helical field experiments to obtain the radial plasma electron density profiles integrated over the length of the plasma column. In the unstable cases, the

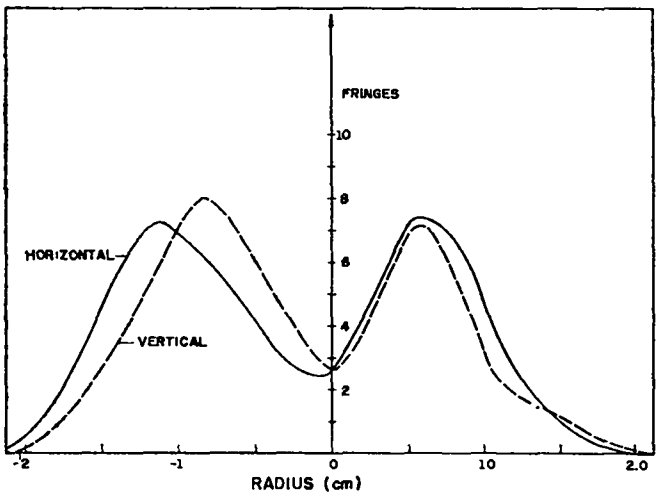

Fig. 9. Density profiles from interferograms of Fig. 7.

interferograms show the plasma column moving off axis and striking the wall in good agreement with the streak photographs. The interferograms have also been used to determine whether or not the plasma column is taking up a helical equilibrium distribution. If the plasma column takes up a helical form about the coil axis, the integrated radial plasma density profiles should show density dips in the center.

The holographic interferogram in Fig. 7 shows a fringe pattern taken 2 μsec after the beginning of the main discharge on the same shot as the streak photographs in Fig. 6C, i.e., with an 11.7-kA parallel I_z current. Graphs of the integrated plasma density profiles in the horizontal and vertical directions, reduced from this interferogram, are in Fig. 9 and their average in Fig. 8, Curve III. For reference, curve I shows the integrated profile with no $\ell = 1$ fields. Integrating over the plasma profile gives the total number of electrons in the discharge, 1.4×10^{18}, which compares quite well with the initial 12 mTorr deuterium filling pressure. This profile (Fig. 8-III) shows a pronounced dip in the central region of the integrated radial density distributions. The luminosity of the plasma column in the side-on streak photographs of Fig. 6C shows a maximum plasma diameter of 1.3 cm at the time the interferogram was taken. This is more than a factor of two less than the overall diameter of the density profile of Fig. 8-III. From the integrated plasma

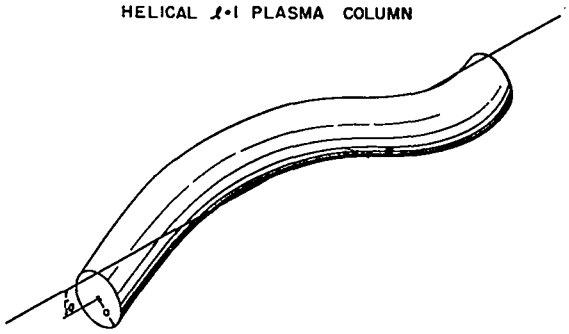

Fig. 10. Schematic diagram of $\ell = 1$ helical plasma.

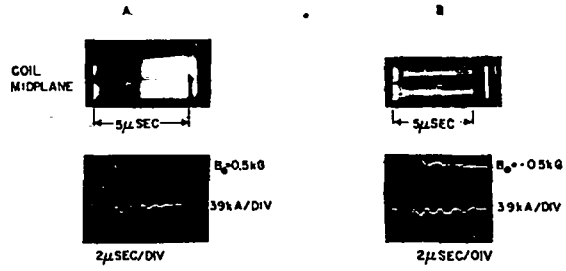

Fig. 11. Streak photographs and oscillograms of Scylla IV-3 with bias fields and $\ell = 1$ fields over the full 3-meter length.

density profile of Fig. 8-III and the plasma diameters from the streak photographs of Fig. 6C, it is concluded that the plasma column is taking up a helical form about the coil axis. Additional interferograms taken under similar conditions substantiate this conclusion.

An integrated plasma density profile obtained from an interferogram taken 2 μsec after the initiation of the main bank and without an applied I_z current pulse (cf. Figs. 7 and 6A) is shown in Fig. 8-II. Such interferograms taken of the plasma column in the absence of applied I_z current pulse do not show a dip in the center of the plasma density profile. These results indicate that, with an applied I_z of ~10 kA of either sign, the plasma column takes up a helical form about the coil axis (Fig. 10). In the absence of applied I_z, the helical displacement appears only as a broadening of the density profile.

Experiments with Initial Magnetic Bias Fields.

Magnetic bias fields with magnitudes of 500 G were applied both parallel ($+ B_o$) and antiparallel ($- B_o$) to the main compression field in the $\ell = 1$ grooved coil with initial deuterium filling pressures of 10 mTorr. In the case of negative bias field, the experiment was to determine if the $\ell = 1$ helical field could penetrate the plasma column during the strong plasma turbulence which occurs just after the initial implosion. With the negative bias field, the plasma stability was not as good as in its absence, although the neutron emission was greater. Without an applied axial current, the plasma column moved to the discharge tube wall in a sideways, $m = 1$, motion approximately 1.4 μsec after the start of the main field. This is to be compared with 2.2 ± 0.5 μsec in the absence of a negative bias field. With an applied I_z of ~ 11 kA, an improvement in the stability was observed as shown in the streak photographs taken at the coil midplane, Fig. 11A. The upper streak shows the plasma motion in the horizontal plane, while the lower one shows the motion in the vertical plane. The oscillogram shows the applied B_z (upper trace) and the I_z (lower trace). The plasma stability was not as good as with the same I_z in the absence of the negative bias field.

With a parallel bias field applied to the $\ell = 1$ grooved coil, a small $\ell = 1$ helical field is embedded in the preionized plasma before the implosion. This field is compressed with the plasma as the main field rises. Without an applied I_z, the plasma column moves to the wall in 3.2 ± 1.2 μsec, compared with 2.2 ± 0.5 μsec in the absence of a parallel bias field. The measured $\ell = 1$ induced current has a peak value of 2.2 kA compared to 4.0 kA without bias field. This reduced current indicates that the $\ell = 1$ helical field is embedded by the bias field before the implosion as conjectured above.

The application of an axial current, I_z ~ 11 kA, in addition to the parallel bias field, results in the stable plasma column shown in Fig. 11B. In this case the I_z was applied parallel to the induced current. The same stable plasma configuration was observed with the I_z applied in opposition to the induced current. This independence of the plasma behavior of the sense of I_z is in agreement with the previous results without bias magnetic fields.

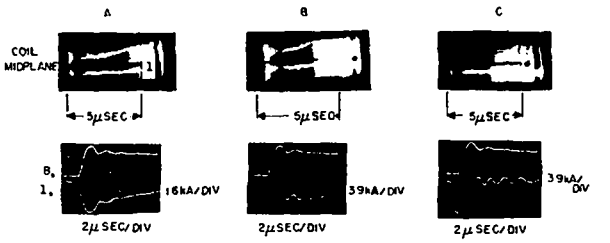

Fig. 12. Streak photographs and oscillograms of Scylla IV-3 with 50 mTorr filling pressure and axial currents for $\ell = 1$ field over the full 3-meter length.

Experiments with an Initial Deuterium Filling Pressure of 50 mTorr. In an attempt to improve the penetration of the $\ell = 1$ helical field into the plasma column the plasma temperature was decreased by increasing the initial deuterium filling pressure from 10 to 50 mTorr. In the absence of an applied I_z, the plasma column was more stable and exhibited a slower growth rate than in the 10 mTorr experiments as shown in the streak photographs of Fig. 12A. The plasma column underwent a sideways motion toward the discharge tube wall as before and struck the wall in 3.6 ± 0.2 μsec after the initiation of the main discharge. An axial bucking current of 5.1 ± 0.2 kA was observed. This current was approximately 25% greater than that measured with an initial filling pressure of 10 mTorr.

The application of an axial current, $I_z \sim 11$ kA, antiparallel, Fig. 12B, and parallel, Fig. 12C, did not appreciably improve the stability of the plasma over that observed without an applied I_z, Fig. 12A.

Analysis of Helical Interferograms. The helical grooves were designed to produce a plasma column shaped like an $\ell = 1$ helix with a helical displacement of about 1 cm. Such a column is shown in Fig. 10 for a plasma with radius a smaller than the helical displacement r_o.

The interferograms measure the optical path length of rays parallel to the helical axis. Since such rays go in and out of the helical column, the interpretation of the fringe shift is more complicated than for straight plasma columns.

It was pointed out by Harold Weitzner that, in principle, the column density and helical shift could be calculated by the formula:

$$n_e(r) = \frac{1}{L}\int_0^\infty k\,dk\,\frac{J_o(kr)}{J_o(kr_o)}\int_0^\infty r\,rd\,J_o(kr)N(r), \qquad (3)$$

where L = the length of the helical column (No. periods x λ), k is a dummy variable, J_o's are ordinary Bessel functions, and N(r) is the experimentally observed fringe shift as a function of r from the helical axis. The approach is awkward in practice because experimental errors prevent a perfect determination of N(r). Such errors lead to difficulties because the inner integral viewed as a function of k is not always zero when $J_o(kr_o)$ is zero. The ratio thus becomes divergent and $n_e(r)$ cannot be calculated.

To get around the problem of imperfect data, a nonlinear least-squares approach was chosen. The column was assumed to be adequately described by

$$n_e(r) = e^{-(r/a)^2}\left[\sum c_n r^{2n-2}\right], \qquad (4)$$

with $1 \le n \le 3$ (i.e., up to r^6) and r measured from the center of the column. Such a column with a helical displacement of r_o would give an experimental fringe shift:

$$N(r) = L\,e^{-\alpha}\left(\sum_n A_n I_n(\beta)\right) \qquad (5)$$

where

$$\alpha = \frac{r^2 + r_o^2}{a^2};\ \beta = \frac{2r_o r}{a^2};$$ r is measured from the helical axis; A_n depends on the set of C_n, r_o, and r; and I_n are the modified Bessel functions. With $n_e(r)$ containing terms up to r^6 there are six parameters in the problem:

r_o	= the helical displacement
a	= the Gaussian width
C_1	= the peak column density
C_2, C_3, C_4	= coefficients which determine the column shape.

The computer program "PACKAGE" from C-5 was then used to fit these six parameters to experimental data using Gauss's method of least squares.

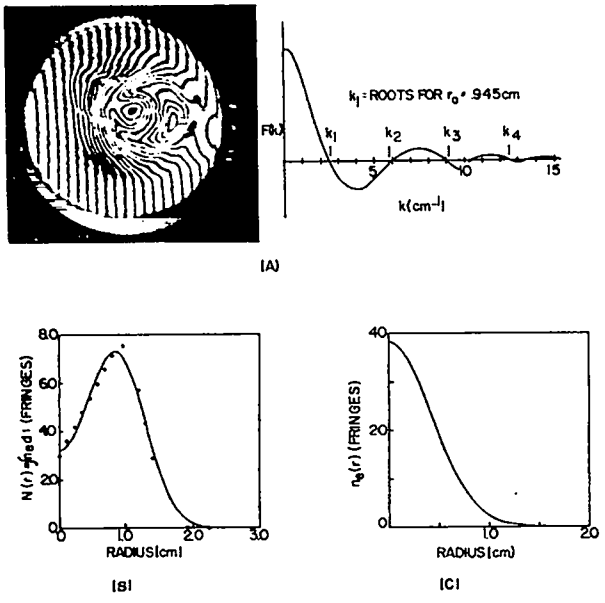

Fig. 13. A. End-on oscillogram of Scylla IV-3 plasma corresponding to Figs. 6C, 7, and 8-III. F(k) is the inner integral of Figs. 3 and 6. B. Fit to experimental points of end-on density profile of helical plasma. C. Derived plasma density distribution as function of radius from the helical axis. Data correspond to second row of Table I.

Actually it was convenient to begin by examining the inner integral

$$F(k) = \int_0^\infty r\, dr\, J_o(kr)\, N_{exp}(r). \qquad (6)$$

If the plasma is helical the zeros of this integral will come close to those of $J_o(kr_o)$ for some choice of r_o. Given this estimate of r_o, the analysis was finished by performing the least-squares fitting procedure.

As an example, the data from Figs. 6C, 7, and 8-III are interesting. The interferogram is shown for reference with F(k) in Fig. 13A. Figure 13B shows the experimental data for this integrated density profile along with the computer generated least-squares fit and Fig. 13C shows the column density profile implied by the fitted curve. Note that Fig. 11C gives the profile at a particular cross section rather than the integrated density profile. Referring to Fig. 13, we see that the interferogram has a dip in the fringe shift at the center which suggests a helical shape immediately. The graph F(k) does have zeros and it is simple to determine that if $r_o = .945$, the roots should be

$$k_1 = \frac{\text{Root No. 1 of } J_o}{r_o} = \frac{2.450}{.945} = 2.545$$

$$k_2 = \frac{\text{Root No. 2 of } J_o}{r_o} = 5.841$$

$k_3 = 0.158$

$k_4 = 12.478$, etc.

Of course the larger roots are associated with the fine grain structure of N(r) and thus become very sensitive to small experimental errors. It often happens that F(k) has zeros in addition to those which coincide with $J_o(kr_o)$, permitting various choices for r_o, but in this case there is only one reasonable interpretation.

In Fig. 13B the experimental data are seen to agree very well with the computer fit, although the fitted values of C_2, C_3, and C_4 were not significantly different from zero. These coefficients of higher powers of r were generally hard to fit because the helical curve, N(r), is not strongly dependent upon them when $a \approx r_o$. Looked at another way, the light goes in and out of the column in such a way as to integrate over the density profile; thus the fringe shift is rather insensitive to the exact shape of the column. It should be further noted that the least squares fit was done while simultaneously varying a, C_1, and r_o. A good fit was found with $r_o = .946 \pm .013$. It was further checked that when r_o is set at other values and held fixed, the fit gets much worse.

It should be noted that the experimental fringe shift in Fig. 13B never exceeds 8 fringes, whereas the peak density in the column would have produced nearly 40 fringes had the column not been helically displaced. The plasma column radius is fairly clear in Fig. 13B since r_o is larger than the plasma radius, but in other examples given below, the plasma radius can only be determined by the complete analysis. The conclusion may thus be

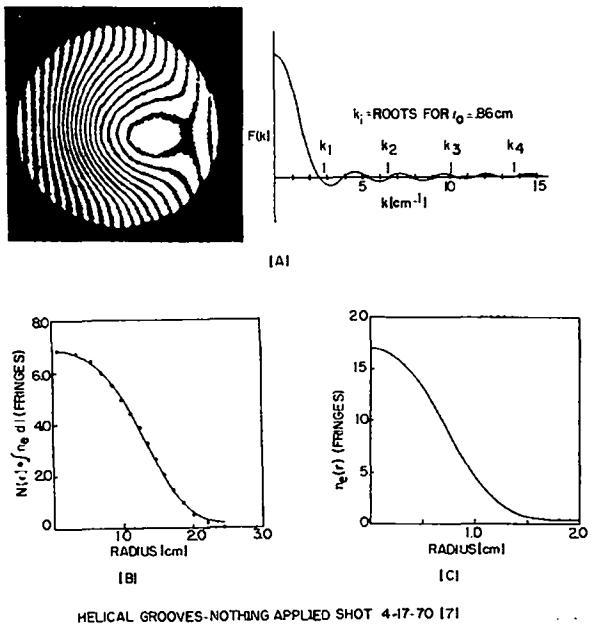

Fig. 14. Same as Fig. 13 except that data correspond to first row of Table I.

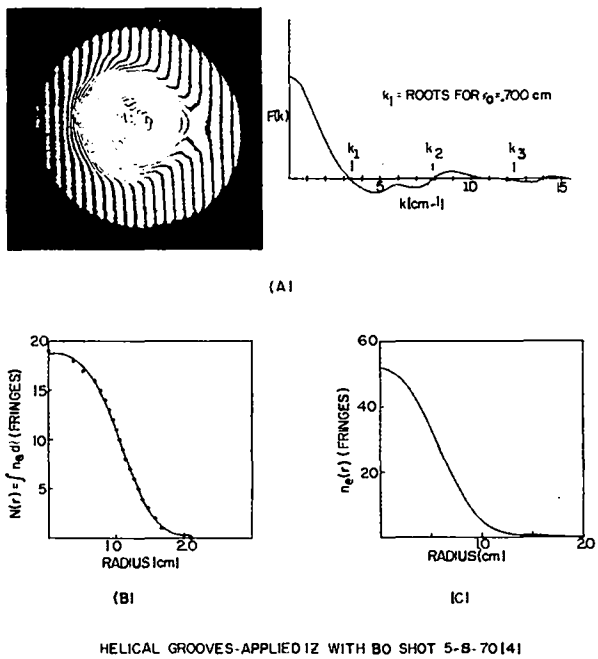

Fig. 15. Same as Fig. 13 except that data correspond to third row of Table I.

reached that if the plasma is in a helical shape its parameters are fixed rather well as given in Fig. 13C. Furthermore, since the side-on streak photos show a column diameter consistent with Fig. 13C and since simple arguments based on pressure balance predict a helical shape, there is only one reasonable interpretation of the interferogram: it is the end-on view of a helical plasma column. This is an important result because the z dependence of the plasma density is very hard to determine directly. This indirect method is rather easy experimentally and determines quite nicely the important parameters of plasma radius and helical shift.

Data for various experimental conditions are summarized in Table I and shown in Figs. 14 and 15. The entries in the table express average results from more than one analysis of a particular interferogram. In particular, each interferogram provides four estimates of N(r) as one reads up, down, left, and right from the center of the interferogram. The plasma radius $\bar{a}$ is defined by

$$n_o \pi \bar{a}^2 = \int n_e \, 2\pi \, r \, dr,$$

where n_o is the peak column density. The units of "fringes" on the density profiles are equivalent to 1.19×10^{15} electrons per cm^3 assuming the system is 270 cm long.

Discussion of Results. Using the values of $\delta_1 = r_o/a$ determined from the interferograms and crude estimates of β based on Scylla IV experience using a straight coil, it is possible to calculate the growth rate of the $m = 1$ instability.[2]

$$\gamma_1^2 = \delta_1^2 \, (hV_A)^2 \, (ha)^2 \, \frac{(2-\beta)(4-3\beta)}{8\,(1-\beta)}.$$

The results are compared with experiment in Table II.

TABLE I

Shot No.	Comments	r_o = helical shift	$\bar{a}$ = plasma radius	n_o = peak electron density in column
4-17-70 No. 7	Helically grooved coil Induced I_z observed. Nothing applied before main bank. 10 mTorr filling of deuterium	.86 ± .04 cm	1.00 ± .15 cm	1.8 ± .4 × 10^{18} cm^{-3}
4-27-70 No. 16	Helically grooved coil Applied I_z No initial B_z 10 mTorr filling of deuterium	.89 ± .09 cm	.55 ± .05 cm	4.4 ± .2 × 10^{16} cm^{-3}
5-8-70 No. 4	Helically grooved coil Applied I_z Initial parallel B_z 14 mTorr filling of deuterium	.69 ± .05 cm	.67 ± .07 cm	5.7 ± .5 × 10^{18} cm^{-3}
	Typical operation without helical fields 10 mTorr filling of deuterium	0	.70 ± .10 cm	4.0 ± 1.0 × 10^{18} cm^{-3}

TABLE II

Case	Estimated β	Calculated γ_1 MHz × 10^6	Observed γ_1 MHz × 10^6
Helical fields without applied I_z or B_o	0.7	2.1	3.0
Applied I_z	0.3	0.85	0.6
Applied I_z and B_o	0.1	0.35	0.2

We are inclined to interpret the variation of observed growth rate with applied I_z and B_o as being due to changes in plasma β brought about when the B_θ or B_z field interferes with the plasma implosion. Forthcoming experiments using driven $\ell = 1$ coils will include measurements of β to determine this variation.

The toroidal sector will be producing hot collisionless plasma in January, 1971, and we anticipate the first tests of toroidal equilibria at β values in the range of 0.5 or greater. Even though the toroidal sector will be end-loss limited, it will allow a test of the $\ell = 1$, $\ell = 0$ helical equilibrium and its stability during the ion thermal transit time from the ends of the apparatus. Values of $n\tau$ in the region of 10^{12} cm^{-3}sec at densities of a few times 10^{16} cm^{-3} and ion temperatures in the neighborhood of 5 keV are anticipated.

References

1. LA-4351-MS, p. 2.
2. F. L. Ribe and M. N. Rosenbluth, Phys. Fluids 13, 2572 (1970).

THREE-LASER HOLOGRAPHIC MEASUREMENTS ON SCYLLA IV-3 (P-15)

(F.C. Jahoda and R.E. Siemon)

The objective of this work is to provide interferograms at three different times during one shot on Scylla IV-3. As shown in Fig. 16, the arrangement involves a straightforward double-exposure holographic method with some particular details required by the three lasers: (1) the lasers are combined with beam splitters of various reflectivities in such a way that the plasma scene can be illuminated with one-third the intensity of any one of the lasers, (2) a reference beam from each laser arrives at a different place on the film plate, and (3) the scene beam is directed equally onto three individual film plates. This is accomplished with a transmission grating which gives about 5% of the incident intensity into each of the three orders shown. Each film plate is also exposed to the reference beam of one laser only. Thus when all three lasers are fired each laser makes a hologram on one film. Each film also receives the illumination of two other scene beams but fortunately this additional incoherent exposure does not destroy the hologram. Figure 17 is a photograph of the laser table with optics to form one scene beam and three reference beams.

We now feel we have a satisfactory system with the following characteristics: (1) three 20-nsec exposure interferograms can be obtained on each shot of Scylla IV, (2) since the three exposures come from individual lasers they may be taken at any time during the development of the plasma, and (3) the quality of the final interferograms permits resolution of at least 50 fringes/cm.

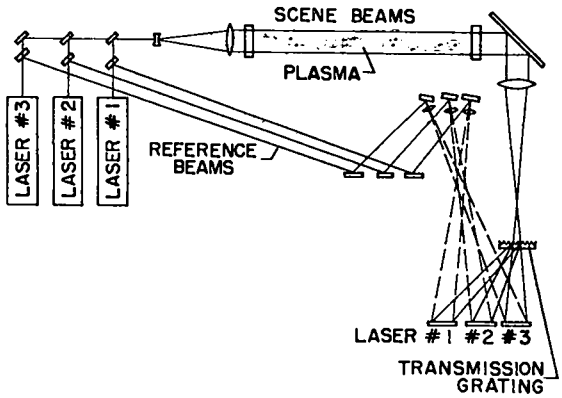

Fig. 16. Three-laser holographic apparatus

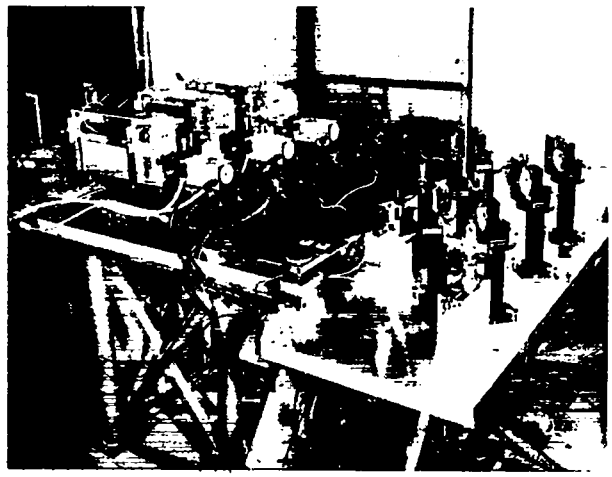

Fig. 17. Laser table with optics of three-laser holographic apparatus.

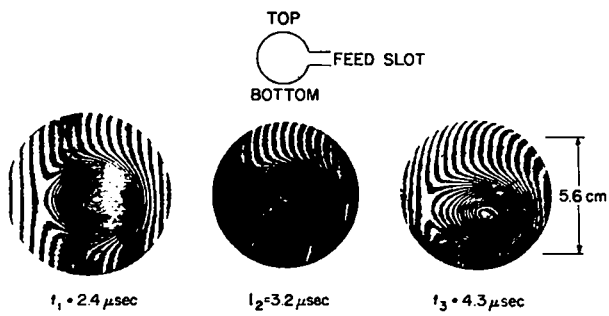

Fig. 18. 3-laser holographic interferograms of Scylla IV-3 with helical $\ell = 1$ coils.

Particularly important is the fact that in the final arrangement, holograms are obtained over quite a broad range of exposure levels. A procedure insensitive to the unavoidable variations of laser intensity and to the alignment difficulties characteristic of large machines was a prime consideration. Recent results are shown in Fig. 18 for a Scylla IV-3 shot in which helical coils were used.

$\ell = 0$ FEEDBACK SYSTEM FOR SCYLLA IV-3 AND SCYLLAC (P-15)

(R. F. Gribble, D. L. Call, R. E. Siemon)

We plan to pursue[1] an $\ell = 0$ MHD feedback experiment to control the $m = 1$ mode (discussed above in the Scylla IV-3 experiment) on a plasma column subject to $\ell = 1$ helical fields. The method has been discussed by Ribe and Rosenbluth,[2] and calculations concerning the feedback dynamics have been performed by Thomassen and Weldon, as summarized elsewhere in this report. The extent to which the $\ell = 0$ feedback coils must be driven will depend on the growth rate of the $m = 1$ instability observed in Scyllac. The present design is capable of correcting a growth rate of about 1 MHz. We plan to try it first on a linear θ pinch and then on the toroidal Scyllac sector. The system consists of three blocks as shown in Fig. 19: the position detector, the analogue arithmetic computer, and the power amplifier. The analogue arithmetic unit, now in the design stage, will have a gain of from 10 to 50 and an output of 10 volts. The power amplifier (including driver and final stage) is presently being designed and tested. This includes a power-tube protection crowbar on the final stage.

POSITRON DETECTOR. Preliminary work on a detector to track plasma column displacements using the plasma luminosity has been encouraging. A United Detector Technology SC-10 detector and amplifier have shown signals compatible with simultaneous streak photographs. Bench-top calibration of the detector with its amplifier imply that one should observe linear signals as the column moves as little as 1 mm or as much as 1 cm off axis, provided that the plasma brightness remains constant in time. First results indicate the plasma column luminosity is fairly constant, but this point will be carefully checked with the new apparatus.

THE ARITHMETIC "COMPUTER". The arithmetic unit will probably consist of four sections: the light level automatic gain control, a 45° rotational translator, an automatic "equilibrium" setter, and an output fan-out amplifier. A Silicon General

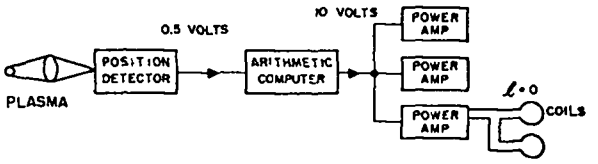

Fig. 19. Block diagram of feedback electronics for Scylla IV-3 and Scyllac.

SG-3402 fast IC amplifier with a fast gain control input will provide an almost true position output with the sum of light level signals applied to the gain control input. By obtaining the sum and differences of the two 45° position detector signals, vertical and horizontal position signals will be obtained. The "equilibrium" setter output will be proportional to the change in plasma position from an "equilibrium" value which is the plasma position at receipt of a control pulse, the time of which is predetermined (about 1 μsec following main bank start). This is accomplished by essentially feeding one position signal into both the normal and invert inputs of a differential amplifier up to the control pulse time. Following the control pulse, the invert input is held to its value at the time of the pulse. This is accomplished by inserting between the position signal line and the amplifier invert input a gated sample-and-hold circuit. The fan-out amplifier will drive the three power amplifier modules for one meter. Design and construction of the arithmetic unit is rather straightforward and will be delayed until the power-amplifier design is finished.

THE POWER AMPLIFIER. This is made up of four amplifier sections, a crowbarred capacitor power source, and a crytron pulse network for rapidly bringing vacuum-tube biases to a nearly linear region.

The driver consists of one transistor and two vacuum-tube stages feeding a driver output transformer which drives the grids of the final amplifier. The driver is ready for test in its breadboard version. The tape-wound-core output transformer is such that the driver can deliver 8-kV at 32 A to the final grids with a risetime of < 0.2 μsec.

The final amplifier uses two Machlett 8618 magnetic-beam triodes in push-pull, driving an output transformer wound on a 20 cm^2, 1-mil laminated, 50% Ni-50% Fe core. The turns ratio will be between 5:1 and 10:1, depending on output needs to the $\ell = 0$ coils, which are driven by the single-turn secondary. Measured risetime is < 0.15 usec. The expected outputs are > 500 A (plate) and > 5000 A (to coils) for 10:1 turns ratio.

COMPONENTS. Two power tubes for pulse modulation service were evaluated; the Machlett ML-8618V and the Eimac 4CW100,000E. The ML-8618 was accepted.

Both of the power tubes evaluated for the feedback experiment met the primary specifications: 500 A plate current, 45-kV dc holdoff, and low drive power. The Eimac 4CW100,000E has the major drawback of exhibiting a highly nonlinear and negative input impedance. Between plate currents of 200 and 300 A the negative grid current is most pronounced. With a swamping resistance across the input as low as 30 Ω, the plate current switches uncontrollably between 200 and 300 A for sufficient input drive. Negative feedback improves the performance, but enough feedback to make the tube useful requires a prohibitive amount of input drive. Another problem with the tube was breakdown between screen and grid terminals at the voltage required for high plate currents.

The ML-8618 was pulsed to 500 A at 20 kV on the plate. The grid current appears to be positive for plate currents to 500 A and plate voltages less than 40 kV. The only problem observed to date with the one ML-8618 tested is high-voltage instability. This problem may be due to an arc that occurred early in the life of the tube when the crowbar failed. The tube was aged for 100 h with the dc plate voltage increased in steps to 50 kV. After 100 h the tube withstood 50 kV without arcing for 10 h. However, it has recently been observed that the tube will hold 40 kV dc indefinitely but arc shortly after the plate is pulsed to more than 300 A.

The 70 ML-8618 tubes will start to arrive about February 1, 1971, at a rate of about 10 per month (5 initially, 15 later). The agreed time for acceptance or rejection is 30 days, and the tubes must be aged for 100 h before they can be rejected because of insufficient hold-off voltage. Consequently it was considered necessary to be able to break in 3 tubes simultaneously. A 3-tube test stand has been designed and is in the process of construction. One 30-kV and two 50-kV suppliers in addition to one driver will provide high-voltage aging and high-voltage, high-current pulse testing at a maximum rate of about 20 tubes per month.

Three kinds of tape-wound core materials of several tape thicknesses were tested for the final output transformer before settling on the final core design, which has been ordered.

References

1. LA-4351-MS, p. 20.

2. Phys. Fluids 13, 2572 (1970).

SCYLLA IV-3 EXPERIMENTS WITH DRIVEN $\ell = 1$ AND $\ell = 0$ COILS (P-15)

(K. S. Thomas, W. R. Ellis, Jr., C. R. Harder, H. W. Harris)

As a sequel to the experiments with $\ell = 1$ fields produced by helical grooves, we are designing a new experiment with driven $\ell = 1$ windings in order to gain better control over the penetration of the helical field and the induced I_z current. The $\ell = 1$ system consists of 10 wavelengths of $\ell = 1$ coils driven in parallel by a capacitor bank consisting of 18, 1.85-μF, 60-kV capacitors. After studying the driven $\ell = 1$ system we intend to add driven $\ell = 0$ coils in order to study the $\ell = 0, 1$ feedback force to be used to control the $m = 1$ instability of the helical system. The $\ell = 0$ capacitor rack and associated structure for its triggering system have been installed.

Epoxy-potted $\ell = 1$ coils have been prepared for this experiment. Each coil consists of two copper windings of helical wavelength $\lambda = 30$ cm in a hollow epoxy cylinder (Fig. 20). The outer surface of the coil is a machined sleeve of epoxy-impregnated fiberglass, which forms the outer portion of a mold in which the two helical windings are placed. The inner surface is an acrylic cylinder. The windings are wrapped before potting with 1-mil polyester (Mylar) tape and heat cured at 400°F. They are then covered with fiberglass sleeves which center them between the two mold cylinders. Vacuum potting is done with Epon 815 epoxy + 15% D-40 hardener + 5% LP-3 polymerizer to reduce brittleness. The coils test under dc (Hypot) to 100 kV and also withstand 100 kV induced voltage from the Scylla I-A coil.

Fig. 20. $\ell = 1$ coil for Scylla IV-3.

SCYLLAC INSTALLATION AND TESTING (P-15)

(W.E. Quinn, C.F. Hammer, W.A. Bradley (Eng-7), R.A. Haarman (Eng-7), E.M. Little, A.S. Rawcliffe, G.A. Sawyer)

INITIAL CONFIGURATION OF SCYLLAC. Figure 21 shows the initial configuration of Scyllac, now under construction. It consists of a 5-meter toroidal sector (Racks 11, 12, 13, 14, and 15, South to North) and a 5.5-meter linear θ pinch with 2:1 mirrors in the end regions where the magnetic field is increased by a factor of 2, to nearly 200,000 gauss. The toroidal sector is now undergoing final electrical checkout, and installation of racks and air system for the linear device is complete.

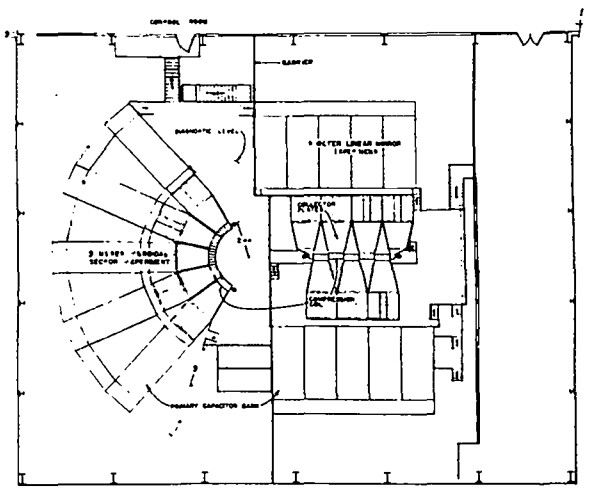

Fig. 21. Initial configuration of Scyllac.

The major part of the installation has been done by LACI crafts under the Zia Company and Eng-4 supervision. In this section we outline parts of the installation and testing done by P Division personnel.

SCYLLAC COLLECTOR PLATE ASSEMBLY. Six collector plate systems have been assembled and leak tested during this report period. In addition, the initial collector plate assembly was reassembled with new Mylar sheet insulation after an electrical fault developed on Rack No. 13. Five collector plate systems have been installed in the 5-meter toroidal sector. The sixth assembly is a spare for this device. The compression coil sections and the coil-collector plate transition sections have been installed on the collector plate assemblies for all five racks. The assembly of the first collector plate for the linear device is well under way.

SCYLLAC TOROIDAL SECTOR INSTALLATION AND TESTING (P-15)

(W. E. Quinn, C. F. Hammer, G. A. Barnes (P-16), R. Baldonado, H. M. Crane, L. H. McDowell, and A. S. Rawcliffe. W. A. Bradley and R. A. Haarman (Eng-7)

Testing and checkout of the completed portions of the 5-meter toroidal sector have been carried out on a 6:00 to 10:00 pm night schedule since the beginning of August. This arrangement has allowed the checkout to be accomplished without interference with the construction of the toroidal sector. The testing and checkout of Racks 12, 13, and 14 have been completed and that of Rack 11 is in process.

COMPONENT INSTALLATION. Following the completion of work on each rack by the LACI electricians and plumbers, LASL technicians perform certain final installations and checks. These installations and checks include the items discussed below in the various systems for each rack of the device.

Capacitor Bank Systems. The polyflow air lines are connected from the various spark gaps to the appropriate air supply and exhaust manifolds. On each rack this includes four lines from each of the 210 start and crowbar spark gaps. On the pre-ionization (PI) bank and crowbar (CB) trigger bank, small distribution manifolds are made and the respective 18 and 48 air lines connected. In the trigger systems air line connections are made to the various buffer triggatron gaps, the pulse charge gaps, master trigger gaps and the submaster trigger gaps. In addition, flush valves with their associated air control lines are installed for each of the gaps in the trigger chains. The air line connections are made to all shorting balls and their operation checked.

An electrical check is made on each of the 245 spark gaps in each rack to insure that each trigger cable is properly plugged into the spark gap.

Each of the 245 spark gaps and the associated trigger gaps in each rack are filled with insulating oil. A "teacup," filled with insulating oil, is installed over the charge connections exterior to each spark gap.

Trigger Systems. For each of the trigger systems on each rack, (a) the master trigger, (b) primary triggers, (c) crowbar triggers, and (d) PI triggers, the following components are installed: a pulse charge buffer triggatron-transformer unit; a pulse charge capacitor and spark gap; and a master buffer triggatron-transformer unit. The interconnecting cables between these units and to the trigger tank in a given system are dressed and installed.

The master and submaster trigger gaps are inspected for proper cable connections, closed up and filled with insulating oil.

Collector Plate Systems. The collector plates have been assembled and installed by P Division personnel. Following the completion of the collector plate cabling by the LACI electricians, LASL technicians fill all cable cartridges with oil, fabricate and connect an oil reservoir fill system for the cable cartridges on the bottom of the collector plate, and fabricate and connect a SF_6 supply manifold to feed SF_6 insulating volumes in the cable cartridges and tie-through bolts. The collector plate coil transition sections and coil sections are installed by P Division personnel.

TEST AND CHECKOUT OF RACKS 12, 13, AND 14

Each of Racks 12, 13, and 14 has been checked out. In each rack the following systems were tested individually: (1) PI trigger system followed by the PI bank; (2) primary master trigger system and primary submaster trigger system; (3) crowbar master trigger system followed by the operation of the complete crowbar trigger system; and (4) primary bank system.

Component Faults. A summary of component faults is as follows: (a) 19 shorted capacitors of which 12 were Sangamo, 5 Aerovox and 2 McGraw-Edison; (b) 10 shorted primary trigger cables having 8 faults at the end of the outer braid terminations and two body faults (untested cables); (c) only 5

shorted RG 17/14 source cables; and (d) 10 shorted RG 14/59 crowbar trigger cables, (untested cables). There was a failure of 11 Sangamo capacitors out of a total of 46 (24%) in Rack No. 13. After failure, a "tapping" test suggests that the Sangamo capacitors might be low on oil. The system testing confirms the earlier capacitor testing at the High Voltage Test Facility and the Gap Test Facility, showing that the Aerovox is a better capacitor than the Sangamo and the McGraw-Edison units.

These tests show that the cable pretesting program for the RG-17/14 source cables and the RG-17/14 load cables has been very worthwhile. There have not been any faults in the 1368 load cables and only 5 faults in the 450 source cables. Previous experience on Scylla IV with the installation of cables which had not been pretested showed a loss of approximately 10% of load cables and 20 to 30% of source cables.

The loss of the primary trigger cables (special RG-17) and crowbar trigger cables (RG-14/59), which were not pretested, is approximately as anticipated. The replacement of crowbar trigger cables is relatively easy while that of the primary trigger cable is somewhat more difficult.

System Problems. The usual problems have occurred in the control system. Excessive voltage drops in the dc control circuits due to long lengths of control wiring have been corrected. Difficulties with power supply breakers tripping because of the initial surge currents drawn by light-bulb ballasted power supplies have been corrected by the installation of fuses. Some logic functions in the control system interlock circuitry have been revised. A fault in the control system which turned power supply circuits on in a discharge mode has been repaired.

Considerable difficulty was encountered in keeping the primary bank trigger cables plugged into the load spark gaps. This problem results from both the required cable routing and the stiffness of the special RG-17 trigger cable. K. Hanks has designed a molded nylon clamp, which will attach to the top of the load gap and firmly hold the trigger cable in place. However, CMB-6 plastics has not been able to deliver any of these clamps in the past two months. On the 5-m toroidal sector a less elegant, but simple, clamping arrangement has been fabricated and installed. An additional difficulty with the trigger cables was an arc breakdown from the outer braid termination up along and through added vinyl and shrinkable tube insulation to the top spark gap flange. This problem has decreased considerably since the addition of the trigger cable clamp.

In the submaster-type trigger gap, an intermittent breakdown occurred between the center and top gap electrodes along the surface of a polyethylene "wrap" insulator. This breakdown was unexpected from our previous experience. To eliminate the possibility of it reoccurring, a simple insulating "hat" cut from the bottom of a dime store plastic basket has been and is being installed on all submaster-type trigger gaps.

The high-voltage meter multiplier, located in the trigger tank, in the PI bias circuit was destroyed by an electrical transient. This problem was eliminated in all trigger tanks by relocating the HV terminal of the meter multipliers in both the bias and cable charge test circuits to a point back of an isolation resistor, where there is some protection from transients.

A failure in a crowbar shorting ball assembly occurred due to a high-voltage track developing in the phenolic base. Nylon, a better insulator, has been substituted in some assemblies. In others, a design modification has allowed the use of the original phenolic base. Another difficulty in the PI and crowbar shorting balls has been a breakdown across the shorting ball assembly. This has been corrected by modifying the assembly to allow approximately an inch-deep layer of oil to cover the "hot" ball in the charged state.

The liquid charge resistor assemblies have required some additional electrical insulation to withstand the high voltages which develop in prefire situations.

One of the most potentially serious problems which has developed is that of "loose" charge lead connections to the capacitors inside the primary load spark gaps. Two types of

failures have occurred: (1) failure at the charge-lead solder connection and (2) failure at the treaded charge-lead connection to the aluminum alloy base spark gap electrode. These charge connections may carry large currents in a prefire situation and when the spark gaps extinguish. Lock washers are presently being used on the threaded connection and the charge connection has been redesigned. Liquid 300-Ω resistors, each capable of absorbing 21 kJ, are being installed in the charge leads to each capacitor to limit current in the charge system in the event of a prefire or capacitor short.

Collector Plate Fault. During the initial tests on Rack 13 an insulation breakdown occurred in the collector plate. The failure was caused by a lack of SF_6 insulating gas in the vicinity of a tie-through bolt in the collector plate skirt area. The necessary SF_6 connection had not been made before the area was covered with sheet insulation. The damage to the collector plate components was minimal. However, the fault required the removal and reassembly of the collector plate in order to replace the Mylar sheet insulation which is continuous throughout the plate area. The entire removal and replacement of the collector plate assembly including cabling took 140 man hours.

Arcing has been experienced at current joints between the transition section and collector plate as well as at the coil closure. It appears that this difficulty may be partially a result of the mechanical assembly involving tolerances in the current joint regions and the insulation thickness. However, the basic difficulty is that the Scyllac current joint carries an unprecedentedly high number of coulombs from each bank discharge.

CHARACTERISTICS OF THE RACK. A 1-m long, 10.5-cm bore compression coil is being used in the electrical testing of each energy storage rack.

Preionization (PI) Bank. The preionization capacitor bank (per meter) consists of nine 0.7-μF 75-kV capacitors whose spark gap switches are each connected into the rear of the collector plate with 12 RG-17/14 coaxial cables (average length = 7.8 m). The PI bank oscillates at 318 kHz ($\tau/4$ = 0.78 μsec) and produces an initial peak field of 8.7 kG (with V_{cap} = 60 kV) with an exponential damping factor of $e^{-9.78 \times 10^4 t}$ in the absence of plasma. The azimuthal electric field E_θ is 405 V/cm (with V_{cap} = 60 kV) at a radius of 4.3 cm. The bank has a source inductance of 28.84 nH compared with the coil inductance of 10.76 nH, giving a transfer efficiency of 0.27. The PI source inductance consists of 6.67 nH in the capacitor-spark gaps, 11.14 nH in load cables, 3.54 nH in cable cartridges, and 7.49 nH in the collector plate and coil feed.

These results suggest that the PI bank could be reduced in size from nine to perhaps five capacitors. With five capacitors in the PI bank, the above results extrapolate to a PI frequency of 357 kHz with an initial magnetic field maximum of 5.5 kG and an E_θ of 283 V/cm with the bank charged to 60 kV.

Primary Capacitor Bank. The primary capacitor bank consists of 210 1.85-μF 60-kV capacitors per meter. The primary bank spark gap switches are each connected into the collector plate with 6 RG-17/14 coaxial cables (average length = 6.8 m). The complete primary bank has been fired only with the crowbar system. The primary bank charged to 55 kV produces a magnetic field of 102 kG in the compression coil with a rise time of 3.85 μsec and an initial azimuthal electric field of 0.95 kV/cm at a radius of 4.3 cm. The crowbar system extends the magnetic field in time with measured e-folding times of up to 280 μsec. The average e-folding time for 15 discharges was 220 μsec. This time varies somewhat from discharge to discharge, depending on the timing and simultaneity in the firing of the crowbar gaps. Figure 22 shows an oscillogram of the magnetic field waveform in the 1-meter compression coil. The crowbarred waveform shows an initial peak-to-peak modulation of about 10%.

The source inductance of the primary bank is 4.70 nH with 0.29 nH in the capacitor-spark gaps, 0.83-nH in the load cables, 0.30 nH in the cable cartridges, and 3.38 nH in the collector plate and coil feed. The system has an energy and voltage transfer efficiency of 0.70 into the 10.5-cm diameter coil (coil inductance = 10.76 nH).

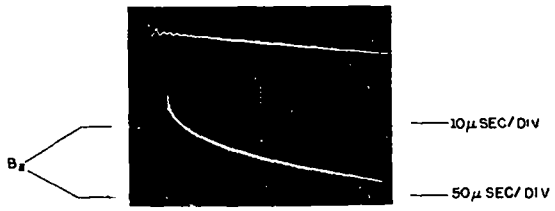

Fig. 22. Crowbarred current waveforms of one rack and coil section of Scyllac.

Vacuum Systems. One of the two vacuum systems for the toroidal sector has been assembled and is being tested. These systems employ both a turbomolecular pump and a Vacion pump in a manner similar to those used in the Scylla IV system. The assembly of the second vacuum system has begun.

Neutron Detectors. Both plastic scintillator-photomultiplier detectors and silver activation counters are being fabricated to monitor neutrons for the toroidal experiments. The power supplies, line drivers, and scalers to be used with the silver counters have been fabricated by A. T. Brousseau.

SCYLLAC COMPUTER AND DATA ACQUISITION (P-15)

(G. A. Sawyer, D. Brown (P-1), J. W. Lillberg, M. J. Seamon (C-4), D. M. Weldon)

During this period the Scyllac computer was moved from the Scylla IV area to the Scyllac building. The Scylla IV gap monitor is now operating with the computer over a long cable.

The spark gap monitor system has also been installed in the first five racks of Scyllac and had been operating satisfactorily during Scyllac checkout. Some minor noise pickup problems have been discovered in the prefire detect section of the gap monitor. This section has been redesigned and is being installed. The Scyllac spark-gap monitor system has also been placed under computer control. The computer will sort out gaps that are not firing within acceptable jitter limits and list them. The experience with the monitor system on an actual operating theta pinch is proving to be important in understanding electrical interference problems as we go into Scyllac operation.

Development of the programming for the Scyllac computer has continued. The plot routines using the CRT display system are in final form. Basic routines for monitoring spark-gap firing time, reading scan converter tubes, and meter reader analogue-to-digital converter have been developed. Typical displays are samples of tables of spark-gap firing data and sample plot routines for displaying single and multiple graphs and oscillograms from the scan converters.

SCAN CONVERTERS AND TRANSIENT RECORDERS FOR SCYLLAC (P-15)

(J. W. Lillberg and R. F. Gribble)

All necessary drawings and printed circuit films for the dual tube version of the analogue section of the scan converters have been sent to ARF Products at Raton for production of the first eight modules (16 scan converter tubes). The prototype unit has been sent to Raton for a few weeks to be used as a production model to demonstrate wire routing. ARF has started production on the first eight dual analogue modules and all eight modules are expected in January. Testing of the scan converter system has begun.

Mechanical drawings and a prototype have been made of the scan converter controller. The wiring and cable tabulations have been written and are being modified as prototype test proceeds.

An interface capable of handling four Biomation Model-610 transient recorders has also been designed and is currently under construction.

ESTIMATED MIRROR RATIOS FOR THE SCYLLAC LINEAR DEVICE (P-15)

(W. E. Quinn)

Mirror ratios for the Scyllac linear device are estimated by scaling the parameters of the mirror section from a 1-meter module of the central coil region. The mirror ratio R_m is given by

$$R_m = \left(\frac{\alpha_m}{\alpha_1}\right)^{\frac{1}{2}} \left(\frac{C_m}{C_1}\right)^{\frac{1}{2}} \left(\frac{\ell_1}{\ell_m}\right)^{\frac{1}{2}} \frac{b_1}{b_m} \frac{V_m}{V_1} , \qquad (1)$$

where the subscript m refers to the mirror section and the subscript 1 to a 1-meter module of the central coil region. The transfer efficiency is α (the ratio of the coil inductance to the sum of the coil and source inductances), C is the capacitance of the bank energizing the coil, ℓ is the length of the coil, b is the coil radius, and V is the capacitor bank voltage. Taking $\ell_1 = 100$ cm, $\ell_m = 20$ cm, and $b_1 = b_m = 5.25$ cm gives

$$R_m = 2.24 \left(\frac{\alpha_1}{\alpha_m}\right)^{\frac{1}{2}} \left(\frac{C_m}{C_1}\right)^{\frac{1}{2}} \frac{V_m}{V_1} . \qquad (2)$$

Furthermore, if we make the assumption that $\alpha_1 = \alpha_m$, take $C_m = C_1$, i.e., the mirror coil is energized with one rack of the Scyllac device (720 kJ) which energizes each meter of the central coil, and take $V_m = V_1$, a mirror ratio, $R_m = 2.24$, is attained. The magnetic field in the mirror coil would be approximately 250 kG. The mirror coil must be placed relative to the main coil such that most of the magnetic field lines from the main coil pass through the mirror coil while the extra mirror lines return through a gap between the two coils. The mirror ratio can be increased by decreasing the radius of the mirror coil relative to the central coil. However, this requires a transition in the diameter of the discharge tube. The above assumption that transfer efficiencies are equal ($\alpha_1 = \alpha_m$) is a reasonably good approximation since both the mirror coil inductance and the source inductance of its current feed will be larger than the corresponding inductances of the 1-meter central coil section.

The rise time of the field in the mirror coil relative to that of the main coil is given by

$$\frac{\tau_m}{\tau_1} = \left(\frac{\alpha_1}{\alpha_m}\right)^{\frac{1}{4}} \left(\frac{C_m}{C_1}\right)^{\frac{1}{4}} \left(\frac{\ell_m}{\ell_1}\right)^{\frac{1}{2}} \frac{b_m}{b_1} \left(\frac{\ell_1^2 + 4b_1^2}{\ell_m^2 + 4b_m^2}\right). \quad (3)$$

With $b_m = b_1 = 5.25$ cm and $\ell_m = \ell_1/5$,

$$\frac{\tau_m}{\tau_1} = 2.0 \left(\frac{\alpha_1}{\alpha_m}\right)^{\frac{1}{4}} \left(\frac{C_m}{C_1}\right)^{\frac{1}{2}}. \quad (4)$$

If, as above, we assume $\alpha_1 = \alpha_m$ and take $C_m = C_1$, $\tau_m/\tau_1 = 2.0$. This is satisfactory since the mirror field can be initiated simultaneously with that of the central field and can continue to rise after the central field is crowbarred.

Another quantity of interest is the current line density at the mirror coil, which is given relative to the main coil by

$$\left(\frac{I_m}{\ell_m}\right) \Big/ \left(\frac{I_1}{\ell_1}\right) =$$

$$\left(\frac{\alpha_m}{\alpha_1}\right)^{\frac{1}{4}} \left(\frac{C_m}{C_1}\right)^{\frac{1}{2}} \left(\frac{\ell_1}{\ell_m}\right)^{\frac{3}{2}} \frac{b_1}{b_m} \left(\frac{\ell_m^2 + 4b_m^2}{\ell_1^2 + 4R_1^2}\right)^{\frac{1}{2}} \frac{V_m}{V_1} \quad (5)$$

With $b_m = b_1 = 5.25$ cm and $\ell_m = \ell_1/5$,

$$\left(\frac{I_m}{\ell_m}\right) \Big/ \left(\frac{I_1}{\ell_1}\right) = 2.5 \left(\frac{\alpha_m}{\alpha_1}\right)^{\frac{1}{4}} \left(\frac{C_m}{C_1}\right)^{\frac{1}{2}} \frac{V_m}{V_1}. \quad (6)$$

With the assumptions above $\alpha_m = \alpha_1$, $C_m = C_1$, $V_m = V_1 \cdot \left(\frac{I_m}{\ell_m}\right) \Big/ \left(\frac{I_1}{\ell_1}\right) = 2.5$. In central region of the coil, the current line density will be approximately 88 kA/cm. This predicts a current line density of ~ 220 kA/cm at the mirror coil. This will require a careful design to prevent arcing at the current-feed joints of the coil.

SCYLLAC-TYPE FEEDBACK SYSTEM (P-15)

(D. M. Weldon and K. I. Thomassen (MIT, Summer SM)

The system proposed by Ribe and Rosenbluth for feedback control of the $m = 1$ instability on the Scyllac $\ell = 1$ helical plasma column involves the programmed excitation of weak $\ell = 0$ fields in various phases (along the z axis) to produce compensating forces in various directions. Analytical and computer studies have been carried out to determine the limits of stability for feedback forces proportional to plasma displacement, as well as its derivative, the transverse velocity. An LA report is being prepared.

EQUILIBRIUM CONFIGURATION OF THE SCYLLAC 5-METER TOROIDAL SECTOR EXPERIMENT (P-15)

(F. L. Ribe, W. H. Borkenhagen, (P-16), W. R. Ellis, and K. S. Hanks (P-16))

The first portion of the Scyllac θ-pinch experiment to be placed in operation is the 5-meter toroidal sector whose compression coil is shown in Fig. 23. It produces a toroidal equilibrium by means of: (a) an $\ell = 1$ helical field ($\delta_1 \approx 1$) produced by capacitor-driven windings, (b) a smaller $\ell = 0$ field ($\delta_0 \approx 0.1$) produced by flux-shaping annular grooves in the compression coil, and (c) a circuit for driving longitudinal current I_z is also provided for equilibrium during the implosion phase of the discharge when the $\ell = 0$ and $\ell = 1$ fields may not yet be operative. A more detailed view of the arrangement of $\ell = 1$ coils and $\ell = 0$ grooves is shown in Fig. 24. An LA report describing the system in detail is being prepared.

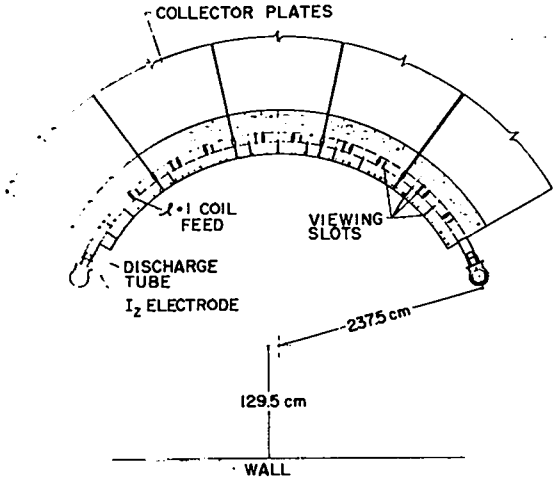

Fig. 23. Top view of compression coil and discharge tube of 5-meter Scyllac toroidal sector.

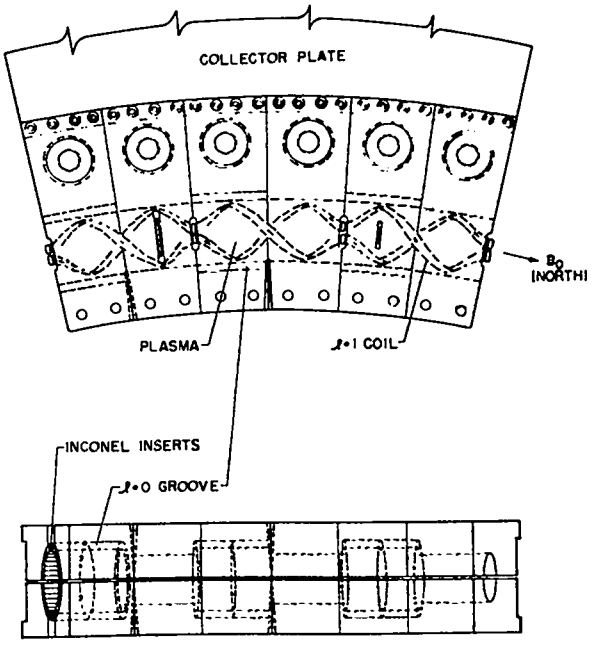

Fig. 24. Arrangement of $\ell = 1$ coils and $\ell = 0$ grooves in Scyllac toroidal sector.

FAR-INFRARED DIAGNOSTICS (P-15)

(R. W. Peterson and F. C. Jahoda)

HCN LASER AT 337 μ. The past year marked the beginning of work to develop a capability in far-infrared interferometry. The following is a brief summary of advantages and disadvantages of this wavelength region along with a description of progress and goals.

The far-infrared region (50 μm - 500 μm) is well suited for density measurements in the range $\int n_e \, d\ell \simeq 10^{12}$ to 10^{16} cm^{-2} and thus provides a considerable extension of the usual sensitivity range for the visible and near-infrared. At the lower end, this bridges the gap to the microwave range while maintaining inherently better spatial resolution capability because of the shorter wavelengths. Until recently, far-infrared interferometry has been hindered by the lack of a strong source of monochromatic radiation, but the recent discovery of molecular laser transitions has provided a variety of available wavelengths (e.g., HCN at 337 μ, 128 μ, H_2O at 118 μ, 79 μ, 48 μ; H_2S at 225 μ, 193 μ; ICN at 773 μ, 676 μ, 538 μ; etc.). Wavelengths > 300 μ have the further advantage over the shorter infrared region of being easily transmitted by crystalline quartz.

In spite of the above advantages, difficulties abound in the far-infrared. A major problem involves fast detection of such low frequency radiation. Detection systems featuring 0.1-μsec response times have recently been developed, but require liquid helium temperatures and large magnetic fields for peak responsivities (our system is described below). Because of the relatively long wavelengths, diffraction sets the limit on the spatial resolution which can be obtained. For example, the diffraction effects produced by a 10-μ pinhole at 4000 Å can be produced by a 1-cm "pinhole" at 400 μ.

The power supplies and discharge tubes for both pulsed and CW laser action in the far-infrared have been purchased from Far Infrared, Inc. Both modes of operation have been achieved for the strong HCN transition at 337 μ. Our "fast" detector system (0.1 μsec) has been purchased from Advanced Kinetics, and consists of an InSb crystal cooled to 1.8°K by liquid helium at ≃ 12 Torr and placed in a 6-12 kG magnetic field produced by a superconducting magnet. In addition, we are working with a pyroelectric detector which operates at room temperature, and has a frequency response up to at least 1 kc.

Our initial attempts were to construct a far-infrared version of the double-cavity laser interferometer at 337 μ. Such a system is relatively simple and very sensitive to small plasma density changes. The limits on its usefulness are set primarily by the achievable spatial resolution of a few mm by its cut-off frequency corresponding to $\sim 10^{16}$ cm^{-3}.

CW operation was studied with variations in discharge current, gas pressures, gas ratios (i.e., partial pressure ratios of CH_4 and N_2 for HCN), and laser mirror surfaces. The steadiest HCN discharge at maximum output was achieved with a 2 to 1 ratio of methane to nitrogen at a pressure of 400 mTorr and a discharge current from 0.8 to 1.0 A. In the case of H_2O, a significantly lower pressure (200-300 mTorr) and higher currents (1.3 to 1.5A) are required for laser operation. Rough estimates from our detector responsivities indicate CW outputs in the 1 mW region.

Some time has been devoted to studying standard methods of far-infrared optics, i.e., how does one efficiently transmit, focus, and reflect the submillimeter radiation from our laser. CMB-6 has been helpful in the construction of lenses molded from polyethylene and TPX (a methyl-pentene polymer). Beam splitters have been made from thin sheets of Mylar (typically 3 mils for 50% transmission). Light pipes and corner reflectors have been constructed of polished brass.

With careful control of gas pressures, gas mixtures, and discharge currents, we have achieved very clean feedback signals with our apparatus in a double cavity configuration. It has been found that some troublesome laser beat phenomena can be minimized by careful longitudinal tuning of the laser. Figure 25(a) shows a slow and a fast sweep taken during feedback operation.

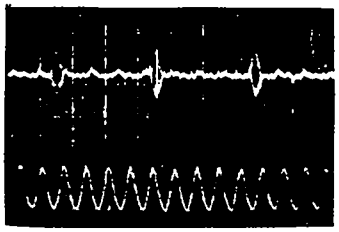

10 MILLISEC/DIV.

10 μ SEC/DIV.

150 KHZ HCN REFERENCE SIGNAL
(b)

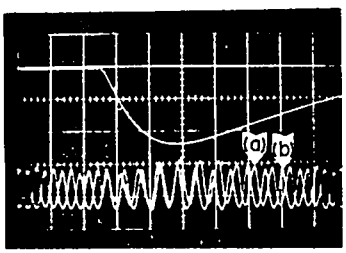

PLASMA LUMINOSITY
10μSEC/DIV.

10μSEC/DIV
SWEEP(a) - PLASMA
SWEEP(b) - NO PLASMA

DENSITY MEASUREMENT
(a)

Fig. 25. (a) HCN laser feedback modulation on slow sweep (top trace) and fast sweep (bottom trace).

(b) Plasma density measurement by time distortion of feedback modulation.

The envelopes of the upper trace correspond to complete revolutions of the rotating corner mirror. Each fringe of the fast lower trace corresponds to an optical path change sufficient to change the phase in the external cavity by 2π radians. These two traces allow an interferometric determination of the laser output wavelength accurate to better than 1%. The maximum fringe frequency we have obtained is mechanically limited by our ability to change the external cavity length; however, noise-free fringes at 160 kHz have been obtained.

In an effort to demonstrate the fractional fringe capability of this interferometer for studying plasmas lasting 10-100 μsec, we have used it to measure a low density plasma formed in a simple pulsed discharge tube. 30-50 mTorr of argon are excited in a 10-in.-long 2-in. i.d. tube with brass electrodes near each end. The discharge is produced by a 1-μF capacitor charged to 6 kV which is triggered by a spark gap. A 20-Ω resistor is placed in series with the load cable in order to slow down the discharge to $\sim$20 μsec.

Figure 25(b) shows the effect of such a plasma on the reference fringe pattern. Fringe shifts are measured relative to the second reference fringe pattern. Fringe shifts are measured relative to the second reference trace which is recorded with no plasma. It is possible to measure shifts of 1/20th of a full fringe. The phase change in radians produced by a density $n(cm^{-3})$ at 337 μ is given by

$$\varphi_{337}(\text{radians}) = 9.5 \times 10^{-15} \int_0^L n d\ell \ .$$

Thus when transversing the plasma of length L twice, our minimum measurable line density is found from,

$$\frac{2\pi}{20} = 2 \times 9.5 \times 10^{-15} \int_0^L n d\ell$$

or

$$\int_0^L n d\ell \Big|_{min} = 1.6 \times 10^{13} \text{ cm}^{-2}.$$

In the case of our discharge tube, where $L \simeq 25$ cm, we obtain

$$n(cm^{-3})\Big|_{min} \simeq 7 \times 10^{11} \text{ cm}^{-3}.$$

Densities of this order have been measured from data similar to that of Fig. 25(b). Our time resolution is still limited to $\sim$ 6 μsec by the angular velocity of the rotating mirror. Spatial resolution of the 337-μ beam in the present experiment is close to 1 cm.

DIAGNOSTICS AT 10.6μ (CO_2 LASER)

A GaAs crystal has been used to electro-optically modulate the phase of the reference beam in the CO_2 laser interferometer of Hammel, et al. We have used the rotating corner mirror version of a coupled cavity CO_2 interferometer to make an absolute calibration of the phase changes produced by the crystal in situ at frequencies comparable to the plasma application.

Assuming a refractive index $n_o = 3.28$,[1] the resulting value of the electro-optic coefficient, $r_{41} = (1.40 \pm 0.12) \times 10^{-10}$ cm/V (95% confidence) compares favorably in magnitude and precision with values in the literature obtained more laboriously from intensity modulation measurements with polarization analyzers. This generally applicable technique is being reported in a short note to Review of Scientific Instruments.

Reference

1. C. J. Johnson, G. H. Sherman, and R. Weil, Appl. Opt. 8, 1667 (1969).

HOLOGRAPHY (P-15)

(F.C. Jahoda)

Passing mention was given in the 1969 Annual Report to an in-place, dry-processing photopolymer recording technique, reported by Hughes Research Laboratories,[1] that promised elimination of the tedious photographic processing of every holographic exposure. Besides convenience, such capability would represent significant improvement in the utility of procedures that now require exact repositioning, such as the consecutive frame "live" fringe method. Our own attempts at preparing the chemicals were promising enough to maintain our interest, but not really successful.

During this year we have been successful with sample solutions furnished by Hughes. The sensitivity is approximately 1 mJ/cm^2 (better than Kodak 649F, not quite as good as Agfa Gevaert 10E75), and the diffraction efficiency and resolution are very high. Signal-to-noise ratio is worse than with photographic emulsions (some of this is inherent to phase recording, as distinguished from amplitude recording of holograms, and some to an unidentified milky precipitate), but this is quite tolerable for interferometry, where the only "gray-scale" requirement is adequate fringe contrast for readout. Hughes can furnish material at an equivalent cost per exposure significantly less than the cost of our photographic plates. The obstruction to widespread use, apparently, is that the user must mix together two solutions, each of long shelf life when unmixed, within 1 h before exposure, spread the mixture between glass plates to approximate a photographic plate, and pre-expose the results to an equivalent fog level in order to remove certain initial inhibitors to the photo-chemical reaction. In practice, these steps can be carried through quite simply.

An abbreviated explanation of the photochemistry follows. A red-sensitive dye (methylene blue), after absorbing a photon, has a high probability of crossing from its normal singlet state to an excited triplet state which is metastable. In the triplet state, it has a higher oxidation potential and produces free radicals in a reaction with p-toluenesulfinic acid. The free radicals, in turn,

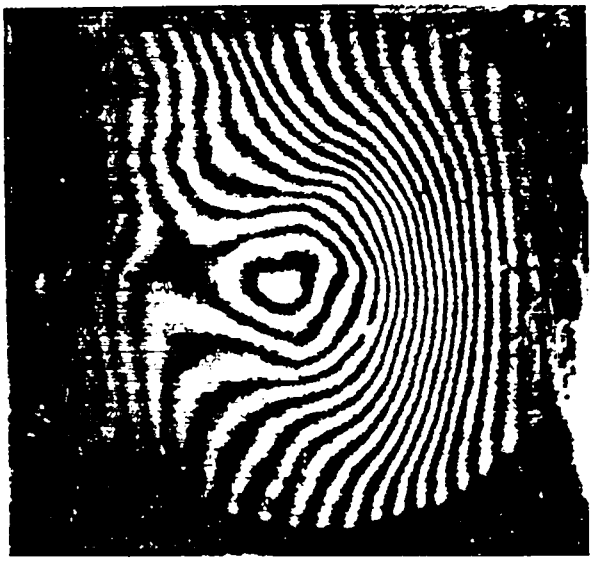

Fig. 26. Scylla IV-3 interferogram reproduced from photopolymer exposure.

initiate polymerization of barium and lead acrylate monomers. The monomers are water soluble, whereas the polymer precipitates out. The process is stopped (fixed) either by continued weak exposure that drives the polymerization to conclusion, or by desensitizing the dye with components that result from uv exposure of another constituent, p-nitrophenylacetic acid. The precipitated polymer has an altered refractive index and its spatial distribution after exposure to interfering coherent light beams constitutes a phase hologram.

Figure 26 is a copy of the polaroid print produced by white-light illumination of the photopolymer with lens-pinhole selection of the first diffracted order, in situ, immediately after the usual two consecutive laser exposures on a Scylla IV-3 plasma experiment. Immediately after the implementation of this technique, however, we converted to the three-frame holographic interferometry (reported elsewhere in this report) and thereby suffered enough additional light loss to render this technique impractical in routine use.

Reference

1. D. H. Close, A. D. Jacobson, J. D. Margerum, R. G. Brault and F. J. McClung, Appl. Phys. Letters 14, 159 (1969).

CRYOGENIC ENERGY STORAGE

(Henry L. Laquer (P-8))

The cost of conventional capacitive energy storage makes capacitors at their present stage of development an unlikely choice for generating the magnetic fields needed in pulsed thermonuclear reactors and in some larger scale plasma physics experiments.

Inductive magnetic energy storage with superconductors or cryogenic aluminum conductors may present a more economical alternative, provided a number of technological problems can be solved; among these are:

(a) High voltage cryogenics

(b) Stability or stabilization of superconductors under transient fast discharge conditions.

(c) Fabrication of "high temperature" 20°K superconductors into usable shapes and forms.

(d) A high current "circuit breaker" to transfer the energy from the inductive storage to the load coil.

Some progress has been made on items (a) and (d) of this list in a cooperative program with the LASL cryogenics group.

A cryogenic aluminum coil was operated successfully in liquid hydrogen under pulse conditions at 100 kJ and 10 kV.[1]

One approach suggested for the high current transfer switch or circuit breaker is also cryogenic, i.e., a superconductor which changes to the normally resistive state. Analysis of various storage and switching configurations has shown that the volume (V) and hence minimum cost of such a switch is related to maximum voltage (E), maximum current (I), supercurrent density (J_c) before switching, and normal state resistivity (ρ_n) after switching, through the equation

$$V \doteq E\, I/J_c^2\ \rho_n.$$

Experimental work is under way to determine the shortest possible switching times for various materials and switching parameters such as magnetic field, current density, and temperature. It appears that switching times of

2 or 3 μsec are readily achievable and that shorter times may be possible with material of sufficient thinness to permit rapid flux penetration. At the present, the analysis of these experiments is complicated by the lack of more than a phenomenological description of the so-called "flux flow state" where resistance appears in a superconductor.

Reference

1. E. Lady, D. Call, Proc. of the Intersociety Energy Conversion Conference, Las Vegas, Sept. 1970.

SCYLLAC ENGINEERING (P-16)

(E. L. Kemp et al.)

The installation of the Scyllac energy system began in January 1970. Installation actually consists of three phases: evaluation and testing of all electrical components, installation into the Scyllac building, and electrical debugging and checkout of the installed hardware.

All capacitors, cables, and spark gaps were evaluated for design performance and tested in mockup systems before they were installed in Scyllac. Two special facilities were established to perform these critical tests and manned by engineers and technicians. The installation of all hardware was performed by skilled crafts. Electrical checkout is being done by the Scyllac operating crew of engineers, physicists, and technicians.

There will be two independent experiments in the first phase of Scyllac: a 5-meter toroidal sector experiment and a 7-meter linear experiment. The toroidal experiment is being put into operation first. All fifteen capacitor racks have been installed, five racks forming a 120° toroidal sector and ten racks aligned for the linear experiment as is shown in Fig. 27.

The power supply system and the control system, which are common to both experiments, were completely installed. The toroidal racks

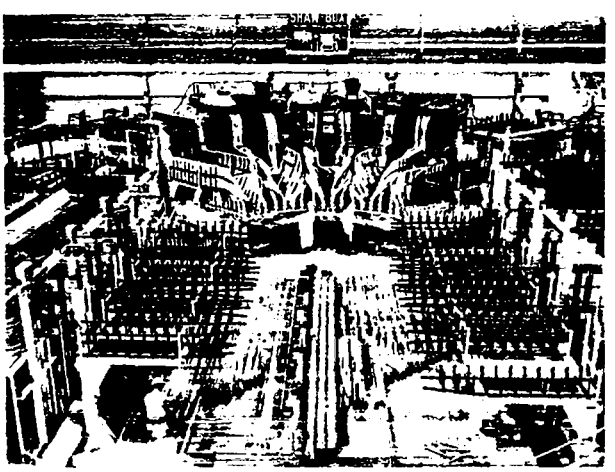

Fig. 27. Alignment of racks for linear experiment with 120° toroidal sector and associated energy storage racks in background.

were loaded with capacitors and each rack checked out as an integral unit. This was accomplished by allowing the installation crafts to work during the day and checking out at night. Checkout of the first rack was completed in ten weeks; subsequent checkouts are taking about three weeks per rack.

The checkout has revealed very few component or design problems--considering the fact that all the major components in the system had to be developed for this application. The first five racks contain essentially only Aerovox 1.85-μF 60-kV capacitors and their performance is excellent. Similar capacitors built by Sangamo and McGraw-Edison have not been as reliable in preinstallation evaluation. The piggyback-crowbar spark gap developed by R. F. Gribble, C. F. Hammer, and D. L. Call operates better than expected as indicated by the long 280-μsec, L/R decay time of load current. The 6000 installed load cables contain over 150,000 ft of cable and not a single load cable has yet failed in operation. The two types of cartridge terminations are operating satisfactorily. The trigger system is also performing well within the design requirements. The only serious problem so far encountered has been the charge lead connections to the spark gaps. This problem was solved by installing an electrolytic resistor in each capacitor charge lead. Plasma physics experiments in the toroidal sector are scheduled to begin in February 1971.

The total cost of the Scyllac project will be about $8.94 million, an overrun of $440,000. That overrun was principally due to increased costs for some of the hardware and an unprecedented rise in installation costs. A request has been made to the AEC for the additional funds required to finish the project. Meanwhile, the installation of the linear system will begin at the rate allowed by the existing funds.

As plasma physics experiments begin on Scyllac, it seems appropriate to identify some of the personnel responsible for this milestone. The capacitors and cable were developed by G. P. Boicourt. The start and crowbar spark gap was developed by Gribble, assisted by Hammer and Call. The cartridge terminations were developed by K. W. Hanks and Boicourt. The trigger system was initially designed by Gribble and fully developed by Hammer. The design team project engineer was W. A. Bradley. Structural design was performed by J. D. Allen and component installation design was performed by J. J. Banta. R. A. Haarman designed the charging system and A. S. Rawcliffe designed the control system. The collector plate system was designed by Hanks, and W. H. Borkenhagen designed the stabilization hardware. The data acquisition system was developed by Gribble, D. Brown, J. Lillberg, G. A. Sawyer, and D. M. Weldon. Checkout is directed by W. E. Quinn, assisted by Hammer, A. S. Rawcliffe, and Sawyer. The scientific project leader is F. L. Ribe and the engineering leader is E. L. Kemp.

SUMMARY OF YEAR'S ACTIVITIES IN THEORY AND NUMERICAL SIMULATION OF PLASMA (P-18)

(W. B. Riesenfeld)

This year has seen gains in understanding the equilibrium and stability properties of toroidally confined high-beta plasma, and the nature of the heating process and attendant instabilities in laser pulse heated plasmas. In addition, the scope of the program in numerical simulation of Vlasov plasmas has broadened considerably with the development of new codes to attack more realistic problems of interest to CTR and related projects. Finally, several applications of new techniques to other fields have proved possible, such as a new variational approach in the analysis of the mode spectrum of classical many-particle systems with full electromagnetic interactions, a new theory of rigorous invariants to solve the exact equations of motion in certain classical and quantum mechanical systems, and numerical techniques in integrating the Fokker-Planck equation to solve the astrophysical problem of the spherically symmetric contraction of a gravitationally interacting star cluster. Approximately thirty publications on these and other topics were made in appropriate professional journals and conference proceedings.

Of special interest is the magnetohydrodynamic analysis of the toroidal theta pinch of Scyllac type, using rotationally transformed multipole fields to balance the toroidal expansion force and thus achieve equilibrium. The equilibrium requirements of such a system and its stability relative to transverse displacement of the plasma column have been studied for a fairly realistic model in which the pressure profile is diffuse, and the results have been compared with those of earlier models based on a sharp boundary between the magnetic field and the plasma. In particular, the configuration uses a dominant $\ell = 1$ multipole field to produce finite displacements of the plasma column from cylindrical symmetry. Growth rates of the $m = 1$ modes (transverse motion) are small enough to be stabilizable by appropriate feedback systems; their action, in addition to more conventional dynamic stabilization schemes, have also been analyzed. Similar MHD analyses have been made for toroidal z-pinches with diffuse pressure and field profiles, and for the equilibrium and trapping of high-beta plasma in the injected quadrupole experiment, along with the effect of dipole shielding of the ring supports. A two-dimensional code has been written to study the dynamic implosion phase of theta pinches. This code will be used to gain information about the implosion of helically symmetric pinches with realistic transport coefficients.

The interaction of the rf electric field of a laser beam with a collisionless, homogeneous, underdense plasma has been studied; linearized growth rates were calculated and verified by numerical simulation. Simulation runs have been extended into the nonlinear regime through several stages of excitation and saturation of streaming instabilities, throughout which electron heating was observed. A two-dimensional electromagnetic simulation code has been written to study laser-radiation induced instabilities in a plasma with a density gradient. Finally, an estimate that is based on solution of a parameterized Fokker-Planck equation has been made of the direct collisional ion heating and thermonuclear reaction rate of a multi-ion species plasma. That estimate has been compared with collisionless ion instability heating; this last item of work was mostly accomplished outside the group.

The advances in the CTR-related numerical simulation of Vlasov plasmas were in the following areas: multi-dimensional beam and beam-plasma interactions, anomalous resistivity and turbulent heating connected with current and field driven instabilities, two-dimensional electromagnetic simulation with application to the Weibel electron anisotropy instability, isolation of a new high-beta electron cyclotron drift resonance instability of large growth rate, the effects of high amplitude rf fields, and the incorporation of binary collisions into Vlasov codes.

MAGNETOHYDRODYNAMIC STABILITY OF HIGH BETA PINCHES (P-18)

(J. P. Freidberg)

SCYLLAC STABILITY WITH DIFFUSE PROFILES (With B. M. Marder)

The encouraging sharp boundary MHD results for the $\ell = 1$ Scyllac configuration have been extended to include diffuse profiles. It is found that if the condition

$$\frac{1}{B_o}\frac{dB_o}{dr} > 0$$

is satisfied, where B_o is the θ-pinch field, then the leading order $m = 1$ term in δW vanishes for $\ell = 1$ as it did in the sharp boundary case. This implies that, at worst, the plasma is very weakly unstable. For any $\ell \neq 1$, the leading order term does vanish and is destabilizing. The above condition is a weak one requiring only that B_z be hollow and not reverse.

IMPROVED SHARP BOUNDARY THEORY FOR SCYLLAC

A new sharp boundary theory was formulated which recovers both previous sharp boundary theories, in the appropriate limits, in addition to extending the range of parameters over which the theory is valid. The intent was to develop a more accurate theory for detailed comparison with experiments. First results indicate that the old ordering, in which the helical shift is assumed small and the helical coil is assumed tightly wound, yields results which are closer to the newer, more exact theory. A more recent ordering theory, which assumes large helical shifts and loosely wound helical windings, predicts greater stability than found in the newest calculation. This is slightly surprising since the parameter range of interest is, on the surface, more closely approximated by the new rather than the old ordering. Further results will be forthcoming to delineate which regions of parameter space are accurately described by which theory.

STABLE "STABILIZED Z-PINCH" PROFILES

Z-pinch profiles have been calculated which satisfy Suydam[1]'s criterion and are completely MHD stable. The profiles are similar to those obtained at Culham Laboratory. Typical profiles are characterized by a 10% reversal in B_z, and a maximum $\beta \approx 20\%$. These profiles are consistent with old Perhapsatron data as well as recent data from the fast z-pinch. In the process of calculating these profiles we have derived the following useful form for Suydam[1]'s criteria by eliminating p' from the pressure balance equation

$$\left[B^1_z - \frac{B_z}{r}\left(\frac{rB^1_\theta}{B_\theta} + 3\right)\right]^2 > \frac{8(B_z^2+B_\theta^2)}{r^2}\left(1 + \frac{rB^1_\theta}{B_\theta}\right).$$

We see that if $rB^1_\theta/B_o < -1$, Suydam's criterion is automatically satisfied; that is, the old intuition of wanting B_θ to fall off faster than $1/r$ does indeed guarantee that Suydam's criterion will be satisfied.

NUMERICAL STUDIES OF THE HELICALLY SYMMETRIC THETA PINCH (P-18)

(T. A. Oliphant, H. Weitzner (NYU), F. L. Ribe (P-15))

In order to understand experimental results recently obtained on the helically symmetric version of Scylla IV-3,[1] and to be able to predict plasma behavior as variables are changed, a numerical program has been written for studying such a device using dissipative magnetohydrodynamics. The mathematical formulation has been thoroughly described by H. Weitzner. For computational convenience, the fluid and electromagnetic equations have been written in a rectangular coordinate system. At present the fluid equations are being solved by the PIC[2] method, with the benefit of close consultation with T-3. The electromagnetic equations are being solved by the SØR method. The general helical equations have been included in the code and have been thoroughly checked for computational symmetry. Shock wave propagation has been checked only in the cylindrically symmetric limit. A well-defined shock front propagates toward the center of the plasma under the pressure of the driving field. However, the reflected shock wave, which propagates back out, develops certain apparently mesh-determined asymmetries. The present view is that these asymmetries arise because of an inadequate treatment of mesh cells containing the boundary between the plasma and the magnetic field. Therefore, a special boundary treatment has been included and is being checked out.

References

1. LA-4599-MS.

2. Anthony A. Amsden, "The Particle-in-Cell Method for Calculation of the Dynamics of Compressible Fluids, LA-3466.

Z-PINCH

SUMMARY OF Z-PINCH ACTIVITIES (P-14)

The effort on the z-pinch has been accelerated during the past year. The group has concentrated on one large toroidal experiment which is now under construction. We have also been given theoretical support from P-18 in understanding pinch stability and equilibria.

In the fast linear z-pinch experiment, plasma heating is accomplished by a strong shock. The B_θ magnetic field rises two to three times faster than in hot θ-pinch experiments. Measurements give plasma temperatures of 750 eV at ion densities $\sim 3 \times 10^{15}/cm^3$. In addition, the plasma column exhibits stability for ~ 8-μsec after which the current decays to zero. This report covers changes made in the experiment by increasing the length of the discharge tube from 30 cm to 63 cm and describes new techniques developed to attain the desired level of operation.

The results from the linear system have encouraged us to construct a shock heated toroidal z-pinch experiment. The primary purpose of this experiment is to avoid electrodes and end effects. In addition, the toroidal geometry has marked advantages for z-pinches in that it has azimuthal symmetry and exhibits stable equilibria. A short description of this experiment appears below (Phillips et al.).

Numerical z-pinch calculations (Haberstich) are being performed using a one-dimensional MHD code in an attempt to duplicate the magnetic field and density profiles as well as the z-current and voltage observed in the linear shock heated z-pinch experiment. These calculations will give us a better understanding of the processes taking place in these discharges.

The MHD stability of the linear z-pinch has been examined (Freidberg, P-18). Completely stable diffuse magnetic field profiles have been found. The β of the confined plasma may be as high as 20%.

The numerical technique (D. Baker, P-18) for calculating ideal MHD equilibria (developed for toroidal multiples) has been extended to handle asymmetric equilibria with perfectly conducting boundaries. The equilibrium for the toroidal z-pinch has been calculated for a class of z-pinches with hollow pressure profiles and reverse B_z field outside the pinch column. These distributions closely match those required for stability and are similar to those found in the linear experiment.

We have again become interested in using metal discharge tubes in our z-pinch experiments. Metals have important advantages over ceramics as the duration of plasma confinement is extended. The results with an aluminum tube are described (Phillips).

Our investigation of methods of high frequency dynamic stabilization of the z-pinch has been completed. We report (Forman, et al.) the results of using an oscillating B_z magnetic field.

FAST z-PINCH (P-14)

(J. N. DiMarco, L. C. Burkhardt)

INTRODUCTION. This experiment is being performed in an attempt to achieve a high temperature (keV) z-pinch. Heating is accomplished by driving a strong shock through the plasma. It is therefore required that the z-pinch be driven by a system capable of supplying a few thousand joules in a time scale faster than the sonic transit time (approximately 0.5 μsec). A low inductance energy source is utilized employing the technique of magnetic energy storage.[1] This system is capable of supplying current at a rate of 2×10^{12} A/sec with voltages of ~ 80 kV and peak currents of 200 kA. At an initial deuterium pressure of 30 mTorr, shock velocities ~ 4×10^7 cm/sec are measured. The plasma temperature, as determined by pressure balance, is ~750 eV. These results are developed in a previous report.[2]

This report will present the changes that have been incorporated in the linear pinch in order to simulate the operation of the shock heated toroidal z-pinch experiment that is now under construction. Some new techniques have been developed to attain the desired level of operation.

DESCRIPTION OF EXPERIMENT. A schematic representation of the experiment is shown in Fig. 28. Deuterium gas flows continuously through the system; it is preionized by a 28-MHz, 300-W oscillator. The level of ionization is increased by a preliminary 25 kA axial current pulse of 13 μsec half-period. This current is removed from the pinch by means of a crowbar applied at the end of the first half-cycle. The rapid main current transfer is timed to occur approximately 3 μsec after the end of the first half cycle of the preionization current pulse. A description of the operation of a magnetic energy storage system is given elsewhere.[1]

When the switch is closed the energy is transferred into the 145 nH storage inductance. This inductance occurs in the capacitors, coaxial cables, headers, and parallel plate transmission

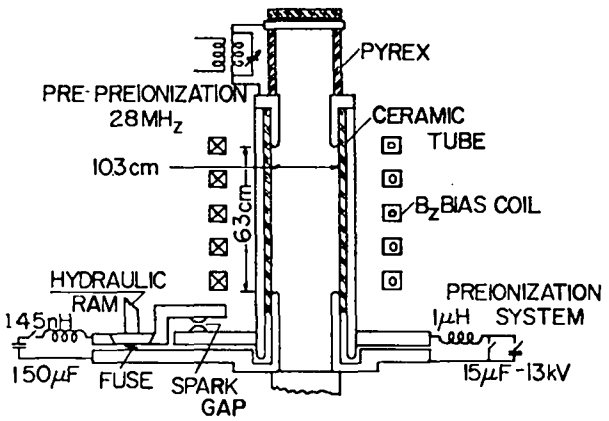

Fig. 28. Schematic of high temperature (keV) linear z-pinch experiment.

line. The majority of the inductance, however, is associated with the parallel plate transmission line so as to isolate the capacitor bank from the high voltage generated across the fuse. The fuse typically consists of a copper foil 1 mil thick, 10 cm wide, and 15 cm long. Conductor-fuse interface continuity is maintained by a 9-ton hydraulic press which holds the short section of transmission line in contact with the top of the fuse. An illuminated dry air gap switch is used to transfer the current from the storage inductance into the z-pinch. It operates at atmospheric pressure and the gap is illuminated by a current-limited (~ 0.1 A) discharge located within the top electrode. The switch is not triggered but rather is allowed to break down spontaneously. The breakdown voltage is found to be very reproducible (± 5%).

The discharge tube is made of 99.8% alumina and has a wall thickness of 0.47 cm. Electrodes are made from 304 stainless steel with a wall thickness of 0.635 cm. Optical access is achieved by using tubular electrodes. The return conductor is made from an aluminum cylinder of wall thickness 1.27 cm. Assembly is achieved by splitting the cylinder along the axis and clamping the halves together with stainless steel clamps. These clamps then serve as flux conservers during the lifetime of the z-pinch, but allow the slow B_z bias field to penetrate the 0.3-cm gap in

the return conductor. The bias magnetic field is produced by a solenoid external to the discharge tube, and has a half period of 3 msec.

To simulate the operation of the shock heated toroidal z-pinch experiment, the discharge tube length is doubled to 63 cm to match the length of a quarter-section of the torus. The storage inductance is increased to 145 nH and the total energy initially stored in the capacitor bank is doubled. The capacitor bank is set up as a two-state Marx system following the predictions of a numerical code which was developed as an aid to determining the desired operating conditions.

EXPERIMENTAL RESULTS. In order to maintain the same operating characteristics while doubling the length of the discharge tube, it is required that the initial $\dot{B}$ and total plasma current remain the same. This then demands that the voltage and energy handling capability of the magnetic energy storage system be doubled to 70 kJ.

Considerable difficulty is encountered as the energy level increases. The most difficult problem developed in the fuse package. The design[1] that worked well with the short tube no longer gave reliable operation. The violence of the explosion that resulted when the fuse vaporized caused considerable damage to the high voltage insulation in spite of re-entrant traps that were designed into the system to catch the molten copper.

This problem was attacked in two ways. The efficiency of the transfer was improved by reducing parasitic inductance between the fuse and the z-pinch so that more voltage is developed across the discharge. Also, a numerical calculation was performed using an experimentally determined relation as the equation of state for the fuse.[1] The transfer gap was therefore redesigned because it was found that 33% of the pinch voltage had developed across the gap. This increased the voltage across the z-pinch by 10%. The numerical calculation enabled the transfer efficiency to be increased by 20%. The net result, being a 30% improvement in overall efficiency, allowed the total stored energy to be reduced from 70 kJ to 50 kJ. Unfortunately, even at this energy level the fuse operation was unreliable.

After discussing the problem with G. Schenk at the Laboratori Gas Ionizzati we adopted a new technique. That part of the copper foil that vaporizes is now placed in contact with glass beads of 100-170 μ diameter, instead of the fiber-glass cloth used in the previous design. The violence of the explosion is drastically reduced as measured by the lower noise level and the reduced perturbation of the area surrounding the fuse. Also the fuse is no longer centrally located between the transmission lines but is moved over to one side and extends outward from between the transmission lines. The result is that the molten copper can now be prevented from damaging the high voltage insulation. The fuse design is also made simpler by making only one fold in the copper foil and inserting a single sheet of 1/16 polyethylene between the folds. This new design produces consistent transfers at the 70-80 kV and 200 kA level.

The stability of the plasma column is determined by observing the signal from a loop that measures the B_z flux inside the discharge. The occurrence of a jump in flux is then associated with a kink mode instability. So far, stable periods from 4 to 8 μsec have been observed depending on experimental conditions. An experiment using 90° Thompson scattering of a ruby laser light is being set up to determine the plasma temperatures.

Reference

1. J. N. DiMarco and L. C. Burkhardt, J. Appl. Phys. 41, 3894 (1970).

2. LA-4351-MS.

THE SHOCK HEATED TOROIDAL Z-PINCH EXPERIMENT (P-14)

(J.A. Phillips, et al.)

The high temperature toroidal z-pinch[1] experiment has been designed and is being assembled. An artist's conception of the experiment is shown in Fig. 29.

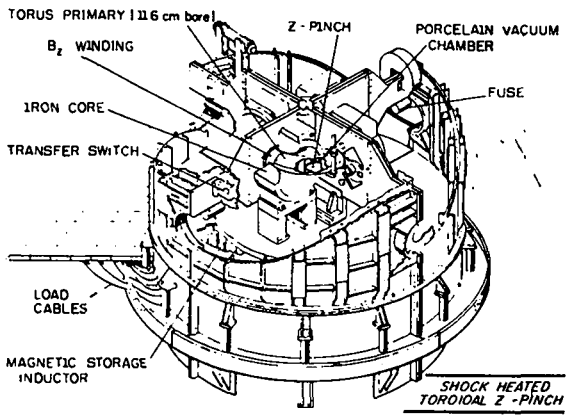

Fig. 29. Artist's conception of the high temperature toroidal z-pinch device.

Each quadrant of the torus approximates the dimensions and electrical characteristics of the present linear experiment. The magnetic energy storage technique as developed for the linear experiment is used. The large (244-cm-diameter) coaxial conductor connects the four fuses with low inductance to force the voltages developed across the fuses to be identical. A coaxial inductor, ~36 nH, is common to the four quadrants and stores the magnetic energy.

The design parameters of the experiment are shown in Table I.

Table I

Major diameter	76.5 cm
Minor diameter	11.0 cm
Rate of rise of plasma current	$\sim 3 \times 10^{12}$ A/sec
Peak plasma current	~ 300 kA
Maximum voltage for quadrant	~ 80 kV
Primary energy source	~ 0.5 MJ at 20 kV
Longitudinal bias B_z field	≤ 6 kG

The experiment should be assembled in the spring of 1971.

Reference

1. LA-4352.

MHD CALCULATIONS OF THE LINEAR SHOCK HEATED Z-PINCH (P-14)

(Albert Haberstich)

Numerical z-pinch calculations, using a one-dimensional MHD code, are performed in an attempt to duplicate the magnetic field and density profiles as well as the z current and voltage observed on the linear shock heated z-pinch experiment.[1] The purpose of these calculations is to gain better understanding of the processes taking place in this type of discharge and to determine parameters such as the diffusion rate and the ion temperature.

Experimentally, the B_θ magnetic field is found to diffuse into the discharge at a rate higher than classical. This effect, which in the MHD model is related to an anomalously high electrical resistivity, has also been observed in low density theta pinches.[2] After 1 μsec, the shape of the magnetic field profiles changes much less rapidly.

Following Bodin et al.,[2] we assume that the enhanced diffusion is caused by a micro-instability which is triggered when the electron drift velocity exceeds an acoustic velocity $((T_e + T_i)/m_i)^{\frac{1}{2}}$, T_e and T_i being the electron and ion temperatures and m_i being the ion mass. For the anomalous resistivity μ we take a multiple of the Bohm value, $B/(16\, n_e\, e)$, where B and n_e are the local magnetic field and electron density and e is the charge of the electron. Whether this is a good choice is difficult to establish with the presently available data.

Since the achievable ion temperature depends to a large extent on the rise time of the z current, we drive the computed z-pinch with an electrical circuit equivalent to the magnetic energy storage system used in the experiment.[3] The fuse is replaced by a variable resistance which, beginning at the time when the current in the storage inductance goes through its first maximum, rises at a rate of 0.25 Ω/μsec. The transfer switch closes at 25 kV.

The linear pinch is initially biased with a B_z field of the order of 3 kG. A cylindrical conductor conserves the B_z flux during the discharge. The problem thus involves anomalous

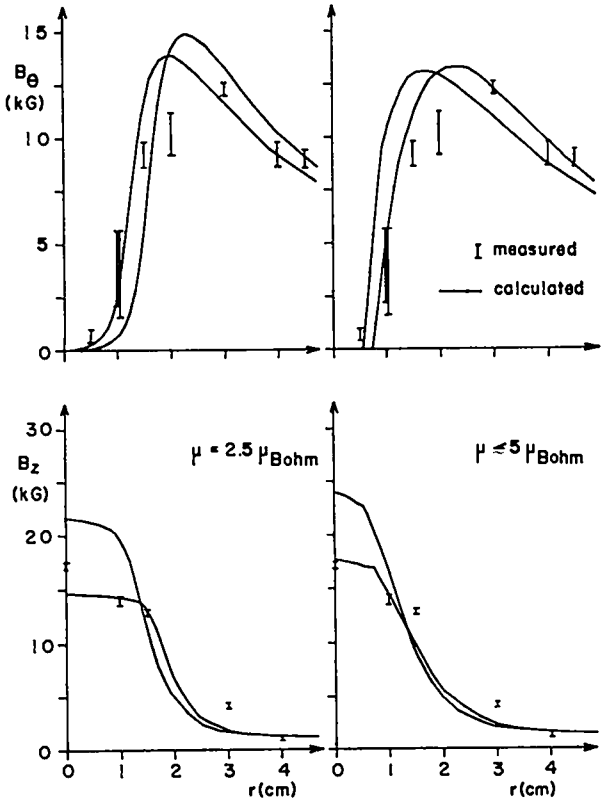

Fig. 30. B_θ and B_z profiles.

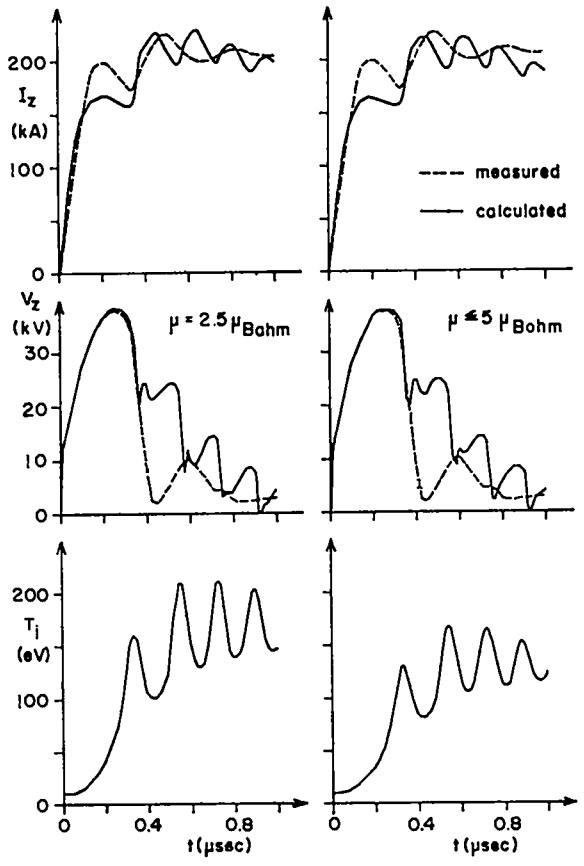

Fig. 31. Time, voltage, and I_z profiles

resistivities both parallel and transverse to the magnetic field. Some paramagnetic effect is allowed to obtain the low B_z field observed in the outer region of the pinch. This is done by choosing $\mu_{//} \approx \mu_\perp / c_1$ where c_1 is a constant of order 10.

B_θ and B_z profiles obtained at 1 μsec into the discharge cycle with a deuterium filling pressure of 30 μHg are shown in Fig. 30(a). The Bohm factor is 2.5 and the resistivity is anomalous everywhere at all times. The plasma is still experiencing some bouncing motion at this time as indicated by the calculated solid curves. The error bars correspond to the measurement.

The profiles in Fig. 30(b) were obtained with a local anomalous resistivity of 5 times the Bohm value, using the above threshold condition. The toe of the B_θ distribution occurs at the transition between classical and anomalous resistivity at this point. Whether the finite structure of the numerical scheme has a retarding effect on the penetration of B_θ is still under investigation.

Figures 31(a) and (b) show time dependences of the calculated and measured z current and voltages as well as the calculated average ion temperature for the two cases. The magnitude and bouncing frequency of the calculated current are in good agreement with the measurement. The lack of structure of the measured z voltage may be an electrode effect. Voltage traces obtained with a longer discharge tube are in better agreement with the calculation. The average ion temperatures are of the order of 150 eV. This value is 35% lower than calculated with an idealized z current rising to 200 kA in 0.1 μsec.

References

1. J. N. DiMarco and L. C. Burkhardt, Annual Meeting of the A.P.S. Division of Plasma Physics, Washington, D.C., Nov. 4-7, 1970.

2. H.A.B. Bodin, J.McCartan, G.H. Wolf, Third European Conference on Controlled Fusion and Plasma Physics, Utrecht, June 23-27, 1969. H.A. Bodin and A.A. Newton, Phys. Fluids 12, 2175 (1969).

3. J. N. DiMarco and L.C, Burkhardt, J. Appl. Phys. 41, 3894 (1970).

ALL METAL WALL DISCHARGE TUBE (P-14)

(J.A. Phillips)

We are again looking at metal discharge tubes as replacements for conventional ceramic tubes, e.g., quartz or alumina. The advantages to be gained with metals over ceramic may be summarized as follows:

1. A conductor can absorb higher energy pulses on the surface exposed to the plasma without melting because of its higher thermal conductivity.

2. A careful choice of wall material can lessen plasma contamination from material released by evaporation and ion bombardment. Losses by bremsstrahlung radiation, $\sim Z^2$, can be reduced if low-Z metals can be considered.

3. Fabrication of a discharge tube that fits closely inside a return conductor or primary can be easier if the tube is machined out of metal. In our proposed toroidal experiment, it is difficult to procure ceramic or quartz torus sections that do not add prohibitive inductance.

A figure of merit ($Qt^{\frac{1}{2}}$) has been determined for evaluating various materials. It has been calculated[1] that the temperature rise (ΔT) of a surface for a flux of Q of energy is given by

$$\Delta T = 2Q(t/\pi\ Ck\rho)^{\frac{1}{2}}$$

where t = time, C = thermal conductivity, k = thermal capacity and ρ = specific heat. With ΔT determined by the melting point, it is clear[2] that metals are superior to insulators. With metals, the question arises how to reconcile the conflict between the high electrical conductivity of the wall and the necessity for the axial electric field in a z-pinch. For slow toroidal experiments such as Zeta and Tokamak it is practicable to use corrugated thin walls to keep the wall currents to tolerable proportions. For the planned fast toroidal z-pinch experiment with high field gradients ($E_z \approx 1$ kV/cm), the wall currents would be too large for a practical tube. There are two other ways by which wall currents can be reduced other than high resistance, i.e., by subdivision of the wall, and by high inductance. We report here on results on subdividing the walls.

When a conducting discharge tube wall is subdivided, the voltage between adjacent conducting surfaces must be less than the running voltage of an arc, because a cathode spot might form on the negative side, and an arc would short-circuit the gap. Experiments[3] have shown that this voltage is about 25 V. If the discharge is to hold off ~ 1000 V/cm then the tube must have ~ 40 subdivisions/cm with insulation between adjacent metal surfaces. Subdividing the metal wall will also reduce unipolar areas,[3] i.e., reduce the area of each metal surface so that the current is below that required to maintain an arc spot.

An experiment was conducted using a series of stacked aluminum rings (washers). Aluminum was chosen as the material not because it has the most desirable thermal properties but the surfaces can be anodized. A total of 800 rings have a discharge tube length of ~ 24 cm. The rings were made of 0.010-in. aluminum and were anodized on each flat surface. Tests showed that 300 V could be applied between adjacent washers without breakdown. The construction is shown in Fig. 32a. The outer coaxial current return has also introduced a difficulty with this design, Fig. 32b. The capacity of each washer to ground, although much smaller than the inter-washer capacity, leads to a non-uniform division of the applied high voltage down the washer train. That difficulty can be avoided by surrounding the system with a relatively high resistance. In the present test experiment we chose a low resistance epoxy (Eccobond 60-L) with 150 Ω total resistance. An outer layer of glass cloth impregnated with epoxy gives strength to the assembly. The completed tube is shown in Fig. 33.

In some cases a small bias B_z field was initially applied to the all-metal tube in an attempt to minimize $m = 0$ instabilities and protect the tube against damage. When experience showed that the tube was not as fragile as we feared, runs were made without the bias field. A copper flux conserver wrapped around the discharge tubes smoothed out the azimuthal asymmetry of four return conductors.

The results of the tests of the all-metal tube have been compared with those of a

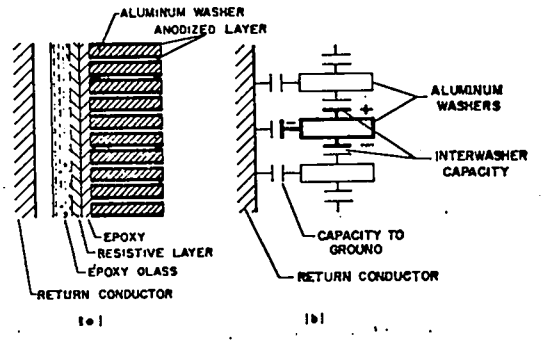

Fig. 32. Construction and schematic of stacked washer discharge tube.

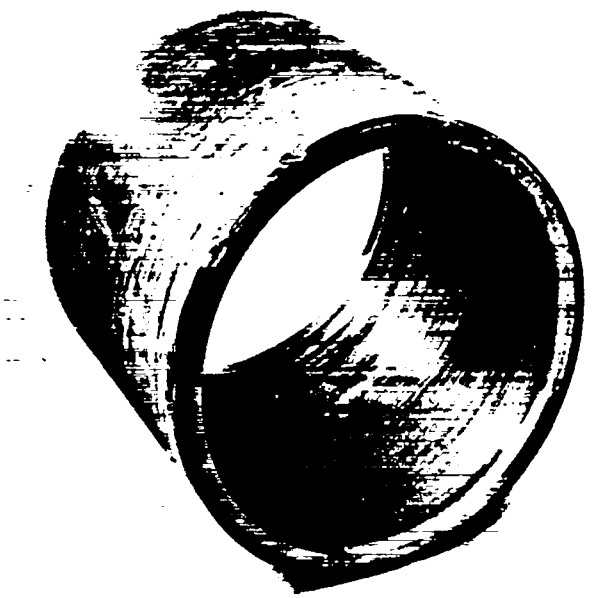

Fig. 33. Completed stacked washer discharge tube.

high purity alumina tube. The inside radii of the two tubes were the same (11.9 cm) but the all-metal tube was shorter (24.1 cm) than the ceramic tube (30.5 cm).

Several hundred discharges were made in the all-metal tube with voltages up to 30 kV. The period of the discharge current was ~ 15 μsec with peak currents up to 0.45 MA. The behavior of the discharge was determined by measuring (a) the voltage across the electrodes, (b) the discharge current, and (c) the B_θ magnetic field distributions in the region 5 cm in front of the tube surface.

Our first concern was the initial formation of the current sheath: was it symmetrical, and

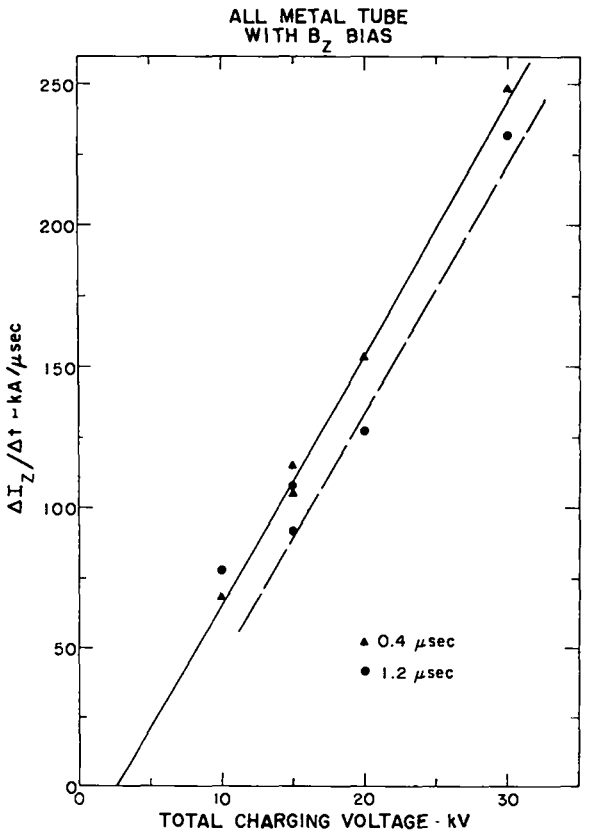

Fig. 34. Rate of charge of z-pinch current as a function of charging voltage.

did it pull off the wall? The time rate of change of the z-pinch current as a function of the charging voltage is shown in Fig. 34. If an arc developed along the tube wall or an asymmetric pinch formed as the voltage was raised, the discharge inductance would increase and the $\dot{I}$ fall. We see that, up to the maximum voltage of 30 kV, $\dot{I}$ remains proportional to voltage at 0.4 μsec in the discharge cycle. At 1.2 μsec the $\dot{I}$ is somewhat smaller indicating the increased inductance due to discharge pinching. No large irregular behavior occurs when the voltage is raised.

The voltage hold-off properties of the tube were examined by running a discharge at low pressures where the applied voltage would hold up for ~ 1 μsec before the discharge current was initiated. When gas current did flow, the discharge behaved normally. This mode of operation was a severe test of the tube, but there was no wall breakdown even when electric field of ~ 0.83 kV/cm was applied. Indeed, when operating at the maximum voltage of 30 kV, where $E_z \approx 1.24$ kV/cm,

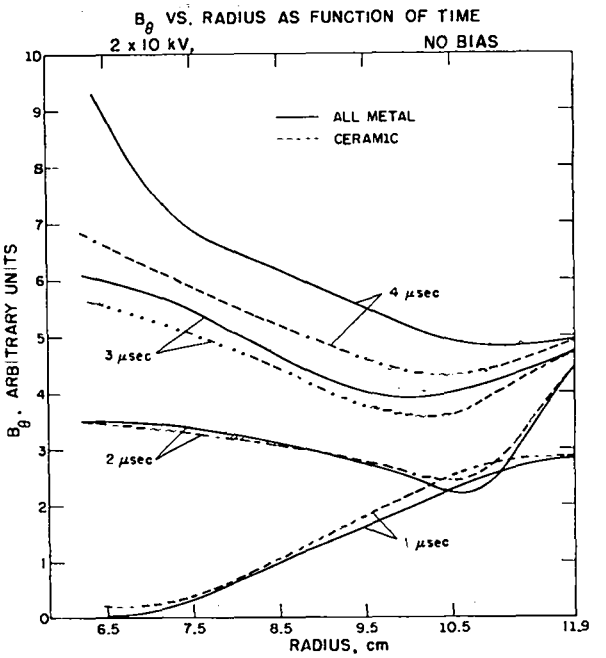

Fig. 35. B_θ field distribution.

we neglected a few times to add the filling gas to the tube with the result that after an initial voltage hangup the discharge tube behaved as a vacuum spark gap! These tests showed that the resistor divider along the tube behaved as expected and no damage to the tube resulted when fast or long high voltage pulses were applied.

To determine the nature of the current sheath, B_θ probe runs were made in the interval 5.2 cm in front of the tube wall for both the all-metal and ceramic tubes. Figure 35 shows plots of the B_θ field distributions at selected times. The results for the two tubes have been normalized to the same magnetic field at the wall. (The discharge current in the ceramic tube was ~ 10% smaller than in the all-metal tube due to its greater length). Note that in both cases the plasma current pulls off the walls, with perhaps a larger percentage of the current flowing at smaller radii in the all-metal tube than in the ceramic tube. These data show that the plasma current does pull off the wall and contracts towards the axis.

Examination of the all-metal tube after several hundred discharges showed no severe

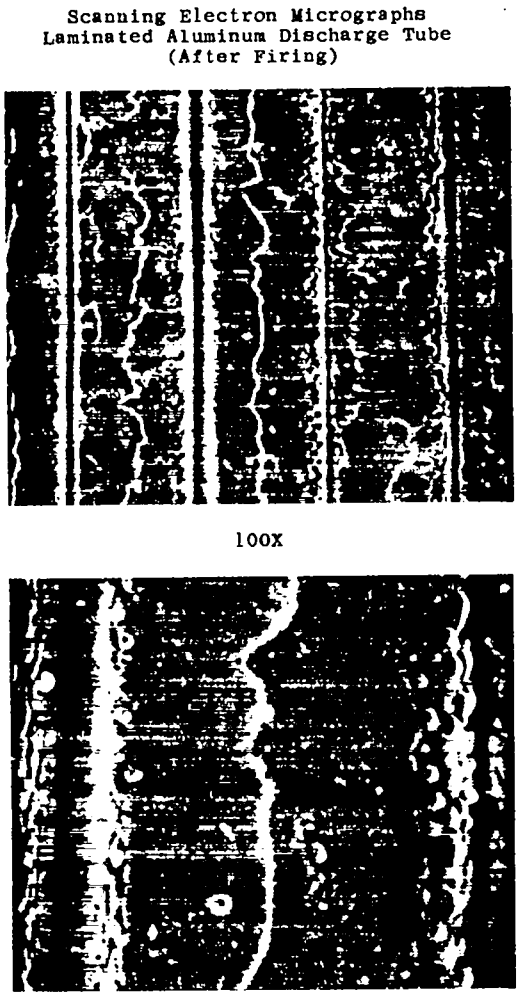

Fig. 36. Scanning electron micrograph of laminated aluminum discharge tube (after firing).

arcing. With the alumina discharge tube a fine brownish-white powder covered the lower electrode when the discharge tube was removed. This powder has been identified as α-plane Al_2O_3. Small chips apparently were plucked out of the surface during the discharge. No such debris was observed with the all-metal tube and the electrodes merely discolored as is usual in these discharges.

Scanning electron micrographs, Fig. 36, taken by T. Gregory (Group GMX-1), of the inside surface of the all-metal tube show some melting along the sharp edges of the washers. No heavy arcing between adjacent washers was seen.

With these encouraging results, we have designed an all-metal discharge tube for the fast linear z-pinch experiment.

References

1. A. A. Ware, TID-7536, Part 2, p. 293.

2. J. A. Phillips and J. L. Tuck, Proc. of the Geneva Conference, p. 40, Vol. 32 (1958).

3. J. L. Cranston, et al., Proc. of the Geneva Conference, p. 414, Vol. 32 (1958).

HIGH FREQUENCY DYNAMIC STABILIZATION OF THE Z-PINCH MHD INSTABILITIES (P-14)

(P.R. Forman, H.J. Karr, J.A. Phillips, A.Schofield)

Our investigation of methods of high frequency dynamic stabilization of the z-pinch MHD instabilities were concluded this year. The method reported here makes use of a high frequency oscillating B_z field. To accomplish this, a single-turn B_z coil 28 cm long was added to the Columba z-pinch experiment. This coil was energized by a .69 μF capacitor bank charged to 25 kV. This circuit produced a damped 750 kHz field with a maximum field of 2700 G. The rest of the system was described earlier.[1]

THEORY OF DYNAMIC $\tilde{B}_z$ STABILIZATION. The theoretical modified growth rate of the Kruskal-Shafranov helical instabilities is determined assuming for the plasma a sharp boundary model that obeys the ideal MHD equation. Cylindrical geometry is assumed and only divergenceless displacements are considered. If one linearizes the ideal magnetohydrodynamic equations and assumes that all perturbed quantities vary as

$$\xi(r,\theta,z,t) = \xi(r)\exp(\gamma t + i(m\theta + kz)) \tag{1}$$

one obtains an equation for the helical radial displacement (ξ) of the plasma surface

$$\frac{d}{dr}\left(\frac{r}{k^2r^2+m^2}\frac{d}{dr}(r\xi_r)\right) - \xi_r = 0. \tag{2}$$

The solution of this equation, which is regular at the origin, is

$$\xi_r = C\, I'_m(kr). \tag{3}$$

In the vacuum region outside the plasma there are no currents flowing. Therefore, $\nabla \times \underline{B} = 0$ so $\underline{B}$ can be expressed as the gradient of a potential. Since $\nabla \cdot \underline{B} = 0$, the potential is a solution of Laplace's equation in cylindrical coordinates,

$$\underline{B} = \nabla \Phi(r) \tag{4}$$

$$\Phi(r) = A\, I_m(kr) + B\, K_m(kr). \tag{5}$$

By requiring the magnetic field to be tangential to both an exterior conducting wall and to the helically perturbed plasma-vacuum interface and requiring the total pressure to be constant, one obtains appropriate values for the unknown constants A, B, and C of Eqns. (3) and (5).

The resulting growth rates for the Kruskal-Shafranov helical modes is

$$\gamma^2 = B_{ze}^2\left[(1-\beta)(ka)^2 + \mu^2\frac{ka\, I'_m(ka)}{I_m(ka)} + (ka+m\mu)^2\frac{I'_m(ka)}{I_m(ka)}M(b)\right] \tag{6}$$

where

$$\mu = \frac{2I_z}{a\,B_{ze}} \tag{7}$$

$$\beta = 1 - \left(\frac{B_{zi}}{B_{ze}}\right)^2 \tag{8}$$

a = plasma radius

b = radius of conducting wall

B_{ze} = axial magnetic field in the vacuum region

B_{zi} = axial magnetic field inside the plasma

$$M(b) = \frac{I_m(ka)K'_m(kb) - I'_m(kb)K_m(ka)}{I'_m(ka)K'_m(kb) - I'_m(kb)K'_m(ka)}.$$

Inclusion of the inertial term gives the equation of motion

$$\pi a^2\rho\frac{d^2\underline{\xi}}{dt^2} \pm \left\{\frac{B_{ze}^2}{4}(1-\beta)(ka)^2 + \frac{I_z^2(ka)}{a^2}\frac{I'_m(ka)}{I_m(ka)} \pm \left[\frac{B_{ze}^2}{4}(ka)^2 + \frac{m^2I_m^2}{a^2} + mkI_zB_{ze}\right]\frac{I'_m(ka)}{I_m(ka)}m(b)\right\}\underline{\xi} = 0 \tag{9}$$

where ρ is the mass density.

If the external field B_{ze} is allowed to have an oscillatory component $B_{ze} = B_o + B_1 \cos\omega t$, and the following definitions are made

$$Z = \frac{\omega t}{2} \qquad \epsilon = \frac{4}{\omega^2 \pi \alpha^2 \rho} \qquad E = \frac{I'_m(ka)}{I_m(ka)} \tag{10}$$

$$\Gamma = (1 - \beta + E\,M(b))$$

$$\alpha = \epsilon \left[\left(B_o^2 + \frac{B_1^2}{2} \right) \left(\frac{ka}{2} \right)^2 \Gamma + \left(\frac{I_z}{a} \right)^2 (ka + m^2 M(b))\, E + k I_z \mu\, B_o M(b)\, E \right]$$

$$q_1 = \frac{\epsilon}{z} \left[\frac{B_o B_1}{2} (ka)^2 \Gamma + m\, k\, I_z\, B_1\, M(b)\, E \right]$$

$$q_2 = -\epsilon \left(\frac{ka\, B_1}{4} \right)^2 \Gamma ;$$

the equation of motion is the Hill equation .

$$\frac{d^2\xi}{d^2Z^2} + \left[\alpha - 2q_1 \cos 2Z - 4\, q_2 \cos 4Z \right] \xi = 0 \tag{11}$$

The growth rates are obtained from the complex part of the exponential term of the Floquet solution of the Hill equation.

For the experimental parameters used in the Columba experiment, only parametric modes are predicted and the theory indicates that the growth should be reduced to rates too small to be observed in the time duration of the experiment.

EXPERIMENTAL RESULTS. Initial experiments on oscillating B_z dynamic stabilization were frustrated by the appearance of azimuthal j_θ currents which excluded the oscillating B_z flux from region near the plasma column. It was speculated that wall breakdown was the problem. Pyrex, quartz, and ceramic discharge tubes were used in an attempt to minimize the effect. A quartz tube, after about 100 discharges, seemed the best, but the effect was still overwhelming and did not improve with successive discharges. These induced j_θ currents were observed with a B_z probe inserted radially into the discharge chamber. In addition, B_z probes showed a lack of an oscillatory component beyond the first half-cycle; external Φ_z flux loops showed that the B_z was being excluded after one-half cycle; and Mach-Zehnder interferograms showed a significant increase in electron density near the wall. A one-dimensional MHD code was employed to investigate the expected behavior of the plasma. The calculations revealed good penetration of the oscillating B_z in agreement with experiment for the first half-cycle of stabilization and in disagreement with the observed shielding of the subsequent oscillations of the stabilizing field. These results reinforced the suspicion that a wall effect was involved.

Haberstich pointed out that since the E_θ field is a maximum at the discharge wall, and if j_θ currents could be prevented from flowing in the outer regions, then, perhaps, close to the pinch the electric field would be low enough so that secondary currents would be reduced and the oscillating B_z field would then be able to penetrate closer toward the pinch column. The j_θ currents may be inhibited by a limiter, as used in Stellarators and Tokamaks, to confine the z-currents to the central region of the discharge tube. In our geometry, such a limiter would consist of longitudinal fins that are parallel to the tube axis, and extend the full length of the discharge. Objections can immediately be raised to such limiters, the most serious of which is that the close proximity of the leading edge of the fin to the discharge will lead to heavy plasma bombardment and the release of impurities. However, the area of the fins is small and contaminations may not be serious. Such an experiment would show whether magnetic fields could be made to penetrate further into a discharge region, and a more meaningful test of the theory could be made.

Consequently the glass shop fabricated a Pyrex tube (i.d. ~ 6.5 cm) in which two diametrically opposite longitudinal fins were formed with a distance of 3.90 cm between the inner edges of the fins. This distance was chosen so that there would be a distance of ~ 1 cm between the edge of the fin and the plasma column of diameter ~ 2 cm.

Two runs were made with the z-pinch, one with the tube having the longitudinal limiters and the second with a standard cylindrical quartz tube

Diagnostics included the measurement of z-pinch current and voltage, and Φ_z flux inside a one-turn coil wound on the outside of the tube, B_θ and B_z with magnetic probes, and the stabilization current in the θ-pinch coil; Mach-Zehnder interferograms were taken axially down the tube. Runs were made with and without a small (~ 206 G) B_z bias field.

The measurement of the Φ_z flux immediately showed a marked difference between the two discharge tubes (Fig. 37). Before the stabilization field was applied (at ~ 1.6μsec) the normal increase in Φ_z flux was seen due to pinch compression and paramagnetism. In the first half-cycle of the oscillating B_z field, the flux was seen to behave the same in the two discharge tubes; the flux penetrated into the tubes unimpeded. However, on the second half cycle there were marked differences. With the uniform quartz tube the flux did not reverse and was shielded out by a conducting layer close to the inside wall. With the longitudinal limiters the flux oscillated about the starting value. There was a relatively free flow of B_z flux in and out of the discharge tube. The dashed lines on the figure represent typical values that the flux would have if no stabilization field were present.

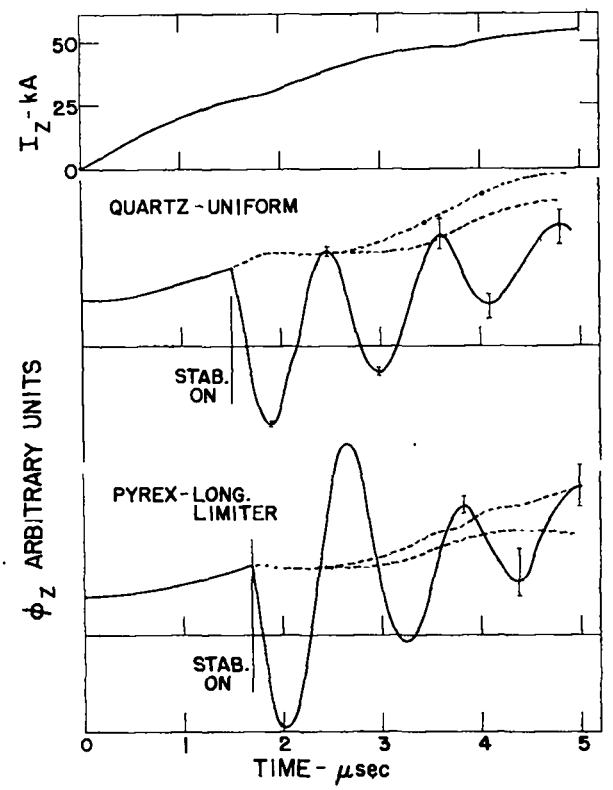

Fig. 37. Φ_z flux.

Flux loop and probe measurements confirmed that the limiters were indeed inhibiting the j_θ currents and the oscillating B_z extended in as far as the fins.

Allowing the B_z field to penetrate close to the pinch column by the limiters delayed the onset of the kink instability. The signals from flux loops indicated that the average time of onset was delayed by 75%, from 3.1 μsec without stabilization field to 5.4 μsec with stabilization. At these late times in the discharge cycle, (a) the peak B_z had decayed to about 30% of the first half cycle by the damped LC driving circuit, (b) loss of plasma out the ends decreased the line mass of the pinch column, and (c) the I_z current had increased to about 40 kA.

All these factors result in less effective stabilization by the B_z. The increase in stable time, as shown in this experiment, may not be the maximum that can be obtained by this method. An extension of the experimental parameters would be necessary to demonstrate the limits.

Reference

1. LA-4351-MS.

TOROIDAL Z-PINCH EQUILIBRIA (P-18)

(D. A. Baker and L. W. Mann (T-5))

INTRODUCTION. The techniques for calculating ideal MHD equilibria numerically for toroidal multipoles, as discussed in the last annual Status Report[1] have been very useful aids in the LASL quadrupole program. In particular, the flux calculations, when used in conjunction with laser interferometer measurements and magnetic probe data taken outside the hot plasma, allow a deduction of the injected plasma temperature as a function of time. Further details are given in the quadrupole section of this report.

We have been successful in extending the numerical techniques to handle general axisymmetric MHD equilibria with perfectly conducting boundaries. Interest, of late, is in calculation of possible equilibria for the LASL toroidal z-pinch presently under construction.

EQUILIBRIUM CALCULATION. We desire solutions of the system of equilibrium equations

$$\nabla p = \vec{J} \times \vec{B} \tag{1}$$

$$\nabla \times \vec{B} = \mu \vec{J} \tag{2}$$

$$\nabla \cdot \vec{B} = 0 \tag{3}$$

for a cylindrically symmetric system having perfectly conducting boundaries and both poloidal and toroidal magnetic fields.

We introduce a cylindrical right-handed coordinate system (r, φ, z) with corresponding unit vectors $(\hat{r}, \hat{\varphi}, \hat{z})$ and a poloidal flux function ψ so that the poloidal magnetic field is given by

$$\vec{B}_p = \frac{1}{r} \nabla \psi \times \hat{\varphi}. \tag{4}$$

From Eq. (1) we see that $\vec{\nabla} p \cdot \vec{B}$ and $\vec{\nabla} p \cdot \vec{J}$ are zero so that $\vec{B}$ and $\vec{J}$ are everywhere tangent to the constant pressure surfaces. It follows that the pressure and poloidal current inside a radius r are functions of ψ only. We therefore let

$$p = p(\psi) \tag{5}$$

$$\bar{I} = \bar{I}(\psi) \tag{6}$$

with the toroidal field B_φ given by

$$B_\varphi = \mu_o \bar{I}/r. \tag{7}$$

We have defined ψ and $\bar{I}$ such that $2\pi\psi$ and $2\pi\bar{I}$, evaluated at any radius r, are the poloidal magnetic and current fluxes threading an r = constant and z = constant contour. With these definitions Eqs. (1), (2), and (3) can be reduced to the following single equation for ψ:

$$r \frac{\partial}{\partial r} \left(\frac{1}{r} \frac{\partial \psi}{\partial r} \right) + \frac{\partial^2 \psi}{\partial z^2} = -\mu_o J_\varphi, \tag{8}$$

where the toroidal current density J_φ can be written in terms of the p and $\bar{I}$ functions

$$J_\varphi = r^2 p' + \mu_o \bar{I} \bar{I}'. \tag{9}$$

Primes denote differentiation with respect to ψ. Once the functions $p(\psi)$ and $\bar{I}(\psi)$ are chosen, we solve Eq. (8) numerically on a finite difference mesh, subject to the condition that ψ is constant on all conducting boundaries. Once $\psi(r, z)$ is known, all quantities of interest can be computed.

RESULTS

General. The general change in the properties of a linear cylindrical pinch when it is bent into a torus are shown in the pressure and flux plots of Fig. 38. These were obtained from a computation for a case with a single peaked pressure profile and an aspect ratio (major radius/minor radius) very nearly unity. The normally circular flux surfaces become elongated in shape and are displaced to larger radii as the plasma compresses flux against the outer wall, thus compensating the radial expansive forces associated with the loop of pinch current. As a check, our computed outward shift has been compared with the expansion formula of Shafranov and found to agree for large aspect ratios.

Hollow Pressure Profile. The experimental results of Burkhardt and DiMarco on a fast linear z-pinch show an enhanced containment and temperature over earlier z-pinches. Their measurements indicate that the pinch has a hollow pressure distribution, i.e., the pressure peaks at a finite

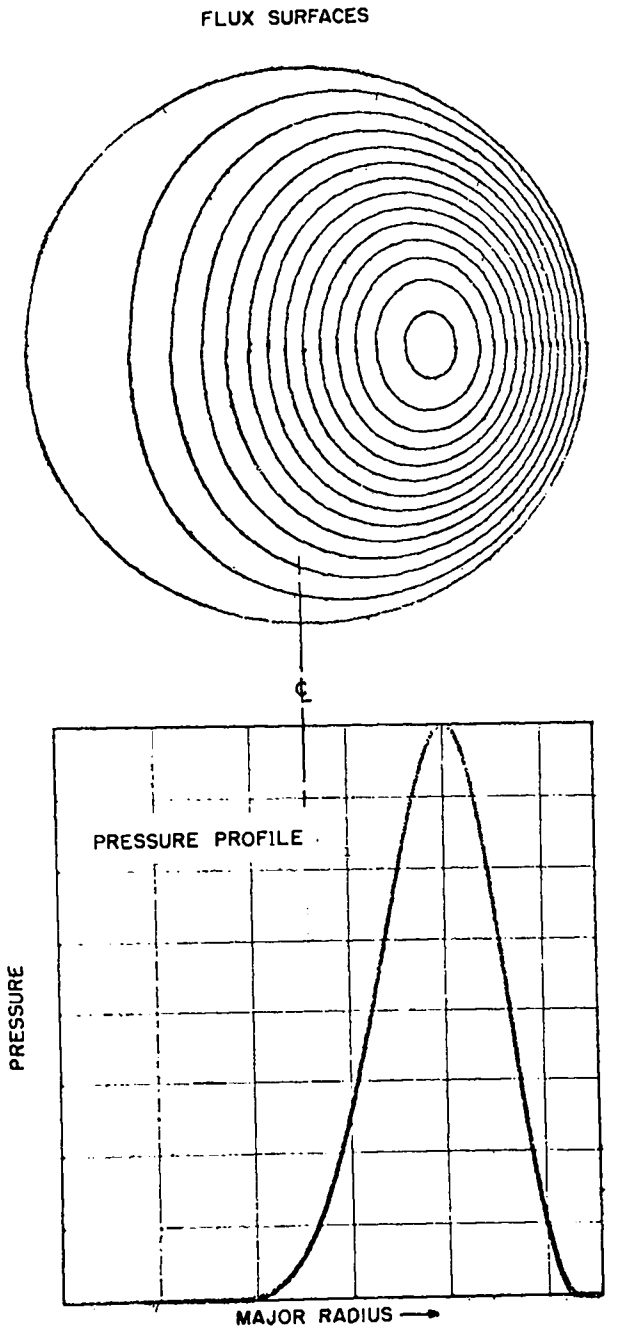

Fig. 38. Cross-sections of flux surfaces and pressure profile for a torus with an aspect ratio (major radius/minor radius) of 1.009 demonstrating toroidal distortions.

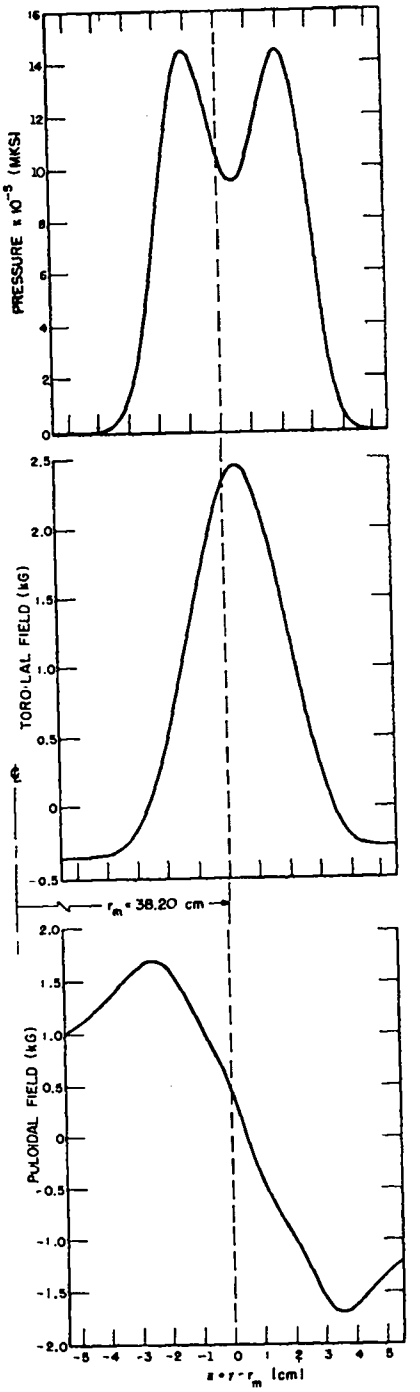

Fig. 39. Profiles of magnetic field and pressure for a toroidal equilibrium representing hollow 300-kA z-pinch having trapped and compressed toroidal field. The origin of the radial variable x is located at the minor axis of the conducting toroidal wall.

radius of the symmetry axis. Freidberg investigated stability properties of a class of linear z-pinches with hollow profiles and reversed field outside and found them to be favorable for obtaining MHD stability. We have computed such equilibria for the toroidal case to examine their properties. The resulting pressure and field distributions for a hollow 300-kA pinch having a small reversed

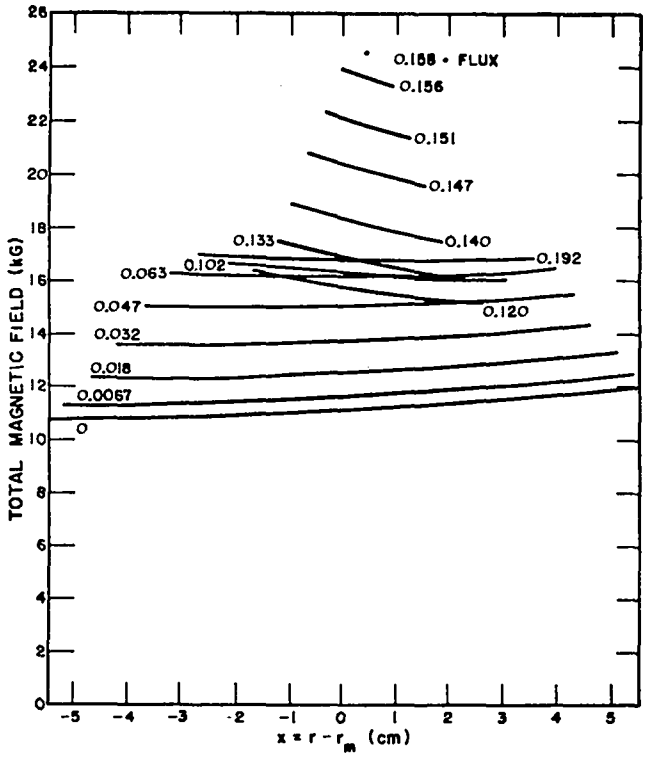

Fig. 40. Plots of the field magnitude along field lines for a hollow z-pinch toroidal equilibrium as a function of major radius. The minor axis is at x = 0. The poloidal flux values (Webers) give the flux between each given flux surface and the wall.

field outside the pinch are shown in Fig. 39. The geometry is that of the LASL toroidal z-pinch under construction, namely with a major radius of 38.2 cm and a minor radius of 5.5 cm. Some interesting properties of this equilibrium can be seen by inspecting Fig. 40. Here we show the total magnitude of the magnetic field on flux surfaces as a function of radius from the symmetry axis. The values of flux are indicated starting with zero at outer conducting boundary. These plots start at their maximum length, corresponding to the outer wall, and become shorter, corresponding to flux surfaces approaching the magnetic axis. In Tokamaks, the toroidal 1/r field dominates and the strongest fields, which are at smaller radii, will mirror particles toward the region of unfavorable toroidal curvature (large radii). This is true in this trapped field z-pinch equilibrium also for the region well inside the pinch where the poloidal field is small. But, as can be seen from Fig. 40,

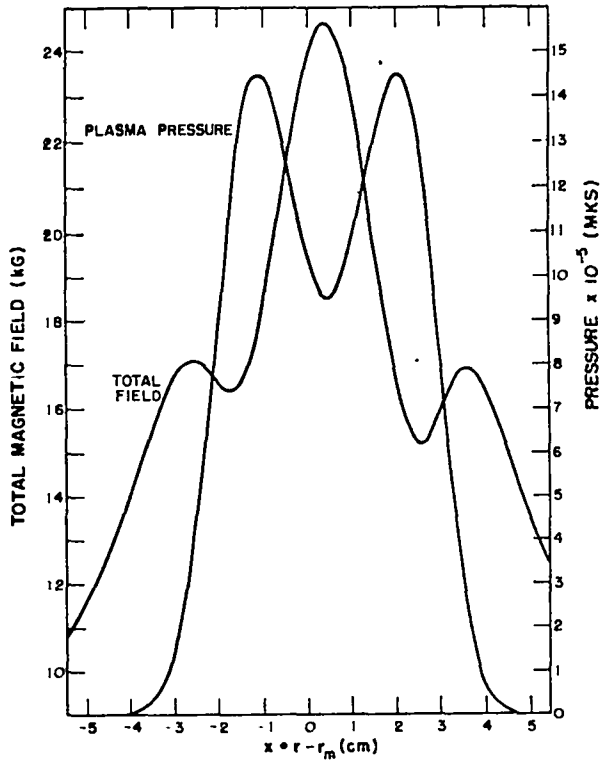

Fig. 41. Radial distribution of total field and pressure along the symmetry plane z = 0 for the hollow toroidal z-pinch equilibrium.

at outer flux surfaces, where the poloidal field dominates, the field becomes maximum at the outer-most radii. This means that particles should be mirrored toward the good toroidal curvature regions. The maximum mirror ratio is 1.1 both inside and outside the pinch. The corresponding maximum mirror ratio for a Tokamak with this aspect ratio is 1.3.

It is evident from Fig. 40 that there is a magnetic well in the sense that there exists a toroidal flux surface whose B values are lower than those in regions on each side of it. The location of the plasma pressure relative to this well is shown in Fig. 41. Detailed stability analyses are under study.

Reference

1. LA-4351-MS.

SHOCK-HEATED TOROIDAL Z-PINCH EXPERIMENT (P-16)

(R. S. Dike)

The shock-heated toroidal z-pinch experiment, proposed by P-14 in the 1969 Annual Report, was approved for construction. The design features are shown in Fig. 29. The toroidal pinch in the center of the machine is driven by a toroidal primary that is split into four quadrants. Each quadrant contains an iron core to improve the coupling between the primary and the plasma secondary. The energy system is a 400-kJ, 20-kV capacitor bank that charges a magnetic storage inductor in the bottom of the assembly through a fuse. When the inductor is fully charged the fuse opens creating about 90 kV that is transferred to the four primary quadrants via the transfer switch. The fast rising current in the primary shock-heats the plasma and compresses and contains it for some time. The primary is also wrapped with a B_z winding.

All the hardware has been designed and ordered. Most of it has been delivered and installation has begun. The first experiments on this machine are scheduled to begin in the spring of 1971.

COMPUTER SIMULATION OF CLASSICAL RESISTIVITY (P-18)

(T. A. Oliphant)

The method reported in a recent paper[1] for including the effects of binary collisions in the computer simulation codes has been generalized to include the treatment of various species moving at nonzero relative average velocities. A sample calculation was set up consisting of a classical Lorentz gas moving under an applied E-field. The ions were assumed to be cold and infinitely heavy. For small applied fields, the electrons accelerated to an equilibrium velocity close to the classical Lorentz drift velocity in several electron-ion relaxation times. For values of E close to the critical value for electron runaway, a group of runaway electrons was observed. For higher values of E, more runaway electrons were observed.

Reference

1. T. A. Oliphant and C. W. Nielson, Phys. Fluids 13, 2103 (1970).

PLASMA GUN PROGRAM

BIRDSEED EXPERIMENT (P-17)

(I. Henins, J. Marshall)

The entire effort of two staff members and two technicians for approximately 8 months of the year went into the Birdseed experiment. The experiment involved the firing of a gun plasma from a rocket at high altitude, and observation of its interaction with the geomagnetic field and the partially ionized plasma of the ionosphere. General responsibility for the experiment was taken by LASL Group J-10. Other organizations contributing to the program included GMX-6, explosive gnerators and diagnostic support; P-17, plasma gun and diagnostic support; Sandia Laboratories, Albuquerque, rocket hardware, telemetry, and launch; EG&G, diagnostic support. A general report will be prepared after all data have been reduced. We give a brief account here of the experiment as it involved Group P-17. In addition, we shall discuss certain aspects of gun behavior as encountered in this work.

The Birdseed program is an extension of auroral work and high altitude barium release experiments carried out in the past at LASL. While this work is not directly concerned with controlled thermonuclear research, it involves phenomena which might well be. It also involves the extension of gun size and energy beyond that which can be funded in the present CTR program.

We wished to inject plasma into the region of interest with a velocity of the order of 10^7 cm/sec or greater in quantities large enough to allow observation from the ground. The plasma was to have a composition such that it could be distinguished spectroscopically from components of the atmosphere. To meet the requirements, it appeared that the best choice was neon plasma generated by a coaxial pulsed hydromagnetic plasma gun, powered by explosive generators. Explosive generators allowed the use of several hundred kilojoules of energy to operate the gun within the payload limits of a STRYPI rocket system.

The requirements of the experiment implied considerable changes in gun parameters from those used before, as well as a change in the gas used, and the use of the explosive generators instead of capacitor banks. It was decided to perform a series of ground tests in which explosive generators were used to drive a gun firing into a large vacuum tank in which various plasma diagnostics could be performed. Most of these tests and their diagnostics were described in the last annual report as was the gun performance achieved. During the period covered by this report two more large vacuum tank explosive generator shots were made. Diagnostics were much the same except for measurements of angular distribution of plasma energy which will be discussed below. In both of these shots, generator performance appears to have been inferior to the average of earlier shots, so no spectacular gun performance was achieved.

After the end of the ground test/vacuum tank series it was planned to shoot three complete rocket payload assemblies, to test the system under simulated flight geometries. These shots, or perhaps more accurately, these payloads, were named Birdseed Auk, Birdseed Buzzard, and Birdseed Crow. A modest sized (79-cm diam x 122-cm long) expendable vacuum tank was used for each shot so that gun plasma would be driven into vacuum and photographed through a side window to determine whether the gun had worked normally. Auk was a failure. Apparently a short circuit developed in the explosive switch designed to connect the primary capacitor bank into the generator circuit. Presumably it was caused by conducting explosive gases. A number of other shakedown problems were encountered, but all seem to have been corrected in the successful Buzzard shot. Diagnostics on these shots were rather crude because of limited facilities and space in the expendable vacuum tank and in the rocket nose cone itself. Enough diagnostics were brought out to give a reasonable chance of identifying malfunctions so that they could be corrected, but there was no chance to do quantitative measurements on the gun plasma. The Crow payload was intended to be shot after a number of mechanical tests involving centrifuging and vibration over a wide range of frequencies with the capacitor bank charged. During this there were serious malfunctions. A capacitor failed and a high-voltage lead pulled off the bank. The date on which the Duck and Egret payloads were to be shipped to the launch site on Kauai, Hawaii, was approaching, and it was decided that there was not time enough to rebuild Crow and fire it. The failures during mechanical testing were assumed to be due to conditions considerably more severe than they would probably be in flight, and it was decided to go ahead with the Duck and Egret launches without a second successful payload test shot. The capacitor failure during testing, in addition to some other unpleasant experiences, led to the decision not to charge the bank fully before launch as had been planned, but to finish charging during flight so as to minimize time at full voltage. This was done with a power supply which had the original purpose of simply maintaining full charge against leakage.

The telemetry system used on the Birdseed rocket flights did not have wide enough bandwidth to give measurements allowing more than qualitative evaluation of gun performance. While quite adequate for its normal function of monitoring more or less steady voltages, temperatures and attitude, it could not transmit data fast enough to provide current and voltage information from which energy input into the gun could be calculated. This was an undesirable situation since, with the observed variability of generator performance, we could not reliably predict the amount of plasma energy which would be produced by the gun. An attempt was made to use an on-board analogue computer to calculate total electrical energy delivered through the gun terminals and to telemeter this simpler information to the ground. The information which came back through this system on the Duck and Egret shots appear to have cut off before all energy had been delivered to the gun. Some component may well have been destroyed by blast. The result is that the energy of these shots is not known.

Duck and Egret appear to have performed satisfactorily. Both payloads were fired at altitudes of about 210 km, and produced plasma

effects which were visible from the ground. The two shots were oriented in different directions relative to the geomagnetic field with the plasma from Duck being injected about 65° away from the direction of the field and Egret about 35°. In both cases a streak of luminosity was observed to move north and south in the direction of the field with a speed of at least 10^8 cm/sec, 5 to 10 times that of the gun plasma. Luminosity was observed for more than 20 km in each direction. The fast moving luminosity was succeeded by a slower brighter luminosity moving north (downward) along the field at speeds comparable to gun plasma speeds, apparently stopping and then gradually diminishing in intensity for many tens of milliseconds. The bright light was, presumably, mostly produced by gun plasma at the injection point and was easily visible to the naked eye. The first luminosity required image intensification to be seen by a camera.

Calorimetry, Angular Distribution and Ablation Effects. Several of the large vacuum tank explosive generator gun shots included diagnosis by calorimetry and ballistic pendulum. In the last three, Birdseed XII, XIII, and XIV, the ballistic pendulum-calorimeter was subdidived to provide information about heat distribution inside the calorimeter can. XIII and XIV were elaborated by a double diaphragm toward the rear of the calorimeter. Plasma passing through the hole would strike the rear plate and either leave its energy there or spread it around the rear chamber as ablation products or reflected plasma. As can be seen in Table I, with reference to Figure 42, approximately 2/3 of the energy passing through the hole was finally collected on surfaces which could not possibly have been hit directly by the gun plasma. The center of the copper back plate, which was hit directly, shows signs of superficial melting with a rough center area about 7 cm in diameter surrounded by a polished area. The inside of the back can appears to be covered by a deposit, presumably of copper condensed from vapor. We assume that the rate at which energy was delivered to the central spot (about 5×10^6 W/cm^2 averaged over the area behind the 182 cm^2 hole in the diaphragm) was too high for

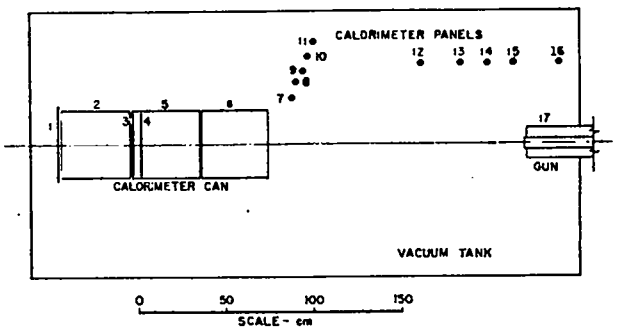

Fig. 42. Schematic representation of vacuum tank and calorimeter location relative to plasma gun.

Table I
Energy Measurements in Calorimeter Can
Average of Birdseed XIII and XIV

Location	Energy (kJ)	Solid Angle (sr)	Energy/ Solid Angle (J/sr)
1. Back plate	13.9		
2. Back can	22.3	39.7 .0039	1.02×10^7
3. Back of diaphragm	3.5		
4. Front of diaphragm	10.7	.020	5.35×10^5
5. Middle can	13.3	.010	1.33×10^6
6. Front can	19.7	.022	0.90×10^6

the copper to carry the heat away from the surface without melting and vaporization. The result is that at power levels such as this most of the plasma striking a surface is carried away by hot ablation products. We observe ablation effects to be more pronounced when plasma power fluxes are larger and when materials other than copper, such as aluminum alloy or glass, are struck. As can be seen from Table I, the energy collected per steradian by the front of the diaphragm is smaller than that collected by the middle calorimeter can. Presumably this too is partly due to ablation, since ablation scars are observable on the surface.
In Fig. 42 we show the locations of a number of calorimeter panels. Most of these were simple rectangles of sheet copper with thermocouple junctions attached. Two of them were in the form of copper cans, oriented so that the open end pointed toward the gun muzzle and was protected by

masks so that plasma from the general direction of the gun would not strike the outside. The two cans gave energy flux measurements approximately twice as high as the open panels. If we assume that the open panel values should be multiplied by two, we obtain a reasonably smooth distribution of energy fluxes which falls off to low values at large angles but which integrates to approximately 150 kJ for Birdseed XIII. Thermocouple measurements of gun barrel temperature allow us to estimate energy lost there. For Birdseed XIII it was 36 kJ. When we include the 79 kJ of energy collected in the calorimeter can for this shot we get a total of 265 kJ which agrees well with the electrical energy delivered to the gun terminals. Presumably, a large fraction, perhaps half, of the energy collected by the calorimeter panels is radiation.

QUADRUPOLE

QUADRUPOLE INJECTION EXPERIMENT (P-17)

(J. E. Hammel, A. R. Sherwood, R. W. Kewish (P-16), J. Marshall, I. Henins)

INTRODUCTION. This experiment is the latest phase of a continuing LASL program directed toward the study of the physical processes that occur when the plasma stream from a coaxial gun enters, and moves through, a transverse magnetic field. In addition to the continuation of this study, objectives of the experiment are to achieve trapping of an energetic gun plasma in a confinement geometry, to study the mechanism of this trapping, and to measure its efficiency. Since levitation of the coils is inconsistent with the level of effort on the experiment, the coils are supported by dipole-guarded current feeds. A further objective is to determine the size of the leak introduced into the containment volume by this scheme of dipole-guarding the supports.

The assembly of the apparatus has been completed, and an experimental program aimed towards these objectives is now under way. So far, operation has been at half the design containment field. Electrostatic probe measurements have been made of the polarization electric field of the plasma stream in the injection region. In the same region, Rogowski loop measurements have also been made of the depolarizing current believed to be responsible for the trapping of the plasma. The results of these measurements are consistent with previous results obtained in other experiments.

A theoretical model of the containment leak caused by a dipole-guarded support has been investigated for comparison with the similar analysis of Meade. The size of the leak appears to depend sensitively on limits of integration in such a way as to suggest that valid results may require calculations of the precise three-dimensional system rather than an idealized two-dimensional system as done so far. This in turn casts doubt upon the validity of any such simple model and emphasizes the necessity of good experimental results. The first measurements obtained are of the electric field in the dipole region, and indicate outward plasma drift velocities considerably smaller than those predicted by the model. It has been observed, however, that an unguarded, protruding portion of the coil associated with the dipole feeds is being bombarded by the energetic plasma. New coils are being produced on which this protrusion has been suppressed.

A CO_2 laser interferometer ($\lambda = 10.6\ \mu$) has been developed and used to make density measurements of the plasma in the containment region. In addition, diamagnetic measurements have been obtained with a magnetic flux pickup loop. When combined, these measurements yield an average plasma temperature. Although the plasma energy containment time is of the order of 100 μsec, the temperature decreases much more rapidly. This is probably due to insufficient containment magnetic field strength for the several kilovolt ion energies observed at early times. The rate of temperature decrease and the energy containment time are found to be greatly affected by change in the gun parameters and configuration.

With these diagnostics, two important results have already been obtained, even with the field at half design strength. These are the very high efficiency of the trapping of the fast gun plasma in the quadrupole null and the previously mentioned electric field measurements in the dipole region.

MEASUREMENTS IN THE INJECTION REGION

The polarization electric field of the injected plasma stream has been measured by a set of three double probes located in the bridge of the outer coil as is shown in Fig. 43. The probes are in a line perpendicular to B (out of the plane of the Fig. 43), and they measure the electric field in the plasma stream according to where the B lines that intersect the probes connect to the plasma. A typical electrical field signal is shown in Fig. 44 for the case where the maximum magnetic field encountered by the injected stream is 3.5 kG. The electric field pulse lasts ~ 5 μsec and has a peak value of 400 V/cm. Although there is some uncertainty in the measurement

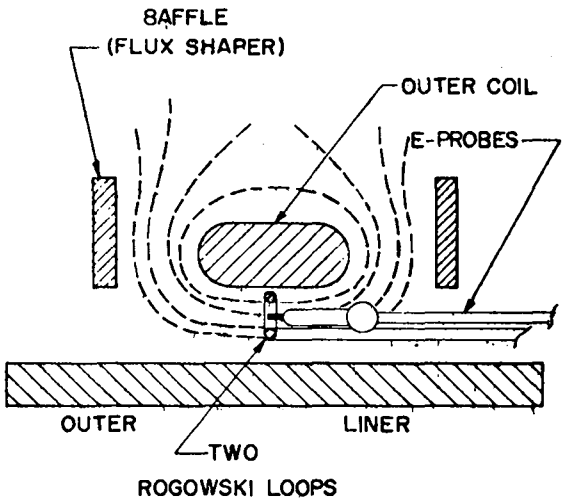

Fig. 43. Diagram showing the placement of the double probes and the Rogowski loops for making measurements in the injection region. Both the double probes and Rogowski loops are positioned to intercept B-lines which are centered on the injected plasma stream. The two probes are not in position simultaneously.

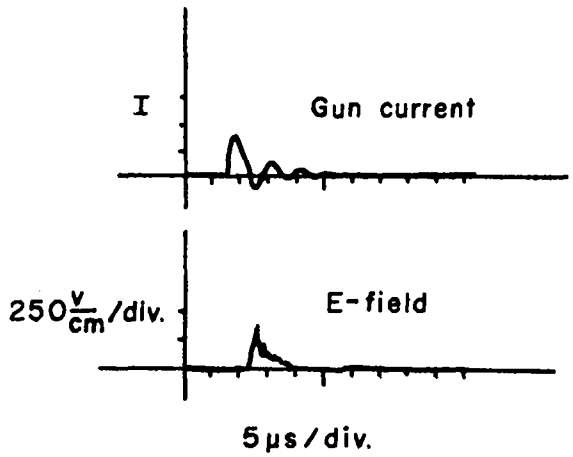

Fig. 44. The measured electric field in the injection region shown as a function of time.

involving lack of knowledge of the exact flux surface on which the probes lie, the peak value obtained for E/B in the plasma stream is 40 cm/μsec which is at the lower end of the range of velocities expected from the gun.

After the plasma stream crosses the quadrupole null its polarization electric field must

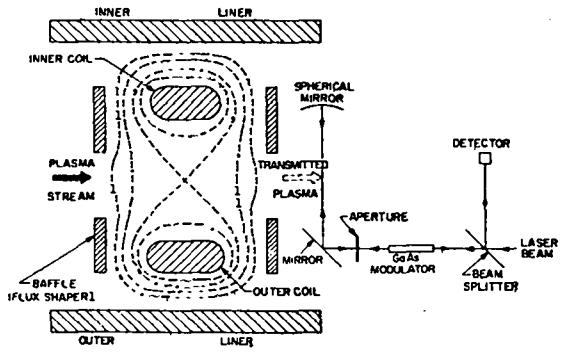

Fig. 45. The interferometer arrangement used for observing gun plasma that was not trapped by the quadrupole field.

reverse direction because it encounters a magnetic field having the opposite direction from that on the other side of the null. These two regions of opposite polarization on either side of the null are connected by magnetic field lines, and depolarization currents flow along these field lines around the coils. The depolarization currents are believed to be the means by which the forward momentum of the plasma stream is lost; that is, they are responsible for the trapping of the plasma in the containment region. A measurement of the depolarization currents was obtained with Rogowski loops in the bridge region as shown in Fig. 42. Peak currents of about 5 kA were observed, having a pulse time of 5 to 15 μsec. The resulting $\vec{j} \times \vec{B}$ impulse is what would be expected for eliminating the momentum of the plasma stream.

A CO_2 laser interferometer was set up to observe the plasma passing completely through the quadrupole field, as is shown in Fig. 45. The peak density across the stream was several tenths of a fringe for the case when the quadrupole field was not present. As the quadrupole field was increased from zero, the amount of plasma observed decreased until it was below the detectable limit at 1/2 the peak design field.

From these measurements, we conclude that the plasma is indeed polarizing as it crosses the quadrupole field, that depolarization currents are flowing along the B lines as we had hoped they

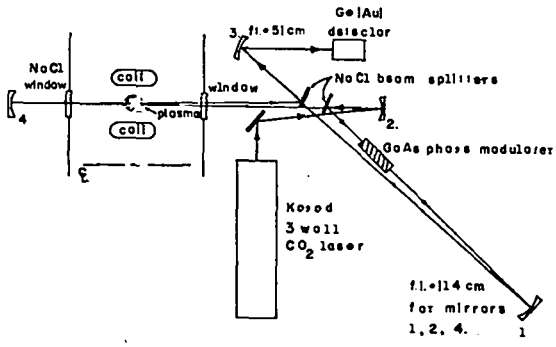

Fig. 46. "Misaligned" Michelson interferometer used for density measurements.

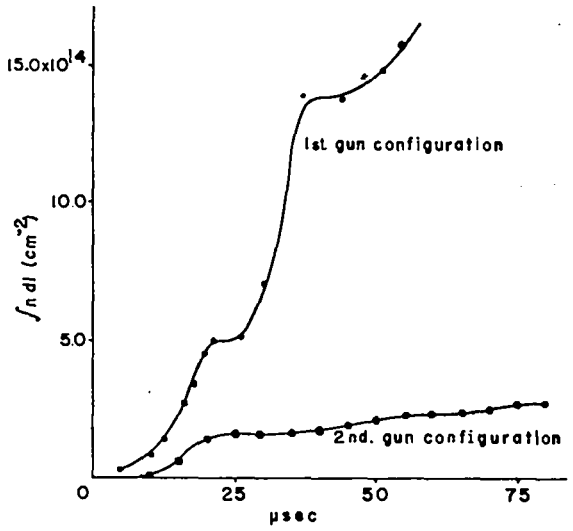

Fig. 47. Plasma density as a function of time for two different configurations of the insulators between the gun and the baffle rings.

would, and (taking into account other measurements described below) that the trapping is quite efficient (perhaps > 50%).

MEASUREMENTS IN THE MAIN CONTAINMENT VOLUME. A major effort of our group has been to develop a CO_2 laser interferometer for obtaining area density measurements of the plasma. An unsuccessful first attempt was to use an Ashby-Jephcott configuration (in which the light beam after traversing the plasma is coupled back into the laser cavity and modulates the output of the laser). The most obvious symptoms of the difficulties encountered with this configuration were:

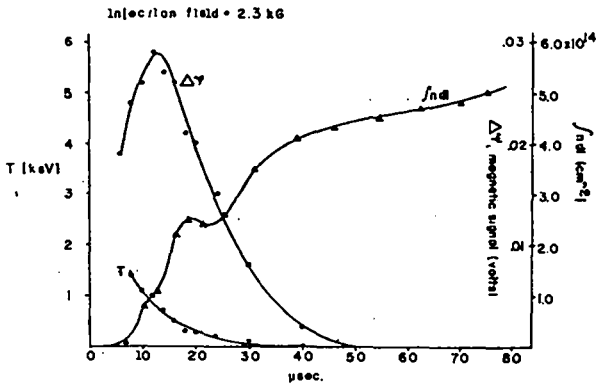

Fig. 48. Diamagnetic signal, plasma density, and plasma temperature for an injection field of 2.3 kG.

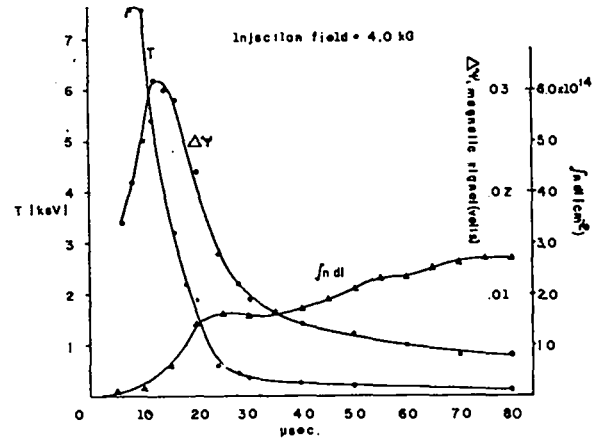

Fig. 49. Diamagnetic signal, plasma density, and plasma temperature for an injection field of 4.0 kG.

(a) approximately flat instrument response occurred only over the frequency range of 50 kHz to 175 kHz, (b) non-reproducible results for the plasma density which were not physically reasonable. An extended series of experiments indicated that the source of the problem was a nonlinear response of the laser output to the feedback signal. We were, therefore, led to try an interferometer geometry that avoids any return beam into the laser. The "misaligned" Michelson interferometer that we have employed very successfully for these measurements is shown in Fig. 46. The sensitivity of this instrument is better than 1/100 of a fringe. The GaAs crystal is modulated at a frequency of 200 kHz-300 kHz and at a magnitude such as to produce a variation

in the optical path of from 1/15 - 1/50 of a wavelength. This additional modulation is useful for interpreting signals of 1/4 fringe shift or larger, otherwise it is not necessary and can be removed. A special feature of the interferometer is an electronic discriminator which initiates the experiment when the low frequency (~ 50 Hz) room vibrations have resulted in the two interferring beams being at a phase angle of $\pi/2$ from in-phase (the most sensitive region of the interferometer).

Typical results for the area density as a function of time are shown in Figs. 48 and 49. The decrease in the rate of rise of the density at about 25 μsec is observed on nearly every shot. In general, the peak density occurs at from 75 to 100 μsec and decays in several hundred microseconds. All of the data obtained so far are for an azimuthal position which is 90° from the dipole-guarded coil supports and 75° from the injection region. As discussed below, it is believed that the density rise after about 20 μsec or so is due to an influx of cold plasma. The source, or sources, of this cold plasma have not yet been identified but good possibilities are: a) it could be coming from the gun itself, b) it could be coming from bombardment of surfaces at or near the baffle rings occurring as the plasma passes through this region on its way into the quadrupole field, c) an unguarded coil protrusion at the coil feeds that is known to be bombarded by the hot plasma, d) bombardment of the coil and liner surfaces themselves. The magnitude of the cold plasma influx can be greatly influenced by altering the gun parameters (voltage, gas load, etc.) or by altering the geometry of insulators in the region between, and around, the gun and the baffle rings. Figure 47 illustrates the effect of changing the insulator geometry. Similar results are obtained when gun parameters are changed.

Although most of the density measurements were taken along a line passing through the quadrupole null, we have taken a few measurements along lines displaced one and two inches from the null towards either coil. The interpretation of the density profiles so obtained is made difficult by the normal shot-to-shot variations that we observe, but within these variations there seems to be an essentially flat area density profile over the 4-in. spread centered on the null for the early hot plasma. The later cold plasma profile peaks slightly toward the center. The observed area density profile can be compared to the predictions of various models for the plasma distribution. Comparison with a distribution of the form $1 + \cos/2$, as in the model of Baker and Mann discussed below, suggests that hot plasma is either centered on the separatrix, or perhaps, displaced slightly outward towards the liners and baffles with the late cold plasma having a narrower distribution.

Plasma energies have been inferred from the flux change in a magnetic pickup loop positioned outside the plasma. In order to get a plasma energy from the magnetic loop signal, a model for the plasma distribution must be made. For this purpose the model used by Baker and Mann in the finite β MHD calculations on the quadrupole is used to relate the magnetic loop signal to the plasma energy. This model assumes an azimuthally symmetric isotropic plasma pressure which varies with ψ, the flux function, as

$$P = \frac{P_o}{2}\left[1 + \cos \pi \frac{\psi - \psi_o}{\psi_1 - \psi_o}\right] .$$

For the case of plasma centered on the separatrix, ψ_o is the flux surface for the separatrix and ψ_1 corresponds to the edge of the plasma distribution. The measurement technique is then to place a magnetic loop just outside the plasma and calculate the plasma energy given by the model for the flux change observed by the loop. Temperature is then obtained from this, using the area density given by the interferometer.

Figures 48 and 49 show the diamagnetic signals, labeled $\Delta\psi$, as well as the measured area density and the deduced plasma temperature plotted as a function of time for two different strengths of the main quadrupole field. It is seen that the density rise occurs with the temperature drop, giving rise to the interpretation that the main density signal is due to an influx of cold plasma. Also, it is evident that the higher-valued quadrupole field gives a much longer energy containment time.

The values for T given in the figures are calculated with the plasma distribution assumed to be centered on the separatrix. The flux change for a distribution off the separatrix was also calculated by Baker and Mann. The two off-separatrix cases were centered on flux surfaces on both sides of the separatrix equal to 1/3 the distance in flux from the separatrix to ψ_{crit}. For the distribution displaced toward the coils, the measured loop would indicate a temperature of about 0.7 of that given. For the opposite displacement, the experimental $\Delta\psi$ would give a calculated temperature more than 5 times that shown in the figures. This would say that the plasma temperature cannot be much lower than that shown in Figs. 48 and 49 even with large displacements of the plasma from the separatrix.

The results of the time history of temperature and density with B as a parameter clearly show that two avenues must be taken in the experiment .

1) The magnetic field strength for the present gun energies is much too small for effective containment. The B field must be pushed toward design strength.

2) Further efforts to control the gun output are needed, and the sources of the cold plasma must be identified and eliminated.

Time-integrated photographs of the insulators in the coil shroud show no evidence of the insulators being hit by the plasma as long as the coils are crowbarred. This presumably means that the main plasma loss is not by following the B field lines back into the coil as the field decay. At present this is not understood.

MEASUREMENTS IN THE DIPOLE REGION

Double probe measurements of the electric field in the dipole region have been made. The probes were located near the outer liner on magnetic field lines which go into the dipole region. As illustrated in Fig. 50, there were three probes oriented such that they measured the electric fields which would transport plasma out of the containment region. The electric fields were found to have a peak value of about 100 V/cm and to last for only about 25 μsec. These measured values are

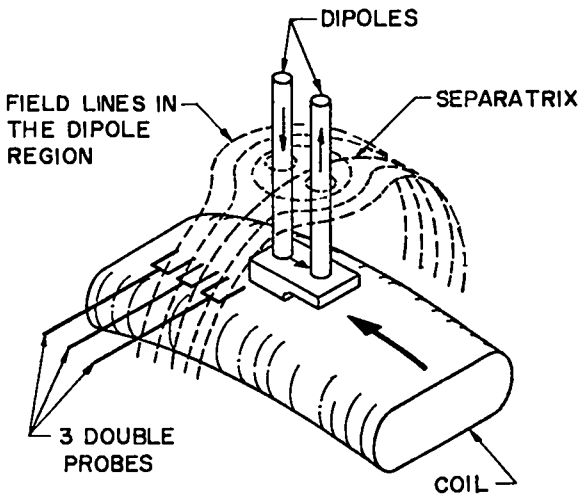

Fig. 50. Schematic diagram showing the position of the double probes used for the electric field measurements in the dipole region. The unguarded protruding dipole crossover piece is also shown.

less than 10% of the value predicted by the model of Meade or by the model of Baker, Hammel, and Sherwood presented in the next section of this report. On a majority of the shots, the largest electric field was seen by the double probe which straddled the dipole separatrix. In some cases the ratio of the signal from this central probe to the signal from the side probes was about 5. Although the probe on the separatrix always gives a field direction which would transport plasma out of the machine, a reverse E field on the side probes is observed on some shots indicating some circulation of the plasma in this region.

Time-integrated photographs of the vicinity of the dipole-guarded supports have been obtained. These photographs show that the dipole supports themselves are not being bombarded by the hot plasma. A thin line of light was seen at the position of the dipole null. These observations are consistent with our present level of knowledge of the effect of the dipole guard field.

It was also observed, however, that the crossover piece at the base of the dipole which protrudes above the surface of the coil (see Fig. 50) is being bombarded by the plasma. Time-resolved photographs have shown that the bombardment of

this unguarded element begins about 10-12 μsec after the gun current starts, which is just about what is expected for the transit time of the fast gun plasma to this area. New coils on which this dipole crossover element has been located below the surface of the coil have been designed and are being fabricated.

DIPOLE SHIELDING MODEL.

Model. The magnetic field, due to the dipole-guarded current feed, upsets the plasma equilibrium that one would expect for the quadrupole field alone. The purpose of this work is to attempt to calculate the expected plasma loss due to this upsetting of the equilibrium. We use a simplified model similar to that used by Meade[1] in which an infinite dipole is placed in a uniform background field. We maintain that the actual physical situation in the experiment is much more complicated so the model is quite crude.

The spirit of our model is that we have a large reservoir with a small hole. As in the case of a large tank with a small hole in its side, we determine the loss rate by calculating the unbalanced force (on the plasma) in the region of the hole (dipole) assuming an undisturbed density distribution. An effective loss area, or "hole size," is that size of hole which gives a plasma momentum flow equal to the unbalanced force.

We can consider the plasma loss due to the dipole to be composed of two parts. First, there is a loss due to the complete lack of pressure balance for the plasma in the region of the two magnetic field line nulls that are present where the dipole field just cancels the background field. But in the model plasma is also lost because the unbalanced forces on the plasma exist over an extended region away from the nulls. This latter loss has been treated with the simplified model (see Fig. 51). The result of this treatment gives an "effective hole size,"

$$A = \int_{\psi_1}^{\psi_2} \int_{-\Delta y/2}^{+\Delta y/2} \frac{d\ell}{B}\, d\psi - \frac{(\psi_2 - \psi_1)\,\Delta y}{B_o} \qquad (1)$$

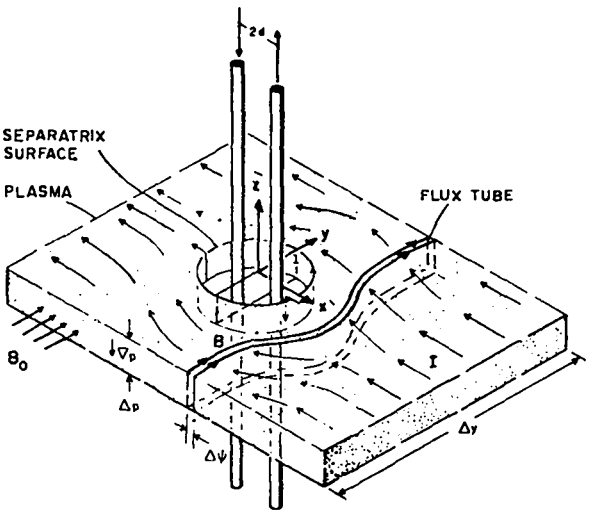

Fig. 51. The geometry of the model.

ψ is the flux function describing the field and is related to the vector potential $\vec{A}$ as follows:

$$\vec{B} = \nabla \times \vec{A}$$

$$\vec{A} = \hat{z}\,\psi$$

where $\hat{z}$ is a unit vector in the z direction.

NUMERICAL RESULTS. Consider first the case where the dipole current makes the dipole force-free. Figure 52 shows a graph of $\int d\ell/B$ (in arbitrary units) for various field lines plotted against the value of x/d at y = 0 for the field line in question (2d is the dipole separation distance). It is seen in Fig. 52 that near the dipole $\int d\ell/B$ is greater than its asymptotic value. This corresponds to a net force on the plasma in the z direction away from the containment region. More distant field lines, however, have $\int d\ell/B$ less than the asymptotic value, and for them the force on the plasma is towards the containment region. These more distant field lines are predominant and the net force on the plasma as a whole is inward towards the containment region. This net inward force is a consequence of our choice of the boundary condition that the current very far from the dipole is undisturbed. Other choices are possible. For

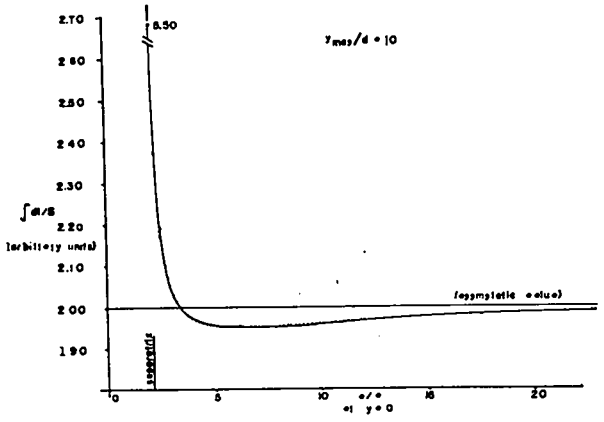

Fig. 52. $\int d\ell/B$ for a flux line vs the value of x/d at y = 0 for that line.

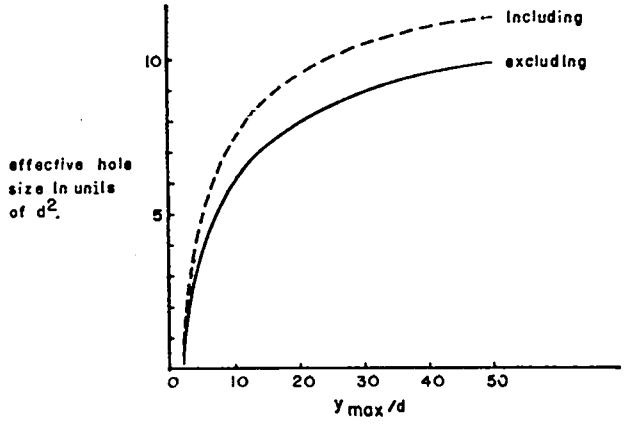

Fig. 53. Effective hole size as a function of the maximum y/d to which the $d\ell$ integration was taken. For the dotted curve the integration is taken all the way into the nulls so that the non-adiabatic region is included. For the solid curve the non-adiabatic region has been excluded.

example, Meade uses a different boundary condition, which, in the present context, can be expressed as $\int_{-\infty}^{\infty} E_x\, dx = 0$, and which gives no net force on the plasma outside the separatrix. Nevertheless, using the information presented in Fig. 52, we can perform the integrations in Eq. (1) and obtain an "effective hole size" for the outward accelerated plasma close to the dipole. For the lower limit ψ_1, we have arbitrarily chosen the outermost flux line that just grazes the nonadiabatic region (defined by $\frac{1}{B}\frac{dB}{dn} > 1$) near the nulls. For the upper limit, we choose the value ψ_2 that corresponds to the crossing over of the curve in Fig. 52 from the region where $\int d\ell/B$ is greater than its asymptotic value to the region where it is less.

The "effective hole size" we obtain from our model in the manner just outlined turns out to be $\simeq 6d^2$. This is to be compared with Meade's value of $-6\pi d^2$. The difference between the two results is due at least in part to a difference in choice of the range for the ψ integration. Meade integrated from a different upper limit (because of his different boundary conditions) all the way to the surface of the supports for his machine. Curves of $\int d\ell/B$, such as shown in Fig. 52, were obtained for various values of $y_{max} = \Delta y/2$ in the ℓ integration. The position (or ψ value) where the curve of Fig. 52 crosses its asymptotic value depends on y_{max}. Extending the integration length moves the crossover flux surface farther from the dipole.

$y_{max}/d = 10$ is an appropriate value for our machine. We also checked the effect of the length of the ℓ integration on the "effective hole size" by calculating the hole size just as before but with the ℓ integration being taken out to $y_{max} = 50d$. The value found was $\approx 10d^2$. We can also obtain a different number for the hole size by using $\psi_1 = 0$ for the lower limit of the ψ integration, i.e., by integrating all the way into the separatrix. Although this is a very questionable procedure, because our model is particularly bad close to the nulls, it does have the advantage of including all of the hole in a single calculation.

Figure 53 shows the "hole size" as a function of the y/d value to which the ℓ integration was taken for the case where the lower limit of the ψ integration is the edge of the non-adiabatic region. It also shows the case where the ℓ integration is taken all the way into the nulls.

We have extended the model somewhat by removing the condition that the dipole current be such as to make the dipole force-free. We define a parameter D which is a measure of the magnitude of the dipole current as the ratio of the dipole current to that required to make the dipole force-free. Figure 54 shows the effect of D on the hole size.

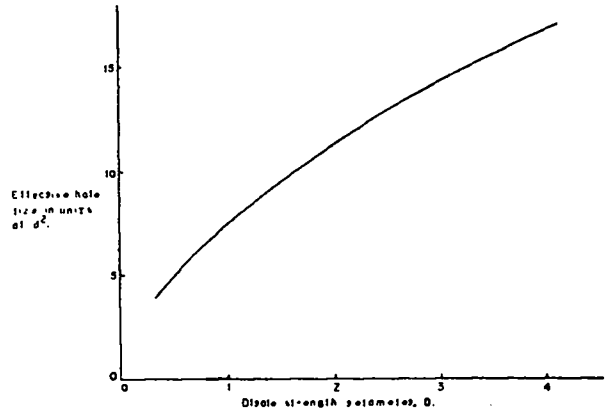

Fig. 54. Effective hole size as a function of the dipole strength parameter D. $(y/d)_{max}$ = 10, and the non-adiabatic region is included. D = 1 corresponds to the force-free condition.

Weaknesses of the Model. The long-range effects exhibited in Figs. 52 and 53 cast serious doubt as to the applicability of the present two-dimensional infinite-dipole model to our actual apparatus. When we started this work, we had hoped that the effects of the dipole would be localized enough that the model would be a reasonable approximation. This does not appear to be the case. In our apparatus the actual length of the dipole elements is about 7d and the background field becomes distinctly non-planar at about y = 4d. Also the background field is not very uniform in the z direction. Thus, it appears that a three-dimensional case would have to be solved to apply to the experiment.

Furthermore, the model is unrealistic because it fails to take into account any plasma flow and the pressure gradients associated therewith.

Reference

1. D. M. Meade, Phys. Fluids 11, 2497 (1968).

PLASMA PHYSICS

SUMMARY OF FUNDAMENTAL PLASMA GROUP ACTIVITIES (P-13)

(H. Dreicer)

During the past year we utilized the radioactive test ion technique, proposed a year ago,[1] to measure the spatial distribution of ion drift speeds in our potassium Q-machine plasma column by means of autoradiography. We find the surprising result that axial drift speeds are considerably smaller than the conventional Q-machine sheath model predicts, probably because of resonant charge exchange. The success of this technique warrants its examination by experimenters concerned with open-ended magnetic confinement geometries.

During the same period we developed a fast-transient technique for measuring the ac resistivity of the Q-machine plasma column near the electron plasma frequency. Our observations indicate that this resistivity can become anomalously large when a threshold electric field is exceeded. We believe this is due to the excitation of the ac two-stream and parametric instabilities. Although this experiment was carried out at 2 GHz with our potassium plasma, the possible scaling to higher frequencies, even into the micron wavelength laser regime, makes this work important as a guide for heating much higher density plasmas.

Studies of the electron cyclotron heated (ECH) plasma device have now reached the point where steady state magnetized plasma columns with central densities up to $10^{11}/cm^3$ and central average electron energies up to 50 eV can be obtained routinely and reproducibly in many gases including hydrogen. Recent work on this device indicates that the plasma column contains hot electrons in its interior and is surrounded by profile wings of colder electrons that have a substantial density. This status report describes a novel microwave system which we have used on the ECH device to measure electron density and to cross-check Langmuir probe measurements. The system uses a high-Q prolate spheroidal multi-mode microwave cavity with very large plasma access holes, and should find wide application for plasma heating and diagnostics in other CTR devices. Major portions of the ECH experiment constitute the Ph.D. thesis work of D. Michael who leaves the group December 31, 1970. His impending departure made available a position in our group which has been filled by J. C. Ingraham since April 1 of this year.

Theoretical work is under way on several fronts to support the experimental program. Our earlier solution to the Fokker-Planck boundary value problem has been extended in several important ways. It leads to an understanding of the spatial relaxation of velocity distribution functions, a mechanism which is especially important in steady state plasma devices. Spurred on by our autoradiographic measurement of ion drift speeds, we have formulated and solved the ion Boltzmann equation with special emphasis on the effect of charge exchange encounters upon the ion velocity distribution. This solution indicates that charge exchange encounters can explain the low ion drift speeds we observed. Finally, synchrotron radiation computations are being made to predict the spectral distribution of radiation emitted by the electrons produced with our new electron beam injector.

The task of regulating the 3 MW of dc power available for our magnets is nearing completion. All major construction work has been completed. The regulator for the 0.5 MW motor generator, which powers magnets for the ECH machine and the electron injector, is completed and provides us with current stability of 0.01%. The remainder, a 2.5 MW supply utilizing rectifiers, has been split into two 1.25 MW units. One of these has been supplying power for the potassium Q-machine magnet with a stability of 0.1%. Further improvements are expected to be completed by July 1, 1971.

Messrs. N. Gardner and A. Mondragon have provided expert assistance in all phases of the group's experimental activities.

Reference

1. LA-4351-MS.

DEVELOPMENT OF A SECOND GENERATION QUIESCENT PLASMA SOURCE: THE ECH-Q MACHINE (P-13)

(D. Michael, J. McLeod, and H. Dreicer)

We have studied the properties of a steady state hydrogen plasma column produced with a modest amount of 10 GHz microwave power near electron cyclotron resonance. Our motivation is the need for a steady state plasma, which, unlike the conventional alkali Q-machine plasma, is not restricted to 0.25 eV particle energies and to alkali ions. This research, carried out during the last two and one half years, was primarily the Ph.D. thesis research of one of us (D.M.), and with its imminent completion (12/31/70) the status of this plasma machine as a tool for further plasma research will be assessed in the near future.

By utilizing a Lisitano-like microwave coupling structure[1] with up to 200 W we are able to produce plasma columns with electron densities up to $10^{11}/cm^3$ and average electron energies up to 50 eV in any of the commonly used gases including hydrogen. The ratio of working to electron cyclotron frequency, ω/ω_B, for such operation lies within an absorption bandwidth of 1% near cyclotron resonance. By tuning ω/ω_B it is possible to produce a plasma column whose boundaries, as determined by light emission in the visible part of the spectrum, are very sharp, with emission falling to zero beyond the Lisitano coil radius. However, detailed studies of the plasma density profile made with a Langmuir probe and a new type of microwave resonator system (described elsewhere) show that the density profile does not possess a correspondingly sharp boundary. As reported by us earlier,[2] the column has extensive wings beyond the radius at which light emission ceases. We have used a novel probe design to verify that photo emission of electrons from the Langmuir probe due to ultraviolet photons is not responsible for the production of the signal when the probe is located in the wings of the density profile. This design (see Fig. 55) incorporates a Pyrex T-tube jacket around the Langmuir probe that shields against ultraviolet photons and yet permits the collection of positive ions which drift to the probe along magnetic lines. Our conclusion is that such a

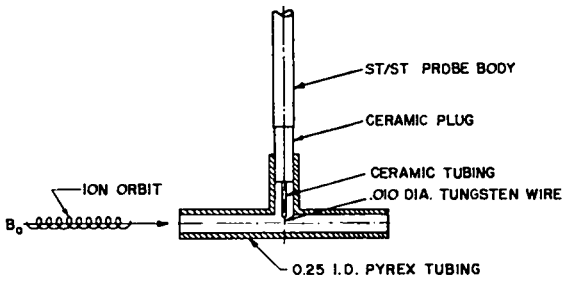

Fig. 55. Langmuir probe with ultraviolet protective Pyrex jacket.

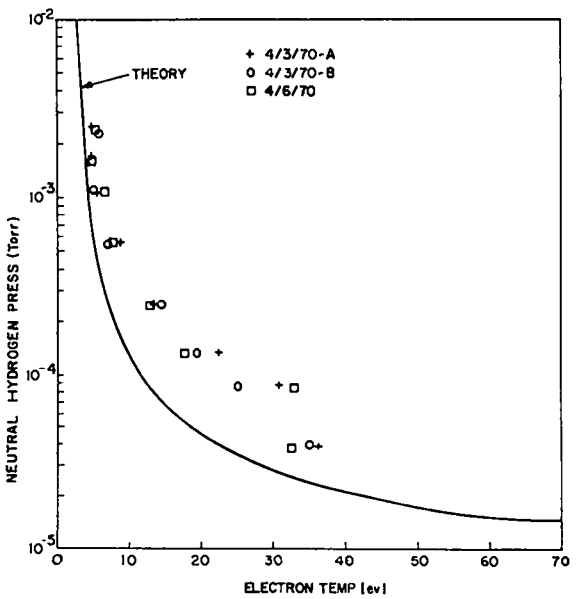

Fig. 56. Neutral hydrogen gas pressure vs average electron energy.

photo effect does not play a significant role in producing the Langmuir probe signal and that the wings of the density profile are real. This suggests the following model for the plasma column maintenance in the wings. Electrons within the Lisitano column diameter are maintained at the average energy mentioned above by repeated transits through the microwave coupling structure. When an electron diffuses across this diameter and makes an inelastic collision with a neutral atom it loses most of its energy and remains tied to its magnetic line without further heating until elastic collisions, or whatever other

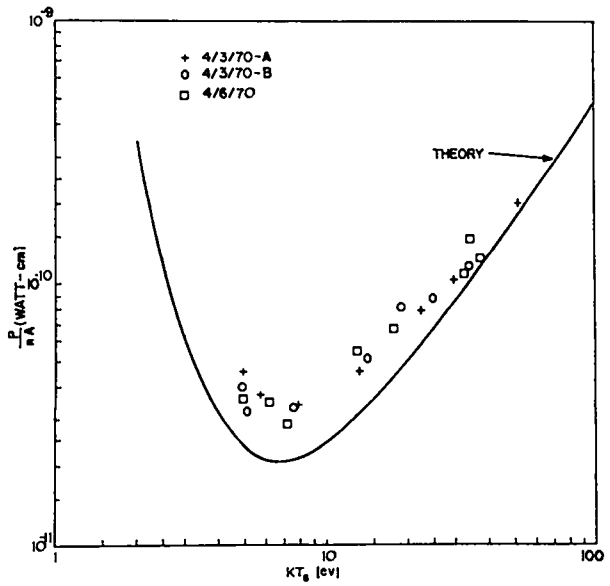

Fig. 57. Specific microwave power vs the effective electron temperature in eV.

mechanism is at work, produce further diffusion across field lines. Recent experimental evidence[3] verifies this sudden drop in average electron energy with radius at the coupling structure radius.

Our earlier theoretical analysis was one-dimensional, allowing plasma losses along field lines only. This assumption leads to predictions about the average electron energy and the microwave power requirement for steady state operation[4] which the experimental data shown in Figs. 56 and 57 largely verify. The average electron energy in these studies is deduced from a measurement of the plasma diamagnetism. A more detailed account of our measurements will become available with the publication of the thesis.

References

1. LA-4075-MS.
2. LA-4351-MS
3. L.P. Mix, Jr., E.W. Fitzgerald, and C. Bekefi, MIT-QPR No. 92, Jan. 15, 1969, p. 234.
4. LA-3831-MS.

THE PROLATE SPHEROIDAL MICROWAVE CAVITY ELECTRON DENSITY PROBE (P-13)

(J. McLeod, D. Michael, H. Dreicer)

We are using a new type of microwave resonator shaped like a prolate spheroid to obtain reliable measurements of the density of our ECH (electron cyclotron heated) plasma column by observing the change in resonant frequency when plasma is introduced into the cavity. A prolate spheroid is the surface of revolution formed when an ellipse is rotated about its major axis (Fig. 58). This novel geometry, to the best of our knowledge not used before in the field of microwave electronics, is dictated by the need for very large plasma access holes several wavelengths in diameter. The probing wavelength is limited by the combination of high central density and the need to avoid the ECH cyclotron resonance frequency (10 GHz) to a maximum of about 2.5 cm. The minimum diameter of the access hole required to avoid interference between the cavity and the wings of the ECH plasma profile is significantly larger than this maximum wavelength. Therefore the conventional low mode cavity whose access holes are protected by waveguides below cut-off cannot be utilized. Moreover, use of the conventional microwave phase shift interferometer on our ECH plasma column would involve serious systematic errors due to diffraction-refraction effects for the highest microwave frequencies we have available. To avoid

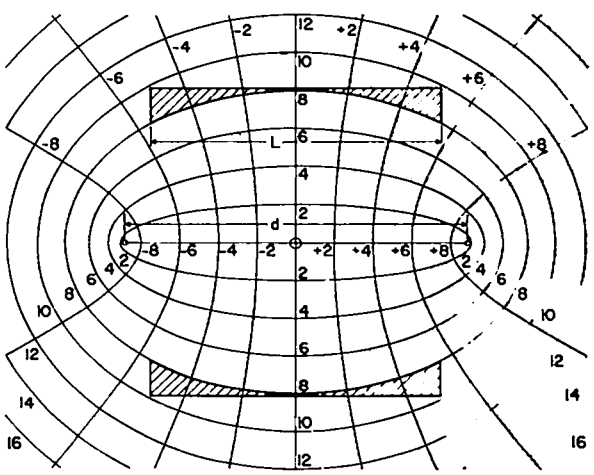

Fig. 58. Spheroidal coordinate system showing cavity cross-section.

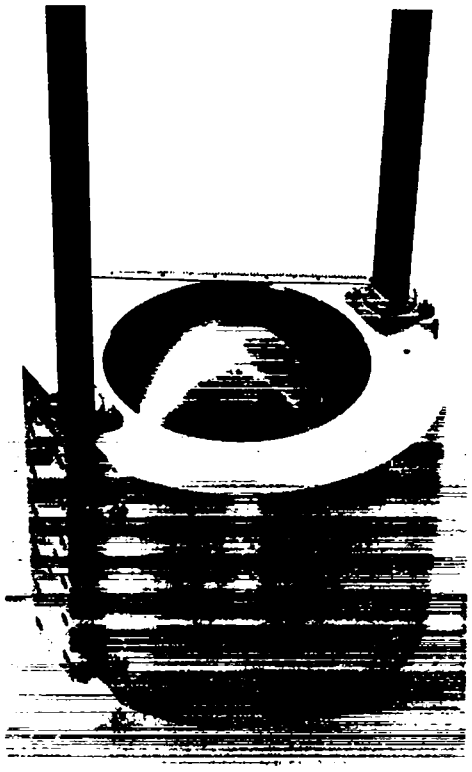

Fig. 59. KU-band prolate spheroidal cavity.

these errors requires microwave equipment operating at 150 GHz. However, phase shifts expected at this frequency are so small that apparatus rigidity becomes a serious problem instead.

We have avoided these problems with the help of the spheroidal cavity, Fig. 58, whose dimensions are many times the wavelength in KU-band (12.4 - 18.0 GHz). It supports modes, with Q's of 50,000, which are not significantly perturbed by the large, 12-cm diameter, access holes. Thus we have been able to carry out measurements without perturbing the wings of the plasma density profile at all, and all previous data taken with our diamagnetic coil have remained valid.

A high mode cavity also has the advantage that many modes are available with a variety of different spatial distributions of electric intensity. Such distributions are shown in Fig. 60 for three modes in the spheroidal cavity. The use of several modes permits reconstruction of the plasma

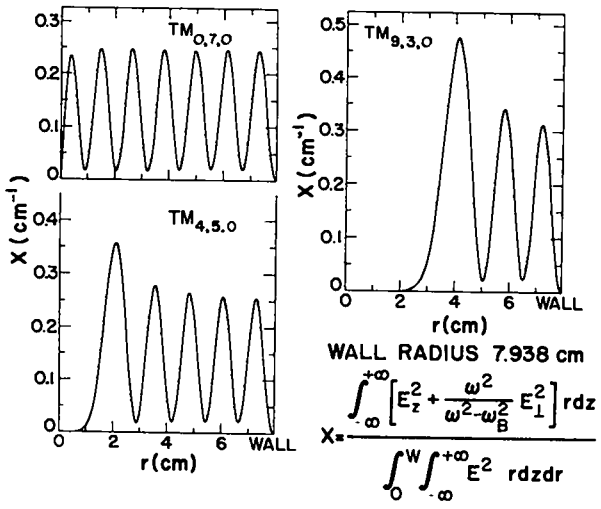

Fig. 60. Radian sensitivity functions for an axisymmetric plasma.

density profile purely on the basis of the shifts in resonant frequency measured for these modes.

Density measurements made with the spheroidal cavity have been compared with the Langmuir probe density measurements. On the average, the cavity indicates that probe theory gives too high a density by about a factor of two. However, this calibration factor varies with plasma parameters with sufficient sensitivity to indicate that a thorough mapping of parameter space may be required. On the other hand, the probe calibration factor does not change greatly between different cavity modes--which are sensitive to different parts of the density profile--when used on the same plasma. This implies that the extensive wings which appear on the Langmuir probe profiles are probably real.

A more detailed account of this work is being prepared for publication.

ELECTRON INJECTOR FOR SYNCHROTRON RADIATION STUDIES (P-13)

(D. Ignat (Post-Doctoral Appointee) and H. Dreicer)

It has been recognized for a long time that electron synchrotron radiation may result in serious power losses from fusion reactors. To understand this problem better, we have planned to study the effect of background plasma on the synchrotron radiation emitted by energetic test electrons. The design of an electron injector for producing such test electrons was described by us earlier;[1] it was placed into operation during the past year. It produces a 200-μA electron beam with perpendicular energy of about 2-5 kV (as determined with a diamagnetic coil), longitudinal energy of about 20 eV, (as determined from the Doppler shift in the electron cyclotron absorption spectrum) with a microwave power of about 10 W at 10 GHz incident on the injector. The microwave radiation emitted by this beam in vacuum is presently under study.

Reference

1. LA-4351-MS, p. 101.

VELOCITY DISTRIBUTIONS OF BOUNDED PLASMAS: SPATIAL RELAXATION (P-13)

(H. Dreicer, J.D. Thomas (NMSU)

The problem of determining the various plasma velocity distribution functions in the region between boundaries upon which they are specified involves the simultaneous solution of the Poisson equations and of the time-independent electron and ion Fokker-Planck equations with space derivatives retained. The latter take the form $\vec{v} \cdot \partial f/\partial \vec{x} = (\partial f/\partial t)_{\text{collision}}$ and, since these have not previously been solved for Coulomb forces, they represent the most formidable barrier to an understanding of this boundary value problem. Our previous work[1] in this field addressed itself to this point by considering the case of plane parallel boundaries for electrons subject to angular scattering by positive ions only, with the general space charge electric field ignored. This involved the solution of

$$\mu \frac{\partial f(x,\mu;v)}{\partial x} = A(v) \frac{\partial}{\partial \mu} \left[(1-\mu^2) \frac{\partial f}{\partial \mu} \right] \qquad (1)$$

where

$A(v) = \frac{a\Gamma}{2v^4} = a/\ell(v)$

$\Gamma = 4\pi n_p e^2 \log\Lambda / m^2$

a = distance between two plane parallel boundary walls

v = electron speed

μ = cosine of angle subtended by electron velocity and normal to boundaries: $(-1 \le \mu \le 1)$

x = spatial coordinate measured perpendicular to boundaries in units of $a/2$. $(-1 \le x \le +1)$

n_p = positive ion density

$\ell(v)$ = mean free path for an electron with the speed v to collide with a positive ion

subject to the boundary conditions

$$\left.\begin{aligned} f(-1,\mu;v) &= \alpha(\mu;v) \\ f(1,-\mu;v) &= \beta(\mu;v) \end{aligned}\right\} \quad 0 \le \mu \le 1. \qquad (2)$$

The properties of the solution to this problem have been described.[1] The status of this work at the end of 1968 is described in a paper presented at the Second International Conference on the Physics of Quiescent Plasmas.[2]

During the past year work was resumed on this problem and the following advances were made.

Solutions to Eq. (1) have been obtained with the ion density n_p allowed to be a function of x such that

$$n_p(x) = n_e(x) = 2\pi \int_{-1}^{+1} \int_{o}^{\infty} f(x,\mu;v)\, v^2 dv d\mu \quad .$$

This is a strict charge neutrality condition which satisfies the Poisson equation with a zero space charge electric field everywhere in the plasma.

The solution to the inhomogeneous Fokker-Planck problem, i.e., Eq. (1), with its right hand side supplemented by a source term $S(x,\mu,v)$, has been constructed.

The completeness of the functions used to represent the solution to Eq. (1) has been demonstrated.

Equation (1) has been solved with mirror machine boundary conditions, i.e., reflective boundary conditions at $x = \pm 1$ over part of the μ range, which replace those in Eq. (2). This solution describes electron velocity distributions as a function of position in a steady state mirror machine in which electron scattering into the loss cone is due to electron-ion encounters only.

More details about these developments will be made available in an article being prepared for publication.

References

1. H. Dreicer and W. B. Riesenfeld, LA-3831-MS. H. Dreicer and J.D. Thomas, LA-4075-MS.
2. H. Dreicer, J. D. Thomas, and W. B. Riesenfeld, Proceedings of the Second International Conference on the Physics of Quiescent Plasmas, Paris, 1969, Volume III, p. 1.

ANOMALOUS AC PLASMA RESISTIVITY FOR LARGE AMPLITUDE ELECTRIC FIELDS NEAR THE ELECTRON PLASMA FREQUENCY (P-13)

(H. Dreicer, J. C. Ingraham, D. B. Henderson, F. E. Wittman)

The ac resistivity ρ of a plasma column has been measured as a function of the amplitude E of the ac electric field for a range of plasma densities in the neighborhood of the critical density. The measurement is carried out with a high-Q, 2 GHz TM_{010} microwave cavity that surrounds a steady state magnetized thermally ionized potassium column. Our Q-machine is used for this purpose. By varying the flux of neutral potassium atoms directed at the Q-machine hot plate, we vary the plasma density in the range $0.2 \leq \omega_{po}^2/\omega^2 \leq 2.0$ where ω_{po}, the plasma frequency, is defined at peak density of the density profile and ω is the working force. The ac resistivity is deduced from the quantity $\Delta(1/Q)$ which arises from the change in resonator Q produced by power dissipation in the plasma. A fast-transient Q measuring technique, developed by us and described separately, permits a determination of Q and avoids the effects of plasma density fluctuations upon the cavity's resonant frequency. Below $\omega_{po}^2/\omega^2 = 1.4$, we find that $\Delta(1/Q)$ is consistent with a resistivity ρ due to classical electron-ion encounters that decrease with increasing E because of ohmic heating of electrons. This effect is illustrated in Fig. 61a and 61b, where curves of microwave power transmitted by the cavity as a function of frequency are shown for two different levels of incident power at $\omega_{po}^2/\omega^2 = 1.4$. Figure 62a, produced with an incident power of 1.7 W, represents a cavity Q of 1.7×10^4, while Fig. 62b, produced with 0.17 W, represents a Q of 1.35×10^4. The distortion of these response curves and the beats observed on their high frequency wings are due to the fast-transient Q measurement.

Near and above $\omega_{po}^2/\omega^2 = 1.8$, we find that ρ decreases similarly with increasing E until the threshold value $eE_t/(m\omega) = \gamma\sqrt{2kT_e/m}$ in ac electron drift speed is reached, above which ρ suddenly increases. Figures 62a and 62b, respectively, illustrate this effect for incident powers of 1.74 W (corresponding to Q = 4800) and 0.15 W (corresponding to Q = 8000). The factor

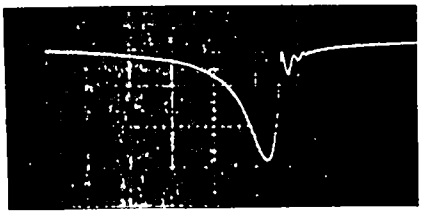

(10 μsec/horizontal division = 0.296 MHz/division)

Fig. 61a. Transmitted microwave power vs frequency at 1.7 W.

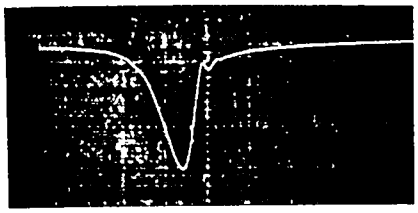

(10 μsec/horizontal division = 0.296 MHz/division)

Fig. 61b. Transmitted microwave power vs frequency at 0.17 W.

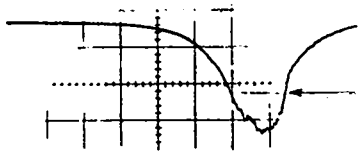

(10 μsec/horizontal division = 0.296 MHz/division)

Fig. 62a. Transmitted microwave power vs. frequency at 1.7 W.

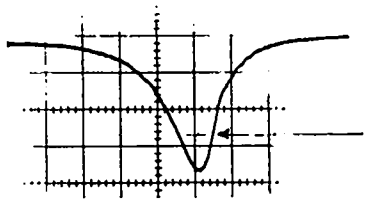

(10 μsec/horizontal division = 0.296 MHz/division)

Fig. 62b. Transmitted microwave power vs frequency at 0.15 W.

γ is found to be approximately 0.1, consistent with existing theories by Silin, Kruer, et al., and Marter et al.[1] for parametric and ac two-stream instabilities. Simultaneously with the anomalous increase in ρ, E shows evidence of low frequency plasma fluctuations at $\sim$ 1 MHz. (See Fig. 62a). Computations show that the anomalous increase in $\Delta(1/Q)$ and ρ cannot be attributed to ionization of background gas by electrons unless an anomalous resistivity first increases the electron energy considerably.

So far in our experiment, we have determined the electron density from the cavity resonant frequency shift, assuming that the radial density profile is described by the zeroth order Bessel function with its first zero at the plasma-vacuum boundary. This probably results in an overestimate in the value of ω^2_{po}/ω^2, since the profile is known to be flatter than this, and the true threshold value for the onset of anomalous resistance is probably closer to $\omega^2_{po}/\omega^2 = 1$ than quoted above. Despite this uncertainty, we believe that the parametric and ac two-stream instabilities have been observed in this experiment.

In future experiments we expect to refine the density measurement and study other plasma properties associated with the anomalous ac resistivity.

Reference

1. V. P. Silin, Proceedings of the Eighth Intl. Conf. on Phenomena in Ionized Gases, Vienna 1967, p. 205; W. L. Kruer, P. K. Kaw, J. M. Dawson, and C. Oberman Phys. Rev. Letters 24, 987 (1970); B. Marder, J. Freidberg, and C. Nielson, Bulletin of American Phys. Soc. 15, 1482 (1970).

NEW TECHNIQUE FOR RAPID Q MEASUREMENT (P-13)

(J.C. Ingraham, H. Dreicer)

An important limitation on the measurement of the Q of our plasma-filled microwave resonator is due to the inherent low frequency electron density fluctuations in the plasma.

These occur at frequencies below 10 kHz and have an amplitude that causes the cavity resonant frequency to fluctuate over a frequency range as large as several MHz. This corresponds to only a few percent change in electron density for typical operating conditions, but the several MHz range is much greater than the 100-500 kHz natural width of the cavity resonance.

Thus, it is impractical to measure the cavity Q using the usual technique of slowly sweeping the oscillator frequency over the region of the cavity resonance while monitoring the power transmitted through the cavity. It is necessary in this case either (a) to sweep the oscillator frequency sufficiently rapidly across resonance so that the electron density does not change appreciably in this time (rapid FM) or (b) to apply a resonant exciting signal to the cavity and observe the decay of the power emitted from the cavity following the rapid termination of the exciting signal. In the latter case, the power, P, decays with time according to

$$P = P_o \exp(-\omega_o t/Q) \qquad (1)$$

where $\omega_o = 2\pi f_o$ and f_o is the cavity resonant frequency. A measurement of the decay of this power yields the Q of the cavity-plasma system. This technique has so far been more difficult for us to apply, and we have developed the rapid FM technique to a greater extent. Use of this method requires that the driver frequency must be swept sufficiently rapidly across the cavity resonance to avoid appreciable change in electron density during sweep time. In our experiment this required that the driver frequency traverse the cavity resonance in times comparable with the cavity response time

$$\tau = Q/\omega_o.$$

Such fast sweep rates result in a distortion of the resonance curve observed in the transmitted power for the following reasons:

1) There is insufficient time for the cavity-stored energy to reach equilibrium with the driver power at each frequency, resulting in a reduction of cavity-stored energy and transmitted power.

2) The energy stored in the resonator at frequencies excited during earlier parts of the driver's traversal across the bandwidth has only partly decayed at later times when the driver is exciting other frequencies in the cavity. Thus a beating phenomenon occurs because of interference between energy in the cavity at the instantaneous frequency of the driver and energy at the resonant frequency, excited by the driver at earlier times.

The resulting nonstandard response curve will possess a half power bandwidth which is not simply related to the cavity Q. Thus, to determine Q, it is necessary to proceed from first principles. Such an analysis, based upon the driven harmonic oscillator equation obeyed by the field amplitudes in the cavity, has been carried out for both the reflected and transmitted signals from the cavity. The results are shown in Figs. 63 and 64, which can be interpreted with the help of the quantities v, v_o, and β defined by

$$v = \sqrt{\beta}\, t/2$$

$$v_o = \omega_o/[4Q\sqrt{\beta}]$$

$$\beta = d\omega/dt$$

where ω_o is the cavity resonant radian frequency and β is the time rate of change of the driver radian frequency. Figure 63 gives Δf, the full width at half power, as a function of β and v_o. From the measured values of Δf and β it is thus possible to determine Q with the help of Fig. 63. Measured points determined from a microwave cavity of known Q are also shown on the figure, and are in good agreement with this theory. The straight line on the figure represents the expression $Q = f/\Delta f$, for determination of Q at very slow sweeping rates, or large v_o. It is seen that for $\Delta f/\sqrt{\beta} \geq 1$ the error made in using $Q = f/\Delta f$ is less than 3%. For $\Delta f/\sqrt{\beta} = 1$, $v_o = 1.55$; that value corresponds to a time-for-traversal, Δt, of the

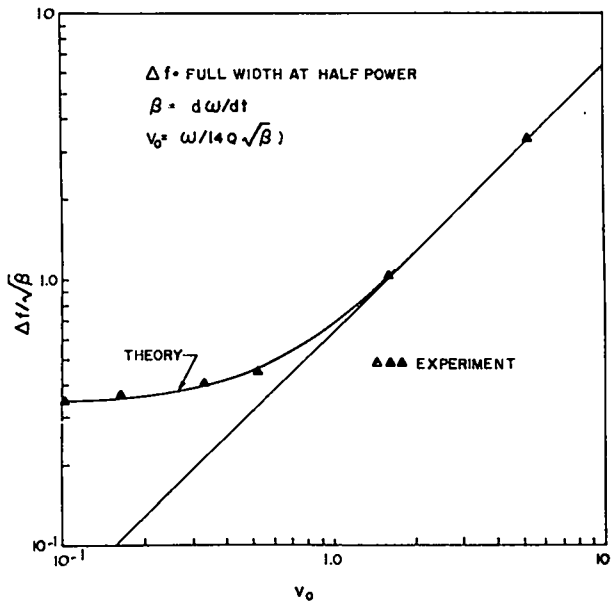

Fig. 63. Full width at half maximum of cavity resonance divided by the square root of the frequency sweep rate, and plotted vs. v_o.

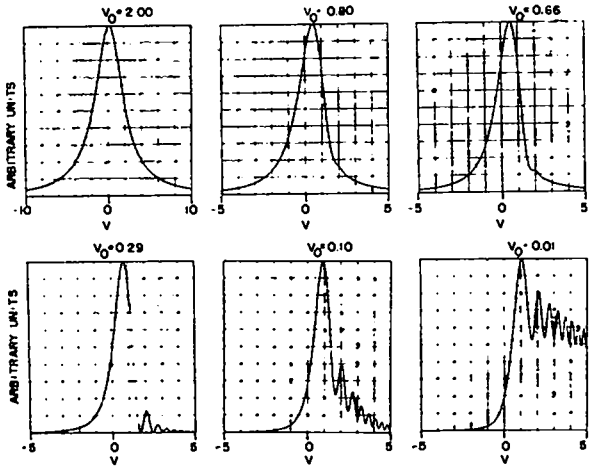

Fig. 64. Power transmitted through cavity as a function of frequency sweep rate. Decreasing v_o is increasing frequency sweep rate.

generator frequency from one half-power point of the resonance to the other of $\Delta t = (Q/\omega_o)\, 38.4$, where Q/ω_o is the energy relazation time constant of the cavity.

Figure 64 illustrates two faster and more accurate techniques for Q determination which do not require detector calibration. As shown, the resonance curve has a point of inflection near $v_o = 0.66$; near $v_o = 0.29$ the first and second minima are equal. More exactly, the values of these quantities are $v_o = 0.665$ and $v_o = 0.292$, respectively. Thus, by observing the transmitted power on an oscilloscope trace while the frequency sweep-rate is slowly adjusted, either of these points can be determined to a high degree of accuracy. With a knowledge of β from the calibrated sweep generator, the cavity resonant frequency, and v_o from the wave form (either 0.292 or 0.665) Q is immediately determined.

These results have been used to interpret anomalous resistivity measurements on our Q-machine plasma column. D. B. Henderson aided in the computer evaluation of the formulae leading to Fig. 64.

USE OF RADIOACTIVE TEST IONS IN THE MEASUREMENT OF THE SPATIAL DISTRIBUTION OF PLASMA ION DRIFT SPEEDS (P-13)

(H. Dreicer, D. B. Henderson, D. Mosher, E. Wittman)

According to presently accepted ideas,[1] the steady state operation of a magnetized single-ended Q-machine plasma column involves the production of positive ions by contact ionization on a hot plate and their subsequent acceleration in a thin electrostatic sheath situated adjacent to the hot plate. The same sheath serves to reduce the current of thermionically emitted electrons so that a quasi-neutral plasma develops between the sheath and a cold collecting plate located farther downstream. A standard method of determining[2] the total ion flux leaving the hot plate consists of biasing the cold collector negatively with respect to the hot plate and monitoring the ion saturation current, $I = e\int j\,dA$ that it collects (j = ion current density, e = electron charge). We have frequently noted in our Q-machine experiments that W, the ratio of I/e to the measured line density $\int n\,dA$ (n = ion density), is smaller than the ion drift speed expected on the basis of the collisionless sheath model. This difference need not necessarily indicate a real discrepancy since W does not in general equal the space average drift speed $\int (j/n)\,dA/A$. To investigate this point it is necessary to measure the distribution of both the ion current density $j(r,\theta)$ and the ion density $n(r,\theta)$ as functions of the cylindrical coordinates r,θ in a plane perpendicular to the plasma axis. During the past year we used radioactive test ions in our potassium Q-machine to carry out such a measurement by means of autoradiography.

The experiment involves the production and contact ionization of radioactive ^{42}K atoms, which serve as test or tracer ions. These follow typical ion orbits and are condensed on a cold collector which terminates the plasma column. By exposing a photographic film to the radioactivity on this collector it becomes possible to obtain an autoradiographic spatial distribution of the total ion current density $j(r,\theta)$. The spatial distribution of ion density $n(r,\theta)$ is obtained from a combined analysis of the frequency shift of a microwave resonator and the spatial distribution of the ion saturation current collected by a small movable Langmuir probe. By taking the ratio j/n, we obtain the spatial distribution of axial ion drift speeds $v_d(r,\theta)$. Contours of constant j, n and v_d, obtained in this way, are shown in Fig. 65. (A detailed account of this work will be published in The Physics of Fluids.)

The measured drift speed distribution displayed in Fig. 65 is nearly constant at the value $v_d = 7 \times 10^4$ cm/sec over most of the plasma column. Significant drift speed gradients exist only near the limiter radius where they might be expected to occur. In particular our earlier suspicion that the axial ion drift speed is substantially lower than predicted by the sheath model is confirmed. For our operating regime we compute $e\Phi/kT_h = 3.7$, and the sheath drop Φ should accelerate the ions to a drift speed of 2.2×10^5 cm/sec $\left(\approx \sqrt{2e\Phi/M}\right)$ which exceeds v_d considerably. This conclusion is not altered when ion-ion and ion-electron encounters in the plasma are taken into account.

At present two slowing-down mechanisms appear to provide possible explanations for the low drift speed observed. The first of these involves the resonant charge exchange, the importance of which for Q-machine operation was pointed out by us earlier.[3] In this process, charge exchange occurs when K ions encounter the slow K atoms which form a gas cloud in front of the hot plate. Such collisions replace a fast ion with a slow ion.[4] Only a crude estimate of v_d is possible without a detailed kinetic theory for the plasma ion velocity distribution which includes charge exchange. We have recently developed such a theory. It uses measured charge exchange cross sections,[5] and indicates that a sizable fraction of the ions may be involved in charge exchange after they are accelerated through the sheath. Anderson et al.[6] recently demonstrated this effect at low plasma densities with artifically produced gas clouds. At high plasma density these authors also measure a low ion drift speed and ascribe it to charge exchange. The second possibility considers that the sheath, in producing a larger than thermal relative drift between electron and ion velocity distributions, might be a source of unstable ion

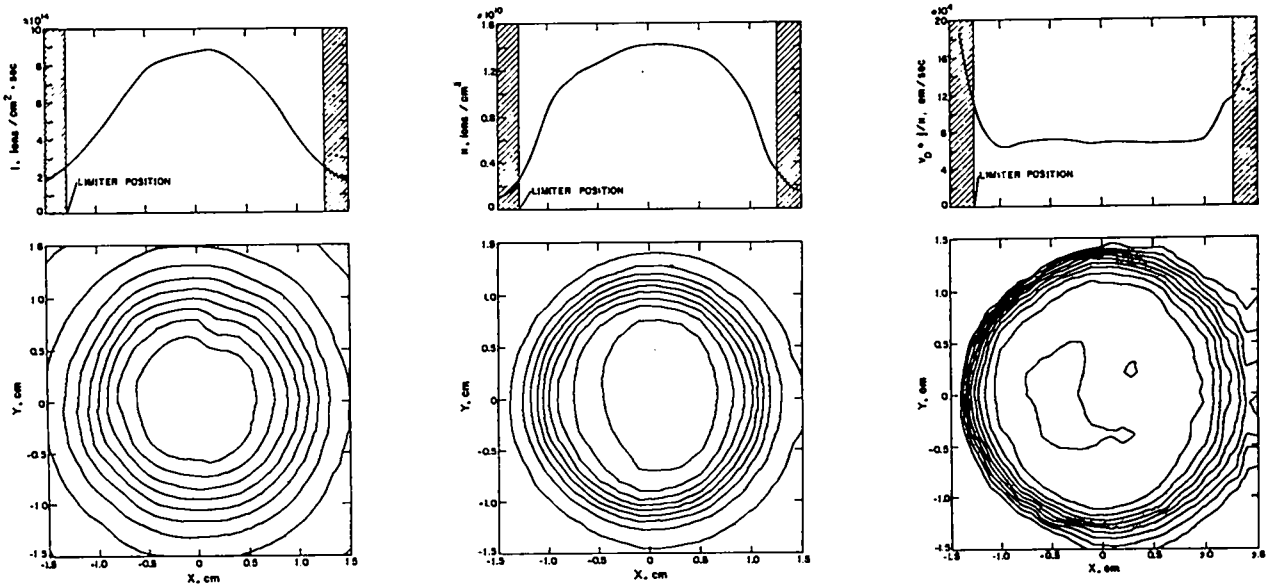

Fig. 65. Contours of j, n, and v_d at 4 kG in a plane perpendicular to the axis of the plasma column. Profiles taken along the y = 0 axis are shown above each contour plot together with the position of the limiter. (The 8 kG contours are very similar.)

plasma waves which slow down the ions. Measurements at lower background atom densities should help to clarify these matters.

Our successful use of the autoradiographic technique indicates that radioactive isotopes form an important source of test ions with which to carry out plasma measurements. The motion of such ions can be followed by detecting their radioactivity, a nuclear property that plasma collisions cannot modify. This is in contrast to optically pumped test ions[7] whose metastable lifetimes depend upon plasma conditions. Apart from the technique described here, we have also introduced radioactive ions into plasmas by charge exchange with radioactive atomic beams.[5] This charge exchange method, or that of ionizing a radioactive atomic beam by plasma electrons and ions, may be especially useful in adapting radiography to plasma studies in open-ended magnetic confinement geometries.

References

1. P. L. Auer, J. Appl. Phys. 31, 2096 (1960).

2. N. D'Angelo and S. vonGoeler, Nucl. Fusion 5, 279 (1965).

3. H. Dreicer and D. B. Henderson, Phys. Rev. Letters, 20, 374 (1968).

4. E. W. McDaniel, Collision Phenomena in Ionized Gases (New York: John Wiley and Sons, 1964) p. 244.

5. H. Dreicer, D. B. Henderson, D. Mosher, F. E. Wittman, and K. Wolfsberg, Proceedings of the International Conference on Physics of Quiescent Plasmas, Part III p. 11 Paris, September 8-13, 1969; B. M. Palyukh and L. S. Savchin, Sov. Phys. Tech. Phys. 13, 883 (1969).

6. S. A. Anderson, V. O. Jensen, P. Michelson, and P. Nielsen, Danish Atomic Energy Commission Research Establishment Risö Report QM-3.

7. D. Dimock, E. Hinnov, and L. C. Johnson, Phys. Fluids. 12, 1730 (1969).

EFFECT OF ION-ION ENCOUNTERS ON THE ION DRIFT SPEED IN A SINGLE-ENDED Q-MACHINE (P-13)

(D. Henderson, H. Dreicer)

INTRODUCTION. We have used an autoradiographic technique to measure the axial drift speed in our single-ended Q-machine plasma. (See preceding section). If we assume the sheath drop to be $3.7 \times (kT_{HP}/e)$ as indicated by collisionless sheath theory,[1] we find an axial ion drift speed greater than the measured value. At the plasma densities in our experiment, ion-ion encounters occur frequently and therefore a collisional plasma model might be more appropriate for analyzing our data. We have constructed and examined a reasonable collisional model for this purpose. In doing so we have used ideas which appear to parallel those of Anderson, Jensen, and Michelsen.[2] We find, as one might expect, that the difference between the collisionless and collisional models is not significant at moderate or high values of $e\varphi/kT_{HP}$, the ratio of sheath drop to thermal energy associated with the hot plate temperature T_{HP}.

THE MODEL. We assume the plasma potential to drop monotonically from the hot plate to the negatively biased cold collector. We assume that we may divide the column into four regions which may be approximated in length by λ_D, λ_{ii}, L, and again λ_{ii}, where the Debye length λ_D is much shorter than the ion-ion collision length λ_{ii}, which in turn is much shorter than the column length L. The first region encompasses the sheath drop φ whose physical function is to control to electron density, giving charge neutrality. Since $\lambda_D \ll \lambda_{ii}$, we know the distribution of new ions from the hot plate at the sheath edge to be a Maxwelliam distribution truncated at a minimum energy v_φ.[1] The third region is the useful length of plasma column, in which we hope to define the ion distribution in terms of three simple parameters (A, v_o, T), independent of axial position, by

$$f_p = A \exp\left[-m\left[(v-v_o^2) + v_\perp^2\right]/2kT\right].$$

There may also be some plasma ions which return over the barrier φ and are lost to the hot plate. In order to include this effect precisely, one would have to solve the Boltzmann equation in region two. Instead we make alternate use of two extreme assumptions about these reflected ions:

1. There are no reflected ions, and
2. The plasma extends back to the sheath edge, and the distribution function of the reflected ions is given in terms of f_p.

One expects the proper solution to lie between assumptions 1 and 2. Since the results are insensitive to these assumptions for $e\varphi/kT_{HP} > 1$, we feel that the reflected ions are not important in the region of interest. Regions two and four are transitions with spatially dependent distribution functions determined by ion-ion collisions. They do not enter the present model, except in the heuristic arguments given.

With the distributions one may solve for the density, the mass flux, the pressure, and the energy flux. The conservation laws then relate the parameters A, v_o, and T to the plasma density, the sheath drop, and the hot plate temperature.

QUASI-NEUTRAL TRANSITION. The density of new ions at the edge of the sheath is less than the density in the plasma. Presumably this change in density occurs over the quasi-neutral region. Taking the electron density to be

$$N_e = N_{eo}\, e^{-e\varphi/kT_e}$$

($-\varphi$ because of the previous convention), we find that an electric field

$$E = -\left(-\frac{d\varphi}{dz}\right) = -\frac{1}{n}\frac{dn}{dz}\frac{kT_e}{e}$$

is required to retard the ions in traversing region two. We include this field but neglect collisions and reevaluate the moments of the Boltzmann equation for the plasma. This additional field must also change the plasma potential from its original sheath drop value. Thus the plasma potential is more positive than the base of the sheath by an amount

$$\Delta\varphi = \frac{kT_e}{e}\, \ell n \text{ (density ratio across the quasi-neutral transition).}$$

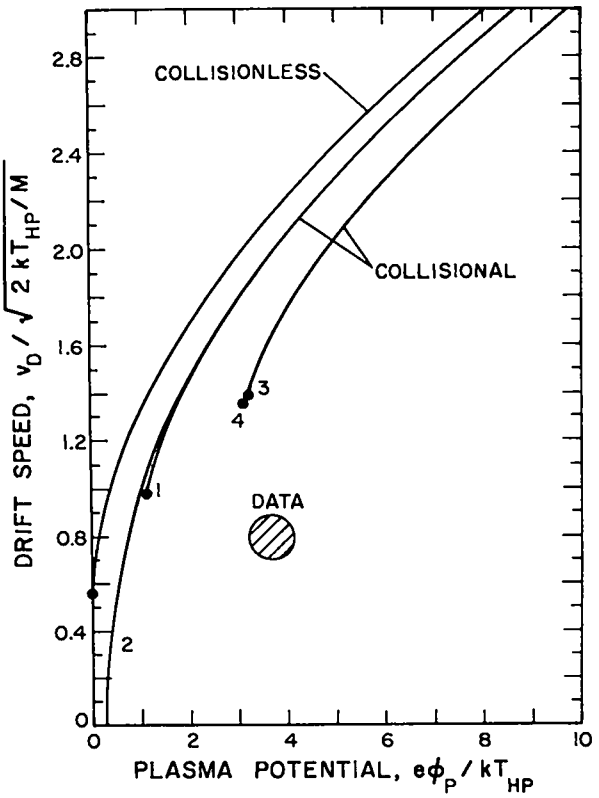

Fig. 66. Drift speeds from collisionless models.

It is desirable to compute the solution with and without this quasi-neutral transition since the ad hoc way in which the additional field is introduced is not fully self-consistent.

NUMERICAL RESULTS. The resulting nonlinear equations have been solved under the various assumptions: with and without reflected ions, and with and without a quasi-neutral transition. This has been done with a recursive computer SUBROUTINE SOLVE, written by John Hancock of Group C-4. Hancock also provided some assistance in using SOLVE.

In Fig. 66 we plot the drift speed vs the plasma potential $e\varphi_p/kT_{HP}$. In the figure, curve "1" denotes the collisional model with no reflected ions and no quasi-neutral transition; curve "2" has reflected ions, curve "3" has a quasi-neutral transition; curve "4" has both reflected ions and a quasi-neutral transition. Also plotted are the results from the collisionless model,[1] and our experimental Q-machine) data from May 20 and 21, 1970. While the collisional model did not resolve our experimental problem, it is an interesting description of the ion velocity distribution in a high density single-ended Q-machine regime. We conclude from these results that the small measured value of the ion drift speed is not due to the ion-ion collisions in our plasma.

References

1. D. B. Henderson and H. Dreicer, LA-4351-MS, p. 85 (1970).

2. S. A. Anderson, V.O. Jensen, P. Michelson, and P. Nielsen, Danish Atomic Energy Commission Research Establishment Risö Report, QM-3.

PLASMA SIMULATION

PLASMA SIMULATION AND RELATED THEORY (P-18)

(D. W. Forslund, J. P. Freidberg, B. M. Marder, R. W. Mitchell, R. L. Morse, C. W. Nielson, L. Rudsinski (C-4) and C. R. Shonk (J-10))

It is a real pleasure, when working on the theory of plasma, to be able to report progress in understanding plasma experiments. Recent linear statiliby and simulation work at LASL has turned up the Electron Cyclotron Drift Instability,[1] and shown it to be capable of causing sufficient anomalous diffusion to account for the diffuse profiles seen in pinches and collisionless shock experiments. These results are obtained with realistic values of all physical parameters. There is no need to fudge conditions to fit experimental results as has been done, for example, with ion temperatures in trying to explain anomalous diffusion with ion acoustic instability. We now expect to be able to calculate field and density profiles of pinch plasmas from first principles.

Since the last annual report, two different methods have been developed for performing fully electromagnetic simulations. These have been applied to the Weibel instability[2] and to the absorption of laser light in plasmas. This latter application has shown energy absorptions as large as 40% by the instability absorption mechanism (see the paragraph on high frequency plasma instabilities by Freidberg and Marder) and has shown that the oblique angle resonance mechanism may also be important.

In addition, the old inductive (nonradiative) electromagnetic method[3] has been coupled to an electrostatic field solver in one dimension and used to study a variety of whistler and magneto-acoustic effects.

At the present time there is hardly any single time-and-length-scale plasma phenomenon for which effective numerical simulation methods have not been developed and tested. As for the multi-scale problems, which are probably more important in low density machines than in high density pulsed machines, it is beginning to appear that they can be done on different scales and combined as in many other branches of applied science. Altogether, we seem to be in a position from which the fastest progress toward controlled fusion could be made with a considerably larger ratio of computing to laboratory experiments than we have now.

References

1. D. W. Forsland, R. L. Morse, and C. W. Nielson, Phys. Rev. Letters 25, 1266 (1970).

2. R. L. Morse and C. W. Nielson, LA-4482-MS July, 1970.

3. D. O. Dickman, R. L. Morse, and C. W. Nielson, Phys. Fluids 12, 1708 (1969).

HIGH FREQUENCY PLASMA INSTABILITIES (P-18)

(J. P. Freidberg and B. M. Marder)

With the advent of high-powered lasers, and their possible use in inducing fusion, much attention has recently been given to energy absorption mechanisms. One area of interest has been absorption resulting from the nonlinear growth of high frequency plasma instabilities. These instabilities have been investigated by many authors using various approximations in different regimes. We, too, have studied the stability properties of a cold plasma under the influence of an imposed electric field oscillating at frequencies near the plasma frequency. Our theory, however, is exact and presents a global picture of the behavior.

The perturbed behavior of a plasma under the influence of an imposed electric field $E = E_o \sin \omega_o t$ is described by the two coupled ordinary differential equations

$$\ddot{\rho}_i + \frac{\omega_{pi}^2}{\omega_o^2} [\rho_i - \rho_e \exp(-ik\lambda_L \sin t)] = 0$$

$$\ddot{\rho}_e + \frac{\omega_{pe}^2}{\omega_o^2} [\rho_e - \rho_i \exp(ik\lambda_L \sin t)] = 0$$

where ω_{pi} and ω_{pe} are the ion and electrom plasma frequencies,

$$\lambda_L = \frac{eE_o}{\omega_o^2} \quad \frac{m_i + m_e}{m_i m_e} \quad , \text{ and}$$

$$\rho_{e,i} = n_{e,i} \exp\left[i \int_o^t k V_{e,i}^o \, dt \right].$$

This system can be written

$$\dot{z} = A(t) z$$

where $A(t + 2\pi) = A(t)$. The periodicity of A allows us to apply Floquet theory to the equations. The Floquet multipliers, which determine the stability properties of the system, are found numerically to a very high degree of accuracy. The regions of instability for mass ratio 1/1836 are shown cross-hatched on the $(k\lambda_L, \omega_p/\omega_o)$ plane in Fig. 67. The largest growth rates are shown in Fig. 68.

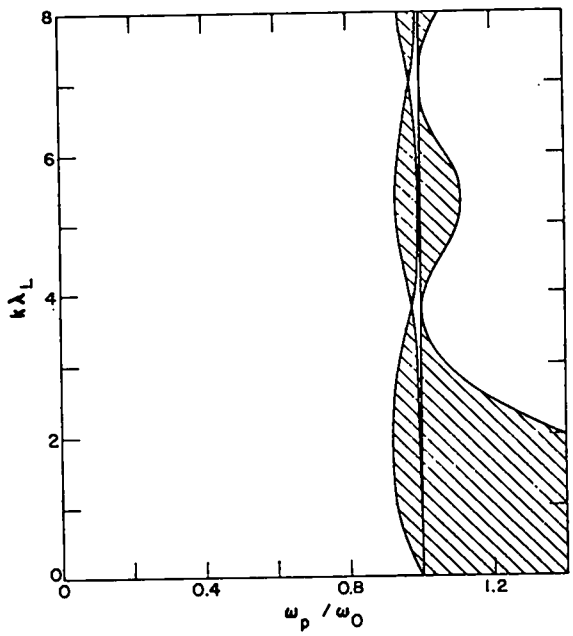

Fig. 67. Stable and unstable regions in the $k\lambda_L$ vs ω_p/ω_o.

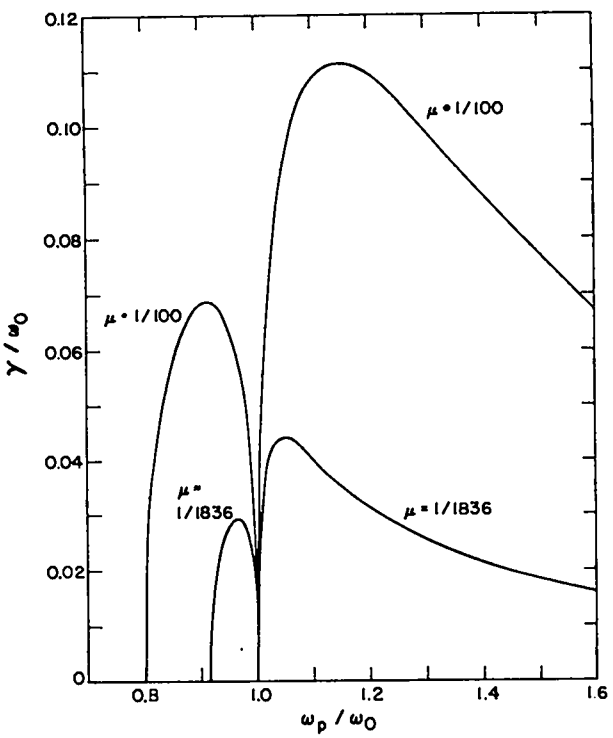

Fig. 68. Growth rates.

To supplement and amplify this work, a two-dimensional electromagnetic code was written to simulate the propagation of laser radiation into a plasma with a density gradient. Agreement with the linear theory is good and the subsequent conversion of laser energy into heat energy is on the order of 50% for mass ratio 1/100.

Finally, a theory which includes temperature effects is being studied.

LINEARIZED VARIATIONAL ANALYSIS OF VLASOV PLASMAS (P-18)

(H. R. Lewis)

The application of Hamilton's variational principle to derive numerical schemes for studying fully nonlinear Vlasov plasmas,[1,2] has been adapted to the description of linearized behavior in terms of a systemof linear, ordinary, second-order differential equations in time. The coefficients of the homogeneous part of the equations are constant in time. They depend on the equilibrium distribution functions, but can be calculated without knowledge of the equilibrium particle orbits. The inhomogeneous driving terms are time-dependent, depending on the initial perturbations of the equilibrium distribution functions and on the unperturbed orbits.

The method has been worked out in detail for a single-species, one-dimensional plasma with a uniform neutralizing background charge and periodic boundary conditions, and many numerical examples were very successfully computed. This is described in an article submitted for publication.[3] In this case an exact particular solution of the equations was found which was used to express the perturbed electrostatic potential solely in terms of solutions of the homogeneous equations. In addition, a useful explicit form of the secular equation for the eigenvalues of the truncated homogeneous equations was found. This form allowed an interpretation of the eigenvalues in terms of beams in velocity space and was useful for computing the eigenvalues numerically. The method is applicable for nonanalytic equilibrium velocity distributions as well as analytic ones. To illustrate the utility of the method, numerical examples were worked out for a single Maxwellian, sums of two Maxwellians, and several nonanalytic distributions that are bounded in velocity and represented by cubic spline functions. Excellent results were obtained. Good quantitative agreement was obtained in a comparison of Landau damping rates and growth rates obtained by this method with those obtained by precise solution of the usual dispersion relation[4] for cases in which the

equilibrium velocity distribution was a Maxwellian or a sum of two Maxwellians. The numerical aspects of this work were done in collaboration with J. R. Neergaard, B. L. Buzbee, D. K. Kahaner, J. H. Hancock, and J. R. Sopka of C-Division; and by G. H. Golub, a LASL consultant.

For the general case, including external fields and magnetic forces, no application has been made as yet. However, it is thought that an exact particular solution of the equations has been found in analogy with the one-dimensional case described above. Part of the proof has been carried out, but it has not yet been possible to prove or disprove that the remainder of the proof is possible. If the proposed particular solution is correct, then it can be used to express the scalar and vector potentials of the perturbed electromagnetic field solely in terms of solutions of the homogeneous equations. Further investigation of this point in terms of a simple inhomogeneous equilibrium is planned.

References

1. H. Ralph Lewis, chapter in Methods in Computational Physics (Academic Press, Inc., New York, 1970), Vol. 9, edited by B. Alder, S. Fernbach, and M. Rotenberg.
2. H. Ralph Lewis, J. Comp. Physics 6, 136 (1970).
3. H. Ralph Lewis, "Linearized Variational Analysis of Single-Species, One-Dimensional Vlasov Plasmas," Los Alamos preprint LA-DC-11349.
4. D. W. Forslund, private communication.

NUMERICAL SIMULATION (P-18)

(H. R. Lewis)

Charge and energy conserving numerical simulation schemes have been derived from the variational principle for the case in which there are external fields and both electric and magnetic forces in general geometries. This represents an extension of the application of the variational principle to numerical simulation given previously.[1,2] This formulation should be useful for numerical simulation studies.

References

1. H. Ralph Lewis, chapter in Methods in Computational Physics (Academic Press, Inc., New York, 1970), Vol. 9, edited by B. Alder, S. Fernbach, and M. Rotenberg.
2. H. Ralph Lewis, J. Comp. Physics 6, 136 (1970).

NUMERICAL SIMULATION WITH A CONTINUOUS DISTRIBUTION OF INITIAL PARTICLE POSITIONS (P-18)

(H. R. Lewis with K. J. Melendez, C-4)

A different approach to the numerical treatment of Vlasov plasmas has been worked out in which the particles are distributed continuously. This is an outgrowth of previous work (see Section V of reference 1). A major objective is to significantly decrease the computer storage requirements compared to the storage necessary for simulation with discrete particles. Although only the relatively simple problem of electrostatic oscillations in one dimension has been considered so far, the approach can be extended to include more dimensions and magnetic forces.

In the one-dimensional electrostatic problem we allow only a discrete set of initial velocities, but for each initial velocity we let the particles be distributed continuously with respect to their initial positions. (The restriction to a discrete set of initial velocities was made for convenience, and is probably not necessary.) For each initial velocity the time-dependent particle position is approximated as a time-dependent piecewise linear function of initial position. The values of position at the nodes of these piecewise linear functions are the dynamical variables. Between each pair of adjacent nodes a continuum of particles is represented, and this should lead to a significant reduction in the computer storage requirement by reducing the number of dynamical variables required. The equations of motion are determined from the variational principle.

The use of piecewise linear functions has two important consequences. In the first place, when piecewise linear functions are used, it was found that the electric field can be calculated in closed form in terms of simple functions. In the second place, definite integrals that occur in the equations of motion, and which must be evaluated at each time step, can also be calculated exactly in closed form in terms of simple functions. This overcomes a difficulty that was encountered in the previous attempt to treat a continuum of particles (see Section V of reference 1).

Reference

1. H. Ralph Lewis, chapter in Methods in Computational Physics (Academic Press, Inc., New York, 1970), Vol. 9, edited by B. Alder, S. Fernbach, and M. Rotenberg.

PAPERS PUBLISHED OR PRESENTED

DiMarco, J.N. Burkhardt, L.C.	Characteristics of a Magnet Energy Storage System for Using Exploding Foils.	J. Appl. Phys 41, 3894-9 (1970).
Lewis, H. R., Jr.	Energy Conserving Numerical Approximations for Vlasov Plasmas	J. Computat. Phys. 6, 736-41 (1970).
Morse, R. L. Freidberg, J. P.	Rigid Drift Model of High Temperature Plasma Containment	Phys. Fluids, V. 13, p. 531-13 1970.
Wesson, J. A.	Dynamic Stabilization and the Rayleigh-Taylor Instability	Phys. Fluids, V. 13, p. 761-6 1970.
Freidberg, J.P. Wesson, J. A.	Ion Drift Wave Instability	Phys. Fluids, V. 13, p. 1009-16 1970.
Freidberg, J. P. Wesson, J. A.	Instability of the M = 1 Mode of a Rotating Theta Pinch	Phys. Fluids, V. 13, p. 1117-8 1970.
Montgomery, D.W. Nielson,C.W.	Thermal Relaxation in One and Two Dimensional Plasma Models	Phys. Fluids, V. 13, p. 1405-7, 1970.
Friedberg, J.P.	MHD Stability of a Diffuse Screw Pinch	Phys. Fluids, V. 13, p. 1812, 1970.
Oliphant, T.A.,Jr. Nielson, C.W.	Simulation of Binary Collision Processes in Plasmas	Phys. Fluids, V. 13, p. 2103-7 1970.
Ribe, F.L. Rosenbluth, M.N.	Feedback Stabilization of a High Beta Sharp Boundaried Plasma Column with Helical Fields	Phys. Fluids, V. 13, p. 2572-7 1970.
Morse, R.L. Stovall,E.J.,Jr.	Spontaneous Field Reversal in Theta Pinches	Phys. Fluids, V. 13, p. 2867-70 1970.

Boicourt, G. P.	Problems in the Design and Manufacture of Energy Storage Capacitors	LA-4142-MS 1970.
Caird, R. S., Jr. Fowler, C.M. Garn, W.B. Henins, I. Ingraham, J.C. Jeffries, R.A. Kerr, D.M., Jr Marshall, J., Jr. Thomson, D.B.	Payload Development for a High Altitude Plasma Injection Experiment	LA-4302-MS 1970.
Weitzner, H.	Adiabatic Invariant for Particles in Toroidal Devices and its Possible Application to the Computation of Toroidal Equilibrium	LA-4323-MS 1970
Phillips, J.A.	Proposal for a Shock Heated Toroidal Z Pinch Experiment	LA-4352, 1970.
Morse, R.L. Nielson, C.W.	Numerical Simulation of the Weibel Instability in One and Two Dimensions	LA-4482-MS 1970.
Forslund, D.W. Morse, R.L. Nielson, C.W.	Electron Cyclotron Drift Instability	LA-4487-MS 1970.
Morse, R.L. Nielson, C.W.	Studies of Turbulent Heating of Hydrogen Plasma by Numerical Simulation	LA-4510-MS 1970.
Lewis, H. R.	Numerical Investigation of the Two Stream Instability Via Hamilton's Principle	American Physical Society, Miami, November 1968. Bull. Am. Phys. Soc., Ser. 2, 13 (1968) (Not previously reported.)

Symposium on Engineering Problems of Fusion Research, April 8-11, 1969, Los Alamos, NM. Proceedings published January 1970 as LA-4250.

Kewish, R. W., Jr. Dike, Robert S. Hammel, Hay E. Sherwood, A. R.	Mechanical Design of a Quadrupole Injection Experiment.
Gribble, R. F. Brown, D. Lillberg, J. W. Sawyer, G. A. Weldon, D. M.	Data Acquisition System for the Scyllac Device .
Boicourt, G. P.	Capacitor Development for Scyllac.
Boicourt, G. P. Kemp, E. L., Jr.	Development of Reliable, High-Voltage, Low-Inductance Cable for Scyllac.
Hanks, K. W. Boicourt, G. P.	Design and Development of Cable Cartridges for Scyllac.
Hammer, C. F. Gribble, R. F.	Scyllac Spark Gap and Trigger System Development.
Gribble, R. F.	Ferrite Loaded Piggy-Back Crowbar Gap.
Call, Darrell L.	Solid Dielectric Crowbar Switch.
Damerow, R. A. Crawford, J. C. Thomson, D. B. Caird, R. S., Jr. Ewing, K. J. Garn, W. B. Fowler, C. M.	Use of Explosive Generators to Power the Theta-Pinch.
Fowler, C. M. Thomson, D. B. Ewing, K. J. Caird, R. S., Jr. Garn, W. B.	High Altitude Pulsed Plasma Power Supply.
Wittman, F. E. Henderson, D. B. Dreicer, H.	Q Machine Hot Plate Development.

Haarman, R. A.	Liquid Resistor Development.
McLeod, J. J. Rand, J. L.	Precise Regulation of a 500 Kilowatt Direct Current Generator with a 2500 Ampere Series-Pass Transistor Bank.
Ware, K. D. Carpenter, J. P. Bottoms, P. J. Williams, A. H. Mather, J. W.	High Power Technology Associated with Dense Plasma Focus Research.
Carpenter, J. P. Ware, K. D. Bottoms, P. J. Williams, A. H. Mather, J. W.	Impedance Matching the Plasma Focus Device.
Boicourt, G. P.	Application of the Net-One Network Analysis Program to Distributed Circuits.
Dike, R. S. Borkenhagen, W. H.	High Current Joint Techniques.
Kemp, E. L., Jr.	Final Design of Scyllac.

International Conference on Physics of Quiescent Plasmas, Paris, Sept. 8-13, 1969. Proceedings, Laboratoire de Physique des Milieux Ionises, Ecole Polytechnique, 1970.

Dreicer, H. Henderson, D. B. Mosher, D. Wittman, F. E. Wolfsberg, K.	Measurement of the Resonant Charge Exchange Cross Section in a Potassium Q-Machine Plasma Column.
Henderson, D. B.	Angular Distribution of Efflux from an Atomic Beam Nozzle.

British Nuclear Energy Society Conference on Nuclear Fusion Reactors, Culham, 1969. Proceedings, Culham Laboratories, UKAE, 1970.

Bell, G. I. Borkenhagen, W. H. Ribe, F. L.	Feasibility Studies of Pulsed, High-Beta Fusion Reactors.

Oliphant, T.A.,Jr.	Fuel Burnup and Direct Conversion of Energy in a D-T Plasma.
Tuck, J.L.	On Nuclear Fusion Objectives.

American Physical Society Meetings, Los Angeles, Calif., November, 1969. Bull. Am. Phys. Soc., Ser 2, 14 (1969)

Baker, D.A. Mann, L.W.	High Beta MHD Equilibrium and Stability of Multipoles.
Bottoms, P. J. Mather, J.W. Carpenter,J.P Ware, K.D. Williams,A.H.	X Ray Measurements on Plasma Focus.
DiMarco, J.N. Burkhardt,L.C.	Fast Z-Pinch.
Dreicer, H. Henderson,D.B. Mosher, D. Wittman, F.E. Wolfsberg,K.	Measurement of the Resonant Charge Exchange Cross Section in a Potassium Q-Machine Plasma Column.
Fowler,C.M. Thomson,D.B. Caird,R.S.,Jr. Ewing,K.J. Garn, W.B.	Explosive Generator Power Supply for Driving a Plasma Gun.
Freidberg,J.P. Morse,R.L. Nielson,C.W.	Numerical Method for Studying Linear Stability of Highly Inhomogeneous Plasmas.
Freidberg,J.P.	Magnetohydrodynamic Stability of a Diffuse Screw Pinch.
Henderson,D.B.	Angular Distribution of Efflux from an Atomic Beam Nozzle.

Henins, I. Jeffries, R. A. Kerr, D. M., Jr. Marshall, J., Jr. Ingraham, J. C.	Explosive Generator Driven Coaxial Plasma Gun.
Karr, H. J. Forman, P. R. Phillips, J. A.	Dynamic Stabilization of the Z-Pinch by Linear Multiple Fields. I.
Marder, B. M. Weitzner, H.	Bifurcation Problem in E-Layer Equilibria.
McLeod, J. J. Michael, D. E. Dreicer, H.	Measurements of ECH Q-Machine Plasma. Properties.
Phillips, J. A. Forman, P. R. Haberstich, A. Karr, H. J. Schofield, A. E.	Dynamic Stabilization of the Z-Pinch by Linear Multiple Fields. II.
Quinn, W. E. Gribble, R. F. Little, E. M.	Experiments on a Three-Meter Collisionless Plasma Column.
Shonk. C. R. Morse, R. L.	Two-Dimensional, Two-Species PIC Simulations of Collisionless Shocks.
Thomas, K. S.	Measurement of Shorting Currents from a Theta Pinch Plasma.
Ware, K. D. Mather, J. W. Bottoms, P. J. Carpenter, J. P. Williams, A. H.	Voltage Scaling for Megajoule Plasma Focus Systems.
Williams, A. H. Carpenter, J. P. Bottoms, P. J. Ware, K. D. Mather, J. W.	Calorimetric Measurement of X Ray Flux from Plasma Focus.

American Physical Society meeting, Washington, April 1970. Bull. Am. Phys. Soc., Ser. 2, 15 (1970).

Bottoms, P.J.
Mather, J.W.
Carpenter, J.P.
Ware, K.D.
Williams, A.H.
Line Radiation Contributions in Plasma Focus.

Ribe, F.L.
Rosenbluth, M.N.
Feedback Stabilization of a High Beta Sharp Boundary Stellarator.

Ware, K.D.
Mather, J.W.
Bottoms, P.J.
Carpenter, J.P.
Williams, A.H.
High Voltage Plasma Focus Development.

Symposium on Feedback and Dynamic Control of Plasmas, June 1970. Princeton, New Jersey. Proceedings, No. 1, American Institute of Physics, New York, 1970.

Ribe, F.L.
Rosenbluth, M.N.
Feedback Stabilization of a High-Beta Stellarator.

CM/rb: 455 (130)